University of Milano-Bicocca
Department of Material Science

Hybrid and Nanocomposite Concepts:
A Driving Force for Novel Materials

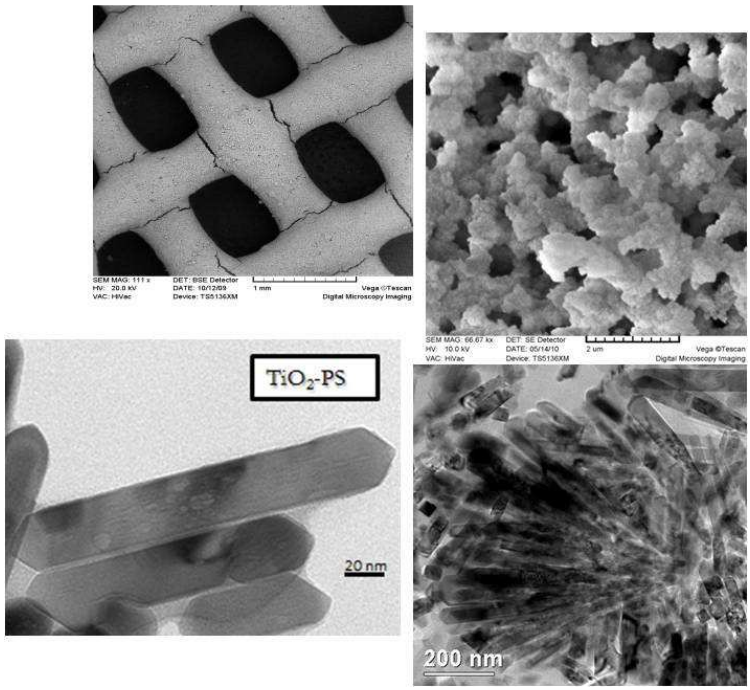

Maurizio Crippa
(reg. n. 483755)

Supervisor: Prof. Roberto Scotti

Dean of the Doctorate: Prof. Gian Paolo Brivio

PhD School in Materials Science – XXV cycle

PhD. Dissertation
January 2013

to Lou Lou

CONTENTS

CHAPTER 1

General Introduction:

Hybrids and Nanocomposites

1.1 Definition[1]

Since the beginning of the technological era the development of new products was accompanied by the necessity of novel materials. Many of the well-established them, such as metals, ceramics or plastics couldn't satisfy the challenges of the new applications. So that, specially at the end of the 20th, scientists and engineers started to mix different materials which showed superior properties then their separated counterparts. One of the most successful examples is the group of the composites where a material, the filler, is embedded into another one, the matrix. Usually the filler is an inorganic compound and a defined shape like particles, fibers, lamellae or mesh while the matrix is typically organic.

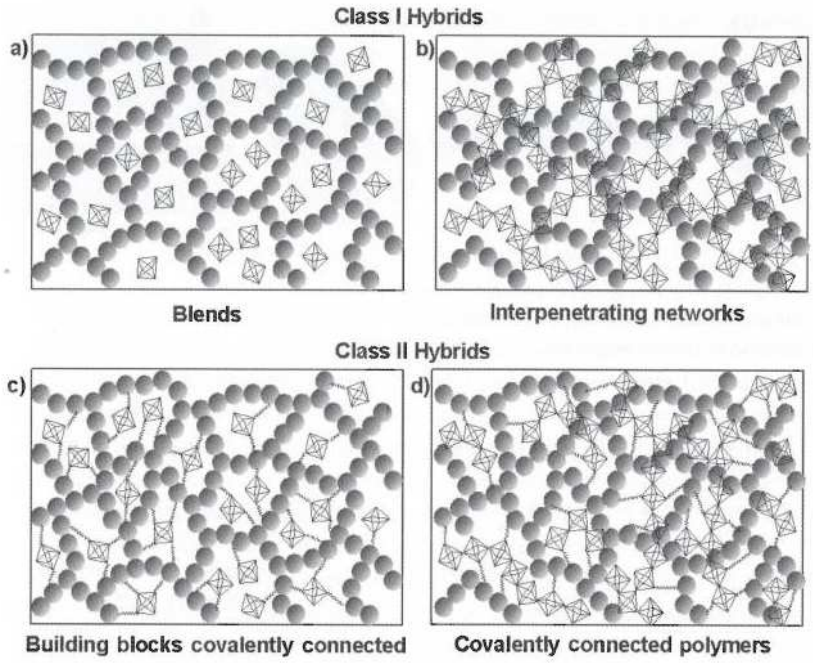

Fig. 1.1 Different types of hybrids materials. Isolated (a) and connected (b) inorganic species are weakly bonded to the organic counterpart in *class I* material while in (c, d) *class II* materials are strongly bonded (covalent and coordinative bonds)

Hybrid materials.[1] When the size of the inorganic units is decreased to the same level of the matrix building blocks a more homogeneous composite material is obtained. If the down-scaling is at the molecular level the intimate interaction between the counterparts could leads to a more homogeneous materials allowing to a fine tuning of the material properties. The obtained materials are called hybrid materials. Following the wide ranging definition reported by Kickelbick "a hybrid material is a material that includes two moieties blended on the molecular scale" (see Fig. 1.1) commonly but not necessary one of these compounds is organic and the other one inorganic. A more detailed definition is based on the interaction strength (see Fig.1.2) i.e. on the nature of the chemical bonds between the counterparts of the material. *Class I* materials are those that show weak interactions between the two phases, such as van der Waals, hydrogen bonding and weak electrostatic interactions. *Class II materials* are those that show strong interactions between the phases such as covalent, coordinative or ionic bonding.

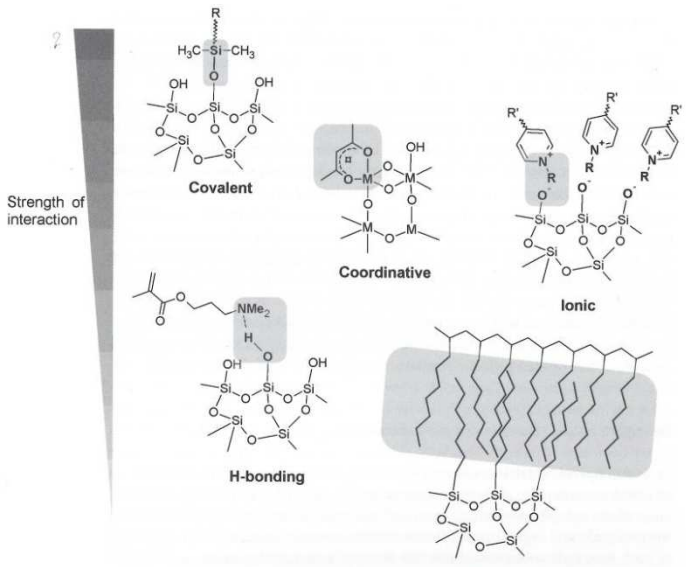

Fig.1.2 Some interactions typically exploited to build hybrid materials and their relative strength

Nanocomposites.[1] After the definition of hybrid materials the question is: what is the difference between inorganic-organic materials and inorganic-organic nanocomposite? Continuously thanking the contribution of Kickelbick resuming the accepted definitions of the scientific community "the term nanocomposite is used if one of the structural units, either the organic or the inorganic, is in a defined size range of 1-100 nm" (see Fig. 1.3). Depending on the size of one of the counterpart of the material there is a gradual transition between hybrid materials and nanocomposites if we think, for example, to large building blocks such as inorganic clusters or large conjugated molecules embedded in an inorganic matrix can already be of the nanometer scale. Then the term nanocomposites is usually used when discrete structural units, in the nanometer size range, are embedded in a matrix while the term hybrid materials is used when inorganic species are formed *in situ* by molecular precursor for example applying sol-gel reactions. The distinction between the two classes is still very thin if we consider for example the silica-rubber composite used for tires: which is the difference if the silica particles, in the nanometric size regime, are prepared and then blended with the rubber or *in situ* synthesized by sol gel reaction? In both cases the composite materials obtained contains silica nanoparticles embedded in a rubber matrix. So that the discrimination is usually done considering the preparation of the material: usually a nanocomposite is formed incorporating these preformed building blocks, such as particles, clay minerals, nanotubes etc. in organic polymers while as an hybrid material is a material where the inorganic counterpart is *in situ* synthesized.

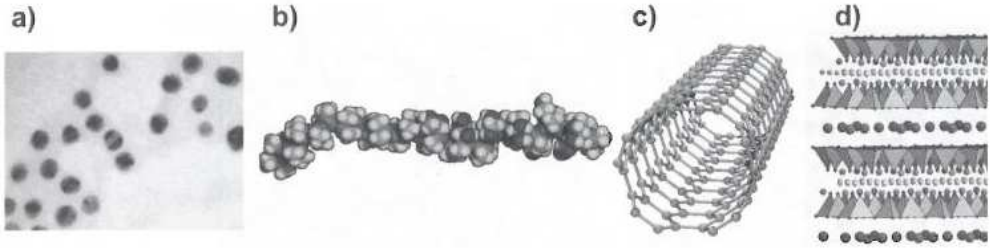

Fig. 1.3 Some different inorganic building blocks used in nanocomposites materials: a)nanoparticles, b) macromolecules, c)nanotubes, d)layered materials

1.2 Advantages of Inorganic/Organic Species Combination in One Material[1]

The glaring advantage of the inorganics and organics combination in one material is to obtain a material exhibiting an advantageous matching between the dissimilar properties of the two species. For example polymers show low density values while inorganic compounds are usually much higher: the obtained hybrid material density might be fine tuned properly balancing the two species constituting the material.

Another driving force for hybrid materials and nanocomposites is the possibility to create multifunctional materials combining some typical property of polymers with some peculiar characteristic of the inorganic materials such as for example the flexibility of the organic species and the electric characteristics of the inorganic counterpart.

Under the point of view of the processability hybrid materials have more polymer-like handle properties then solid state inorganic materials which typically require high temperatures process and lower shaping ability: a polymeric system can be extruded, filmed or shaped in a mold at relatively low temperature.

As reported in chapter 2 all of these peculiarities of hybrids and nanocomposites will be exploited to create novel materials.

1.3 The role of the Interface and the Interaction Mechanisms[1]

Reducing the size of a macroscopic object to the nanometric scale new physical properties of the material itself show up, i.e. the quantum size effect, and the ratio between the surface and bulk atoms increases. If we consider a packed atoms cube (see Fig. 1.4) with a side constituted by 16 atoms the resulting bulk atoms are 4096=16x16x16 while the surface ones are approximately 1352 (~33% of superficial atoms). Dividing the object in

eight cubes and repeating the process a second time the resulting atoms located on the surface are 2368 (~58% of superficial atoms) after the first division and 3584 (~88% of superficial atoms) the second time being the atoms number always constant. This example evidences the importance of the surface when the size of an object is down-scaled. Considering the surface importance of the scaling-down the inner interface between the different phases become predominant for the feature of hybrids and nanocomposites influencing the properties of the building blocks and finally of the material's properties. As explained in the section 1.1 the nature of the interaction strength between the phases interface is used to classify the materials. For example if the two moieties have different polarity the system could thermodynamically phase separate. Depending on the level, i.e. micrometric or nanometric scale, the systems can separate leading to macro or microphase separations. Usually such a system would thermodynamically equilibrate overtime but if a network is forming during the time, for example because a sol-gel reaction occurs, the system will be kinetically stabilized. As explained in chapter 4 this properties will be originally exploited to produce a porous materials.

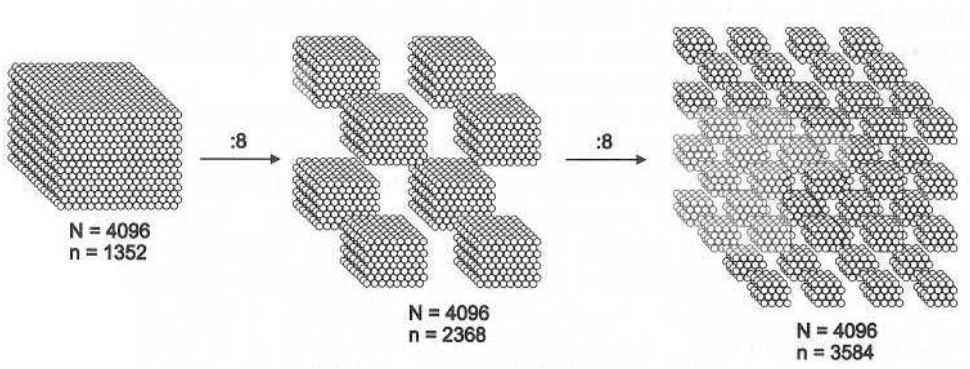

Fig. 1.4 Graphical representation of the sizing effect obtained dividing twice a cube with 16x16x16 atoms. N=total atoms, n=surface atoms

The high surface area of the building blocks, such as particles, can lead to a significant interaction between the embedded material and the matrix having a large influence on the physical properties. These properties, for example electron transfer, will be deeply described in the chapter 3.

As nanosized objects, inorganic nanoparticles show high surface energy, that if it is not reduced by some surface agent, i.e. surfactants or generally surface functionalizing molecules, such particles tend to agglomerate in an organic medium. In some case the agglomeration is detrimental for the final physical properties of the material but sometime a controlled agglomeration is desired to emphasize some other ones. In chapter 4 and 5 both of them characteristics will be explored to optimize two different applications for titanium dioxide.

1.4 Synthetic Strategies[1]

Two different approaches can be used to prepare hybrid and nanocomposite materials. Defined and preformed building blocks can react each other to form the final material leading to the formation of a system in which the precursor is partially kept integer: the building blocks approach. On the other hand the second approach is based on the *in situ* transformation of the precursors into a novel network generating the components of the new structure. Because on the present work both of the methodologies were used the two methods are described in detail highlighting them advantages and disadvantages.

Because the present introduction wants to be a general overview on hybrids and nanocomposites materials the detailed introductions to the synthetic methods such as sol-gel synthesis in chapter 4 and RAFT polymerization in chapter 5, used to prepare the different explored materials, are introduced in every chapter. Just the synthesis of the

titanium dioxide is described in the section 1.5.3 of the introduction because it is the common denominator of the entire work.

1.4.1 The Building Block Approach[1]

As mentioned above this approach is based on the preservation of a structural unit which, reacting during the material formation, is at least found partially integer after the material synthesis. Being the building block preserved after the formation of the material its physical properties are also transferred into the novel material. Representative examples of building blocks (see Fig. 1.3) are modified inorganic clusters or surface functionalized nanoparticles with reactive organic groups. Depending on the number of the functional groups present on the surface, generally for nanoclusters, with one reactive functional group on the surface the unit structure can just functionalize the polymeric chain while with two of them can be part of a chain and with more than three can generate a 3D network i.e. the unit structures can be used without additional molecules for the formation of a crosslinked material. In case of nanosized building blocks like nanoparticles the obtained material is a nanocomposites. Being the structural units at least partially preserved after the formation of the final material the original properties of the building blocks can be easily transferred to the material and then better final properties of the material can be precisely tuned. Furthermore the building blocks can be designed to optimize the synthesis formation of the final material. The dispersability of inorganic nanoparticles in an organic medium, for example, can be increased and controlled to produce a more uniform material as exploited in different ways in the chapters 4 and 5.

1.4.2 In Situ Formation of the Components[1]

The *in situ* formation of hybrid materials is based on the chemical synthesis of the material starting from the chemical precursors during the material's preparation. Usually this is the typical case of the polymer synthesis but also if the sol gel is used to produce the inorganic moiety of the composite. In this approach the molecules are converted in multidimensional structures which exhibit different properties than their precursor. Of course the final properties like the internal structure of the final material depend both on the composition of the precursor and on the synthesis conditions. For example the sol gel synthesis of silica is influenced by the catalytic conditions used during the preparation: base conditions produce globular-like structures while acid conditions leads to polymer-like structures. In the chapter 4 different catalytic conditions will be studied to produce two materials with the same composition but different microstructural properties.

1.5 A Common Denominator: the TiO_2

Morphology of TiO_2. Titanium is the world's fourth most abundant metal (exceeded only by aluminium, iron, and magnesium) and the ninth most abundant element (constituting about 0.63% of the Earth's crust). It was discovered in 1791 in England by Reverend William Gregor, who detected the presence of a new element in ilmenite. Then the element was rediscovered several years later by the German chemist Heinrich Klaporth who named it Titans, mythological first son of the goddess Ge (Earth in Greek mythology).

Titanium dioxide can exist mainly in one of three bulk crystalline forms: rutile, anatase, and brookite. The structures of these polymorphs can be discussed in terms of $(TiO_6)^{2-}$ octahedrals, where each Ti^{4+} ion is surrounded by an octahedron of six O^{2-} ions. The three

crystal structures differ from the distortion of each octahedral and by the assembly patterns of the octahedral chains. Anatase can be regarded as being composed of octahedrals that are connected by their vertices; in rutile, the edges are linked, and in brookite, both vertices and edges are connected (see Fig. 1.5). In rutile, a slight distortion from orthorhombic structure occurs, where the unit cell is stretched beyond a cubic shape. In anatase, the distortion of the cubic lattice is more significant; and thus the resulting symmetry is less orthorhombic. The Ti-Ti distances in anatase are larger, whereas the Ti-O distances are shorter than those in rutile[2].

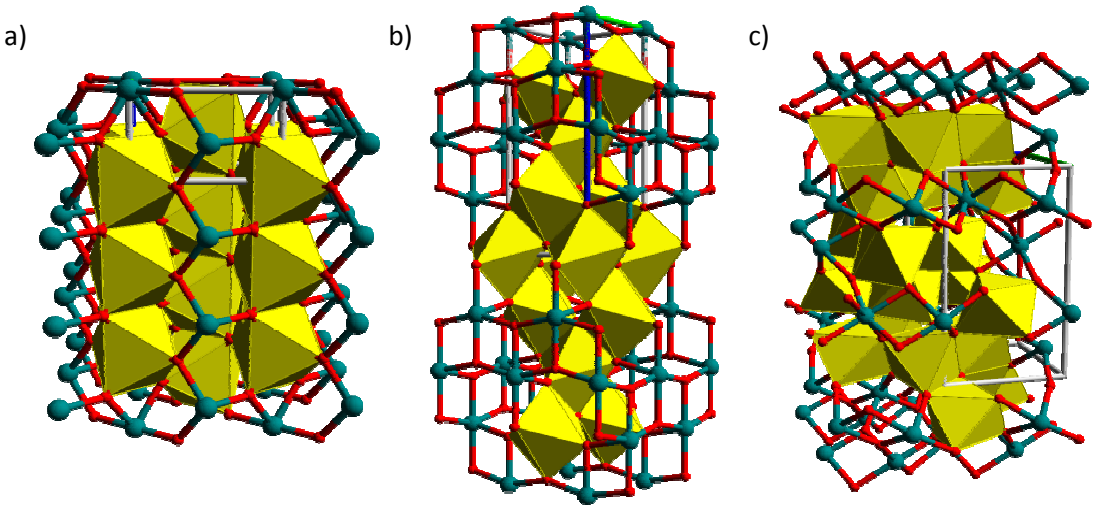

Fig. 1.5. Bulk crystal structures of rutile (a), anatase (b), and brookite (c).

These differences in lattice structures cause different mass densities and electronic band structures between the two main forms of TiO_2. Thermodynamic calculations based on calorimetric data predict that rutile is the most stable phase[3,4] at all temperatures and pressures up to 60 kbar. The small differences in the Gibbs free energy (4–20 kJ/mol) between the three phases suggest that the metastable polymorphs are almost as stable as rutile at normal pressures and temperatures. Particle size experiments performed by Zhang and Banfield, affirm that the relative phase stability may reverse when particle sizes decrease to sufficiently low values due to surface-energy effects [5] (surface free energy and

surface stress, which depend on particle size); if the particle sizes of the three crystalline phases are equal, anatase becomes the most thermodynamically stable at sizes less than 11 nm. Brookite is most stable between 11 and 35 nm, and rutile is most stable at sizes greater than 35 nm [6]. The enthalpy of the anatase → rutile phase transformation is low. A survey of the literature reveals widespread disagreement, with values ranging from -1.3 to 6 ± 0.8 kJ/mol [7]. Kinetically, anatase transformation into rutile at room temperature practically does not occur. At the macroscopic scale, the transition reaches a measurable speed for bulk TiO_2 at T > 600°C [8]. The anatase → rutile conversion has been studied for many reasons[9], because the TiO_2 crystalline phase (i.e., anatase or rutile) is one of the most critical parameters determining its use as a photocatalyst [10]. This transition, achieved by increased temperature or pressure, is influenced by several factors such as the concentration of lattice and surface defects, which mainly depend on the synthetic method [11] and the presence of dopants [12], because these defects act as nucleation sites. On the other hand, since the transformation involves an overall contraction or shrinking of the oxygen structure (as indicated by a volume shrinkage of approximately 8%) and a co-operative movement of the ions, the removal of oxygen ions (i.e., the formation of oxygen vacancies) accelerates the transformation.

Under the light of hybrid and nanocomposites materials and using titania nanoparticles as building blocks the attention on the phase transition is more focused on the sintering growth due to the particle size. Banfield et al. found that the conversion temperature and the rate of transformation depend on how fast the primary particles in the anatase phase sinter together to reach the critical size [13]. Once the critical particle size is achieved using nanosized anatase as the starting material, the transformation reaches a measurable speed at lower temperatures (T > 400°C); and when rutile is formed, it grew much faster than anatase [4,14]. This phenomena are take into account on the chapter 4 during the calcinations step of the hybrid material.

TiO_2 as semiconductor. Due to oxygen vacancies, TiO_2 is an n-type semiconductor. These vacancies are formed according to the following reaction:

$$O_o^x \xrightarrow{TiO_2} V_o^{hh} + 2e^- + \tfrac{1}{2} O_{2\,(gas)} \qquad (1)$$

where the Kröger–Vink defect notation is used to explain that inside TiO_2 a positive (2+) charged oxide ion vacancy (V_o^{hh}) is formed upon release of two electrons and molecular oxygen. For example, this reaction can be induced by thermal treatment in an oxygen-poor environment (reducing conditions). A photocatalyst is characterized by its capability to adsorb simultaneously two reactants, which can be reduced and oxidized by a photonic activation through an efficient absorption i.e. when the incident photon energy is higher than the electronic gap ($h\nu \geq E_g$). The Fig. 1.6 shows the band gap of several semiconductors and some standard potentials of redox couples. The ability of a semiconductor to undergo photoinduced electron transfer to an adsorbed particle is governed by the band energy positions of the semiconductor and the redox potential of the adsorbates. The energy level at the bottom of conduction band is actually the reduction potential of photoelectrons. The energy level at the top of the valence band determines the oxidizing ability of photoholes, each value reflecting the ability of the system to promote reductions and oxidations. The flatband potential, V_{fb}, locates the energy of both charge carriers at the semiconductor–electrolyte interface, depending on the nature of the material and system equilibrium [15].

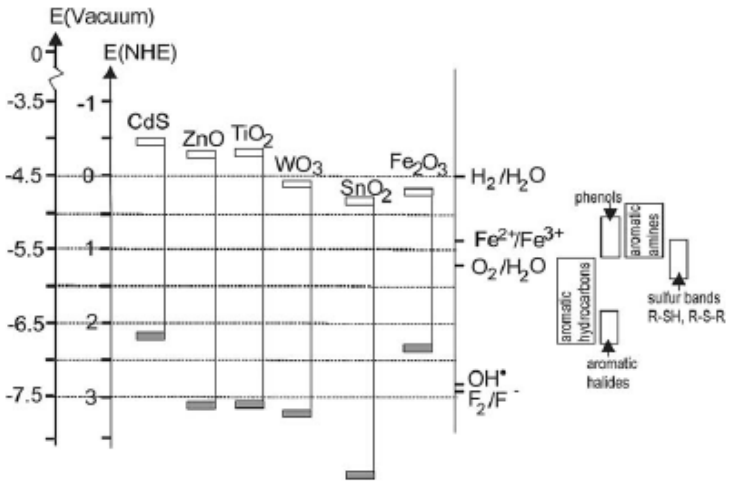

Fig. 1.6. Band positions (top of valence band and bottom of conduction band) of several semiconductors together with some selected redox potentials.

From the thermodynamic point of view, adsorbed couples can be reduced photocatalytically by conduction band electrons if they have more positive redox potentials than V_{fb} of the conduction band, and can be oxidized by valence band holes if they have more negative redox potentials than the V_{fb} of the valence band [16]. Unlike metals, semiconductors lack a continuum of interband states to assist the recombination of electron–hole pairs, which assure a sufficiently long lifetime of e^-–h^+ pair to diffuse to the catalyst's surface and initiate a redox reaction [17]. The different anatase and rutile TiO_2 lattice structures causes different densities and electronic band structures, leading to different band gaps (for bulk materials: anatase 3.20 eV and rutile 3.02 eV) [18].

Thus, when photons have a higher energy than this band gap an electron is promoted to the CB, leaving a hole in the VB. The subsequent mode of action of the photogenerated electron–hole pair (e^--h^+), determines which of the phenomena is the dominant process because even if they are intrinsically different processes, they can actually take place concomitantly on the same TiO_2 surface.

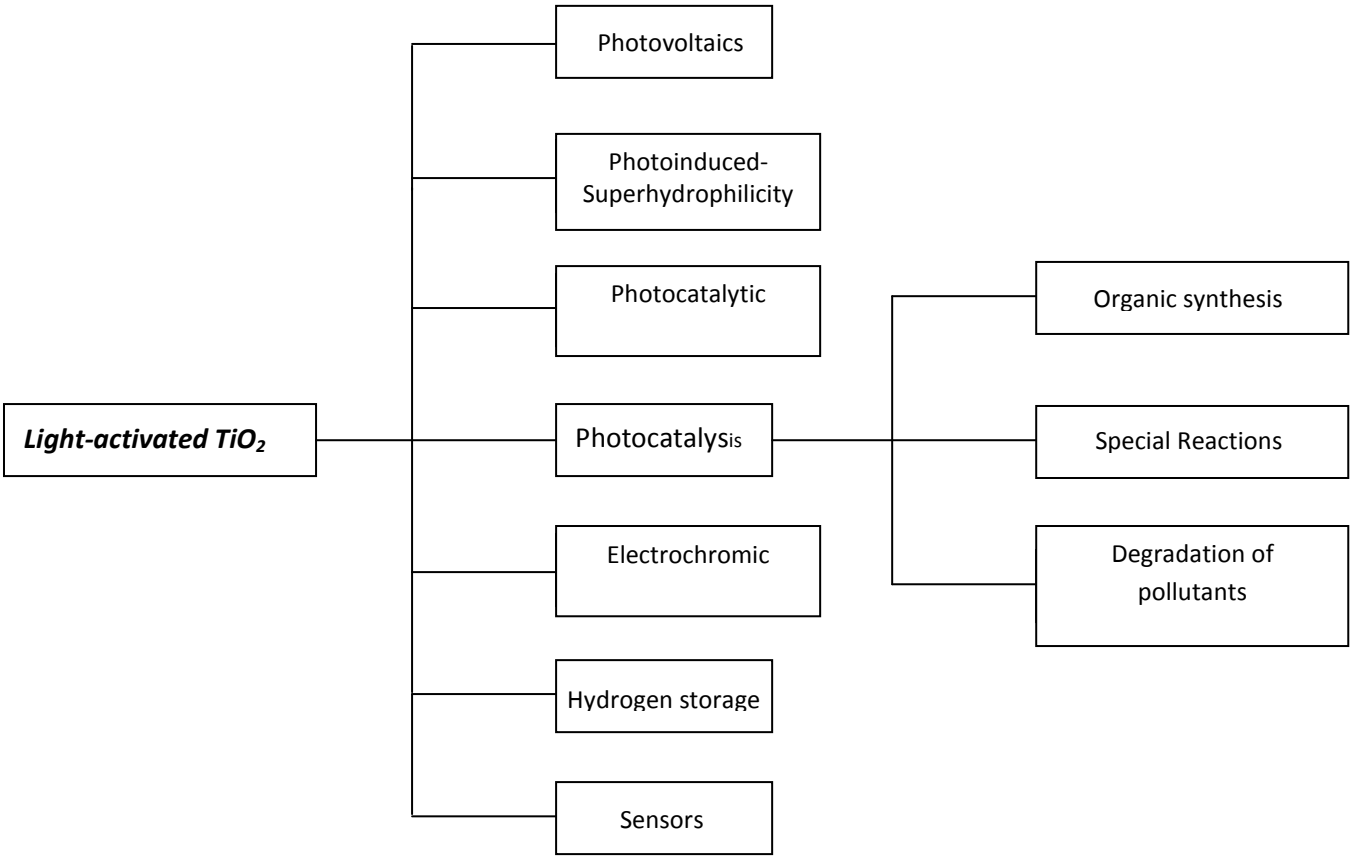

Fig. 1.7. Photoinduced processes on TiO_2

In fact, the excited electron can either be used directly to create electricity in photovoltaic solar cells or drive a chemical reaction, which is properly called photocatalysis. Another phenomenon was recently discovered: the trapping of holes at the TiO_2 surface causes a high wettability and is termed 'photoinduced superhydrophilicity (PSH). All the photoinduced phenomena involving light activated TiO_2 are summarized in Fig. 1.7. For the purposes of the present work the attention on the photoinduced phenomena will be focused on the photocatalysis effects and on the dielectric characteristic of the different TiO_2 crystal structures.

1.5.1 TiO_2 as Photocatalyst

Titanium dioxide is among the most extensively studied photocatalyst and it has been widely used for photodegradation of various pollutants [19]. TiO_2 can also be used to kill bacteria, as has been carried out with *E. coli* suspensions [20]. The photocatalytic reaction mechanisms are widely studied. The principle of the semiconductor photocatalytic process is straightforward [21]. Upon absorption of photons with energy larger than the band gap of TiO_2, electrons are excited from the valence band to the conduction band, creating electron-hole pairs (Fig. 1.8) [22]. These charge carriers can migrate to the surface of the oxide activating reduction and oxidation reactions with adsorbed the species:

$$(Ox_1)_{ads} + (Red_2)_{ads} \xrightarrow[h\nu > E_g]{TiO_2} (Red_1) + (Ox_2) \qquad (2)$$

Under the point of view of the efficiency the different interfacial electron processes, involving e^- and h^+, compete with the major deactivation processes i.e. the e^-h^+ recombination which may occur both in the bulk or at the surface (Fig. 1.8).

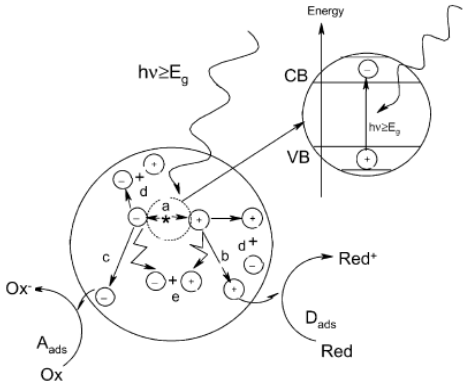

Fig. 1.8. Main processes occurring on a TiO_2 particle: (a) electron–hole generation; (b) oxidation of donor (D); (c) reduction of acceptor (A); (d) and (e) electron–hole recombination at surface and in bulk, respectively.

The photomineralization processes usually involve one or more radicals or intermediate species such as $OH^{\bullet}$, O_2^-, H_2O_2, or O_2, which play some relevant roles in the photocatalytic reaction mechanisms. In fact [23]:

– they may react chemically with themselves or surface-adsorbed compounds;

- they may recombine by back electron-transfer reactions, especially when they are trapped near the surface, due to either the slowed-down outward diffusion or hydrophobicity;

– they may diffuse from the semiconductor surface and participate in chemical reactions in the bulk solution.

In particular the highly oxidant $OH^{\bullet}$ radicals [24] are considered to be the main responsible for the photodegradation of organic and inorganic molecules adsorbed on the surface of TiO_2. They can be generated either in the presence of the homogeneous oxidant (H_2O_2) or heterogeneous (O_2) by reaction of holes in the valence band with adsorbed H_2O, hydroxide, or surface titanol groups (- TiOH):

$$OH^- + h^+ \rightarrow OH^{\bullet} \quad (3)$$

The photogenerated electrons are reducing agents which are strong enough to produce the superoxide (O_2^-):

$$O_{2,\,gas} + e^- \rightarrow O_2^- \quad (4)$$

This superoxide is an effective oxygenation agent that attacks neutral substrates as well as surface-adsorbed radicals and/or radical ions.

In theory, the redox potential of the electron–hole pair permits H_2O_2 formation, either by water oxidation by holes or by two conduction band electron reduction of the adsorbed oxygen. The latter represents the main pathway of H_2O_2 formation [25]:

$$O_{2,\,gas} + 2\,H_2O_{ads} + 2\,e^- \rightarrow 2\,H_2O_2 + 2\,OH^- \quad (5)$$

Moreover O_2^- centers may further generate H_2O_2 by the following steps [100, 104]:

$$O_2^- + H_2O \rightarrow HO_2^\bullet + OH^- \quad (6)$$

$$2\,HO_2^\bullet \rightarrow H_2O_2 + O_2 \quad (7)$$

$$HO_2^\bullet + H_2O + e^- \rightarrow H_2O_2 + OH^- \quad (8)$$

H_2O_2 contributes to the degradation pathway by acting as an electron acceptor or as a direct source of hydroxyl radicals due to homolytic scission.

$$H_2O_2 + e^- \rightarrow OH^\bullet + OH^- \quad (9)$$

Finally, hydroxyl radicals $OH^\bullet$ can react, for instance, with the organic substrates (S), till complete mineralization due to their high oxidizing potential (2.80 eV) [24]:

$$OH^\bullet + S \rightarrow CO_2 + H_2O \quad (10)$$

A schematic representation of this process is displayed in Fig. 1.9.

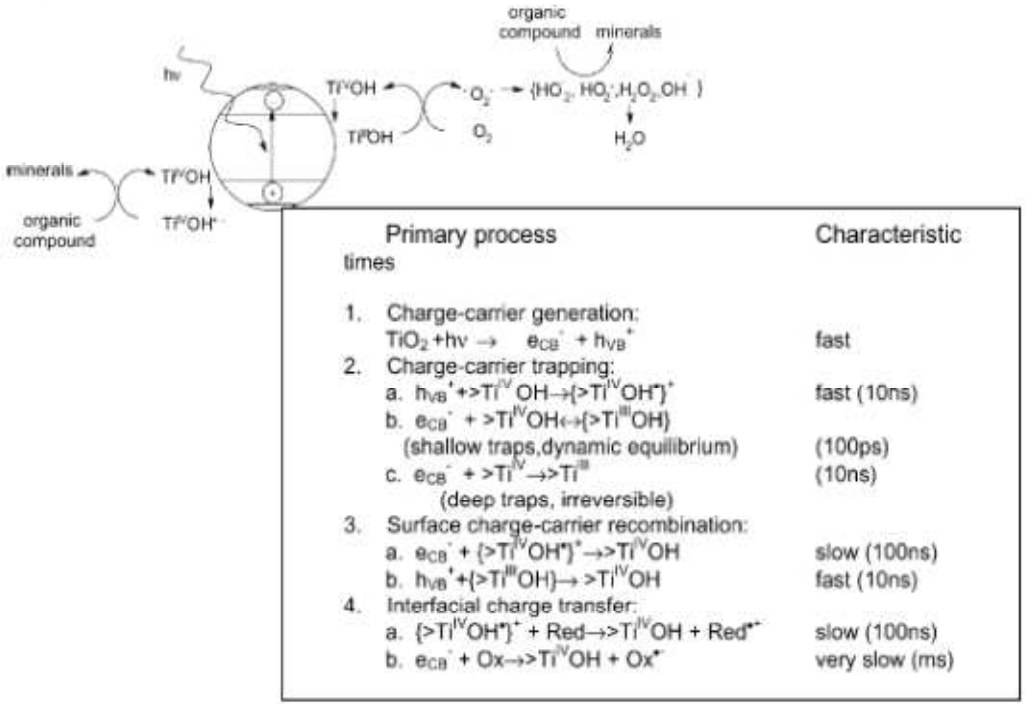

Primary process	Characteristic times
1. Charge-carrier generation:	
$TiO_2 + h\nu \rightarrow e_{CB}^- + h_{VB}^+$	fast
2. Charge-carrier trapping:	
a. $h_{VB}^+ + >Ti^{IV}OH \rightarrow \{>Ti^{IV}OH^{\bullet}\}^+$	fast (10ns)
b. $e_{CB}^- + >Ti^{IV}OH \leftrightarrow \{>Ti^{III}OH\}$ (shallow traps,dynamic equilibrium)	(100ps)
c. $e_{CB}^- + >Ti^{IV} \rightarrow >Ti^{III}$ (deep traps, irreversible)	(10ns)
3. Surface charge-carrier recombination:	
a. $e_{CB}^- + \{>Ti^{IV}OH^{\bullet}\}^+ \rightarrow >Ti^{IV}OH$	slow (100ns)
b. $h_{VB}^+ + \{>Ti^{III}OH\} \rightarrow >Ti^{IV}OH$	fast (10ns)
4. Interfacial charge transfer:	
a. $\{>Ti^{IV}OH^{\bullet}\}^+ + Red \rightarrow >Ti^{IV}OH + Red^{\bullet+}$	slow (100ns)
b. $e_{CB}^- + Ox \rightarrow >Ti^{IV}OH + Ox^{\bullet-}$	very slow (ms)

Fig. 1.9. Main processes occurring on a TiO_2 particle: (a) electron–hole generation; (b) oxidation of donor (D); (c) reduction of acceptor (A); (d) and (e) electron–hole recombination at surface and in bulk, respectively.

The photocatalytic activity of a semiconductor is largely controlled by (i) the light absorption properties, e.g., light absorption spectrum and coefficient, (ii) reduction and oxidation rates on the surface by the electron and hole, (iii) and the electron-hole recombination rate. Specially the first point has to be take care during the preparation of hybrids and nanocomposites because is related to the matrix while the other two are related to the nature of the particles.

A large surface area with a constant surface density of adsorbents leads to faster surface photocatalytic reaction rates. On the other hand, the surface is a defective site; therefore, larger the surface area, faster the charges recombination is. The higher the crystallinity, the fewer the bulk defects, and the higher the photocatalytic activity is. High temperature treatment usually improves the crystallinity of TiO_2 nanomaterials, which in turn can induce

the aggregation of small nanoparticles and the decrease of the surface area [2]. Both crystal structures, anatase and rutile, are commonly used as photocatalyst, with anatase showing a greater photocatalytic activity for most reactions [26]. It has been suggested that this increased photoreactivity is due to anatase's slightly higher Fermi level and the higher degree of hydroxylation (i.e., number of hydroxyl groups on the surface) [27].

The excitation of charge carriers (electron-hole pairs) for TiO_2 materials occurs when the substrate material absorbs photons of energy higher than its band gap (reaction 11).

These charge carriers can nonradiatively or radiatively recombine (dissipating the input energy as heat), or get trapped and react with electron donors or acceptors adsorbed on the surface of the photocatalyst (Fig. 1.8). In fact, electrons and holes generated after UV irradiation in TiO_2 nanoparticles are localized at different defect sites on the surface and in the bulk. Holes are trapped at bulk or surface O^{2-} ions giving paramagnetic O^- species [28] (reaction 12); while electrons are trapped on Ti^{4+} ions located at the bulk, at the surface and, in mixed-phase systems, at the anatase-rutile interface, giving EPR (electron paramagnetic resonance) active Ti^{3+} species (reaction 13) [29]:

$$TiO_2 + h\nu \rightarrow e^-_{CB} + h^+_{VB} \quad (11)$$

$$O^{2-} + h^+_{VB} \rightarrow O^- \quad (12)$$

$$Ti^{4+} + e^-_{CB} \rightarrow Ti^{3+} \quad (13)$$

According to reactions 11–13, the paramagnetic species Ti^{3+} and O^- may be considered as probes of the photogenerated electrons and holes, respectively, and can be revealed by EPR spectroscopy [30]. This technique is used to investigate the chemical activity of composite material in the chapter 3. Under continuous UV illumination, photogenerated electrons are either trapped at localized states within the band gap (Ti^{3+} centers) where they are accessible to EPR spectroscopy or promoted to the conduction band where they

can be detected by their IR absorption, which results from their electronic excitation within the conduction band in the infrared region.

Using this method, the lifetime of the photoexcited electrons and holes can be measured and is found to be on the order of hours at low temperature (T=90 K). At room temperature, the recombination process is much faster, and the photogenerated electrons and holes recombine rapidly. Fig. 1.10 illustrates the detection of photogenerated electrons and holes via either EPR or IR spectroscopy.

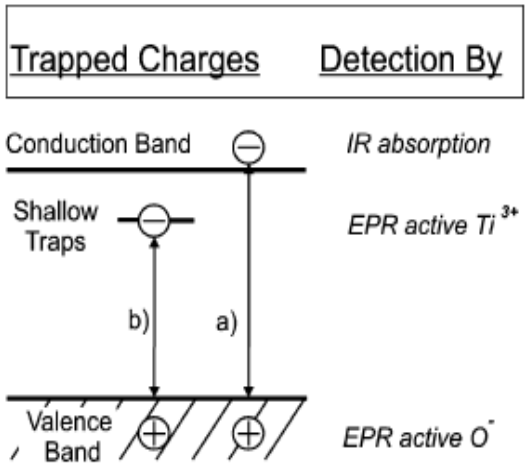

Fig. 1.10. Scheme of UV induced charge separation in TiO_2. Electrons from the VB can either be trapped (a) by defect states, which are located close to the CB (shallow traps), or (b) in the CB where they produce absorption in the IR region. EPR spectroscopy detects both electrons in shallow traps, Ti^{3+}, and hole centers, O^-.

According to the above-mentioned mechanism and time characteristics, two critical parameters determine the overall efficiency of photocatalytic processes:

– the competition between charge-carrier recombination and trapping (ps to ns);

– the competition between trapped carrier recombination and interfacial charge transfer (μs to ms).

The different recombination lifetimes and interfacial electron-transfer rate constants may be due to many factors, such as the different preparation methods of the samples that result in different crystal defect structures and surface morphologies. Because their reasons, as explained in the chapter 2, in order to prepare composite materials for photocatalysis the adopted strategy is to start from *ex situ* synthesized particles optimized for photocatalysis. In a second step the particles are immobilized into the matrix instead to *in situ* synthesized.

1.5.2 TiO_2 as Dielectric Material

The dielectric properties of the titanium oxide were measured on the beginning of the XX century. The dielectric properties such as the dielectric constant and the conduction properties are strictly related to crystal phase. It is well known that between the three crystalline forms of TiO_2, rutile, brookite and anatase the mean dielectric constants are 114, 78 and 31 respectively [31]. The peculiar high dielectric constant of the rutile was accurately measured by Schmidt in 1902 [32]. He found a dielectric value of 173 along the *c axis* and 89 along the *a/b axes*. [31] The mean dielectric constant can roughly calculated summing twice one third of the value along the *axis b*, because along the two directions perpendicular to the principal *axis c* rutile has the same values, to one third of the value along the *axis c*. Because the huge difference between the dielectric constant of the rutile and of the anatase phases many researches were accomplished to study the dielectric characteristic of rutile. Actually these researches were driven by the applicative perspectives of the material for the realization of electronic devices. On the other hand the electronic conduction characteristics of the anatase phase, as n-type semiconductor, were deeply investigated specially because the use of anatase nanoparticles as electrode on Graetzel solar cells. As reported by Tang resistivity and Hall-effect measurements

revealed as at high doping concentrations anatase, and not rutile, shows a metallic transition of the donor conduction band. This indicates that anatase has a large radius of donor electron wave function compared that of rutile. A larger Bohr radius of donor electrons suggests a smaller effective mass in anatase which is responsible for the higher electron mobility [33].

The chapter 5 of this work is focused on the exploiting of shape controlled rutile nanoparticles used as building blocks for a nanocomposite dielectric material.

1.5.3 Synthesis methods of TiO_2

Being the present work focused on the exploration of hybrid and nanocomposite materials using, as building block, crystalline phase and size shape controlled TiO_2 nanoparticles the exploration of the synthetic methods of TiO_2 is limited to the two main route generally accepted to produce controlled and reproducible titania nanoparticles: the sol-gel method and the hydrothermal method.

Sol-gel method. TiO_2 nanoparticles can be synthesized with the sol-gel method by two main different approaches: the alkoxide and the non-alkoxide route [34].

The former uses metal alkoxides as starting material [35], while the latter uses inorganic salts [36] such as nitrates, chlorides, acetates, carbonates, acetylacetonates, etc.

The alkoxide method involves the hydrolysis of titanium alkoxides (reaction 1) with the formation of a TiO_2 sol or gel or precipitation and the condensation with the development of Ti-O-Ti polymer chains (reaction 2, 3) [37] :

$$\equiv Ti\text{-}OR + H_2O \leftrightarrows \equiv Ti\text{-}OH \quad (1)$$

$$2\ \equiv Ti\text{-}OH \leftrightarrows \equiv Ti\text{-}O\text{-}Ti\equiv + H_2O \quad (2)$$

$$\equiv Ti\text{-}OH + \equiv Ti\text{-}OR \leftrightarrows \equiv Ti\text{-}O\text{-}Ti\equiv + ROH \quad (3)$$

These two processes are strictly related to the reaction conditions, such as the water/alkoxide ratio, acid/base catalyst, solvent type, gel aging, reaction temperature, and mixing technique. Furthermore, hydrolysis and condensation are competitive, and in order to exhibit better control over the evolution of the crystalline phase, porosity and size of TiO_2 nanoparticles, it is desirable to separate and temper these two steps [21]. With this aim, several approaches are adopted. One of them is alkoxide modification by complexation with coordination agents which are less easily hydrolysed, i.e. they are more strongly bonded to the metal, such as carboxylates [38], or β-diketonates [39]. Additionally, the preferred coordination mode of these ligands can be exploited to control the evolution of the structure. These reactions are followed by a thermal treatment (450–600°C) to remove the organic part and to crystallize either anatase or rutile TiO_2. The calcination process will inevitably cause a decline in surface area and mesoporosity (due to sintering and crystal growth), loss of surface hydroxyl groups, and even induce phase transformation.

Acid–base catalysis can also be used to enable separation of hydrolysis and condensation steps. Pratsinis et al studied the effect of HCl or NH_4OH catalysts added during hydrolysis of titanium tetraisopropoxide (TTIP) on the crystal phase and porosity of the resulting TiO_2 nanoparticles [40]. They demonstrated that HCl enhances the hydrolysis rate and ultimately the phase transformations of the titania powders from amorphous to anatase as well as anatase to rutile, while NH_4OH retarded both phase transformations. Finally, they observed that titania powders calcined at 500°C showed bimodal pore size distributions: one was intra-aggregated pores with average pore diameters of 3–6 nm and the other was inter-aggregated pores with average pore diameters of 35–50 nm. The average intra-

aggregated pore diameter was decreased with increasing HCl concentration, while it was increased with increasing NH_4OH concentration.

Li et al. reported that the water/alkoxide ratio also strongly influences the hydrolysis and condensation processes in the synthesis of TiO_2 [41]. They observed that an increase of the water concentration accelerates the cross-linking process and reduces the gelation time. In fact at the highest water concentration, macromolecular networks form rapidly through the reactions of hydrolysis and condensation, and have low interconnectivity. Consequently, the network is rather loose, and the solvent may easily migrate out of the network.

In contrast, a system with lower water amount will form slowly leading to a denser and more structured network that can incorporate a higher solvent concentration. The gel powders synthesized from different water concentrations are calcined at various temperatures up to 700°C to obtain TiO_2 powders.

In general, with the alkoxide route, pure anatase or mixed phase has been obtained. Pure rutile was produced by heating the powders at temperatures higher than 400 °C, which also causes undesired grain coarsening, aggregation, and reduction of the surface area [42] or alternatively, crystallization under hydrothermal conditions [43].

Several efforts were also directed in the synthesis of TiO_2 by the non-alkoxide route, nevertheless it has the disadvantage of the additional removal of the inorganic anion.

For instance, the thermohydrolysis of $TiCl_4$ [44] in an aqueous medium was proposed as an alternative soft-chemistry method to prepare pure anatase as it allows one to control the particle size at the nanometric scale as a function of pH, but also in this case pure rutile was produced by treating the powders at high temperature. Different compositions of rutile, anatase, and brookite were obtained by thermohydrolysis and oxidation of $TiCl_3$,[45] accurately varying the pH between 0 and 7. However, in this case brookite-free anatase could not be obtained. Also in this synthesis route, in order to tune the evolution of the

crystalline phase, porosity and size of TiO_2 nanocrystals, the high reactivity toward hydrolysis and condensation of transition metal oxide precursors have to be controlled.

The hydrothermal route. Performing a chemical reaction in a sealed vessel (bomb, autoclave, etc.), where solvents can be brought to temperatures well above their boiling points by the increase in autogenous pressures resulting from heating is referred to as solvothermal process, or in the case of water as solvent, to an hydrothermal process. Review articles focused specifically to these methods appear frequently in the literature [46].

The hydrothermal process is performed under subcritical water conditions, e.g. at temperatures below 374 °C and pressure lower than 218 atm. Above these values, water is said to be supercritical. Supercritical fluids exhibit characteristics of both a liquid and a gas: the interfaces of solids and supercritical fluids lack surface tension, yet supercritical fluids exhibit high viscosities and easily dissolve chemical compounds that would otherwise exhibit very low solubility under the ambient conditions.

Only a few hydrothermal processes involve supercritical solvents. Most, however, simply take advantage of the increased solubility and reactivity of metal salts and complexes at elevated temperatures and pressures without bringing the solvent to its critical point. Moreover, hydrothermal processing allows many inorganic materials to be prepared at temperatures substantially below those required by traditional solid-state reactions. Unlike the cases of co-precipitation and sol-gel methods, which also allow for substantially reduced reaction temperatures, the products of hydrothermal reactions are usually crystalline and do not require post-annealing treatments. During the synthesis of nanocrystals, parameters such as temperature, pH, reactant concentration and molar ratio, additive, etc., can be tuned to maintain a high simultaneous nucleation rate and good size distribution, obtaining crystalline products with different composition, structure and morphology. As a matter of safety, the pressures generated in a sealed vessel should

always be estimated beforehand. Finally, the equipment and processing required in the hydrothermal process are simpler, the control of reaction conditions is easier and scale-up problems, often related to lack of homogeneity in big reactors, can be resolved by the application of specific strategies [47]. For all these reasons, the hydrothermal route is widely used for the production of nanoparticles in the ceramics industry. For example, perovskite-type (tabular), pyrochlore-type (starlike) and tetragonal body-centered type (acicular) $PbTiO_3$, $PbTi3O_7$, and $PbO\text{-}TiO_2$ solid solution ($PbTi_xO_{l+2x}$, x = 0.8) (tabular) have been obtained under different hydrothermal conditions [48].

The synthesis of nanocrystalline TiO_2, is one of the most thoroughly investigated solvothermal/hydrothermal reactions. Oguri et al. reported in 1988 the hydrothermal synthesis of monodispersed anatase nanoparticles by the controlled hydrolysis of $Ti(OEt)_4$ in ethanol [49]. Successively, Cheng et al. developed a method to prepare nanoparticulate, phase-pure rutile and anatase from aqueous $TiCl_4$ by a hydrothermal process [48]. They found that acidic conditions favoured rutile, while basic conditions favoured anatase. Interestingly, they discovered that at higher temperatures more highly dispersed products are obtained and that the presence of salts such as $SnCl_4$ and NaCl tended to reduce the average grain size, while NH_4Cl led to agglomerate.

Research on the synthesis of nanophase TiO_2 still continues. Starting from the work of Cheng et al., others determined that the phase purity of the products from hydrothermally processed aqueous $TiCl_4$ depends primarily on the precursor concentration and soaking time [50].

In particular a high concentration of $TiCl_4$ favours the rutile phase, while particle size is related mainly to reaction time. Therefore, it is clear that in order to achieve careful control over phase composition and particle size of TiO_2 nanocrystals, the hydrothermal method is a suitable way. Apart the commercial titania P25 used in the chapter 3 and partially in the chapter 4 In this work the home made titania used for the dielectric applications in chapter

5 and for the rest of the chapter 4 was synthesised via hydrothermal method to ensure the crystalline phase uniformity of the particles and to avoid their aggregation subsequent to an eventual high thermal treatment typically needed to obtain rutile nanoparticles when the sol-gel synthesis is used.

References

[1] G. Kickelbick, *Hybrid Materials. Synthesis, Characterization, and Applications*, **2007**, Wiley-VCH Verlag GmbH & Co. KGaA, Weinheim, ISBN: 978-3-527-31299-3

[2] Chen X. and Mao S.S., Chem. Rev. 107 (2007) 2891

[3] Norotsky A., Jamieson J.C., Kleppa O.J., Science (1967) 158

[4] Jamieson J.C., Olinger B., Am. Min. (1969) 54

[5] Zhang H.Z., Banfield J.F., J. Mater. Chem. 8 (1998) 2073

[6] H.Z. Zhang, J.F. Banfield, J. Phys. Chem. B 104 (2000) 3481

[7] Bobyrenko Y.Y. Zh Fis Khim 46 (1972) 1303; Novrotsky A., Jleppa O.J, J. Am. Ceram. Soc. 50 (1968) 623; Mitsihashi T., J. Am. Ceram. Soc. 62 (1972) 1305; Daßler A., Feltz A., Jung J., Ludwig W., Kaiserberger E., J. Therm. Anal. 33 (1988) 803

[8] Kumar P.N., Keizer K., Burggraff A.J., Okubo T., Nagomoto H., Morooka S. Nature 358 (1992) 48; Basca R.R., Grätzel M., J. Am. Ceram. Soc. 79 (1996) 2185; So W.W., Park S.B., Kim K.J., Shin C.H., Moon S.J., J. Mater. Sci. 36 (2001) 4299

[9] Sureh C., Biju V., Mukundan P., Warrier K.G.K., Polyhedron 17 (1998) 3131; Gennari F.C., Pasquevich D.M., J. Am. Ceram. Soc. 82 (1999) 1915; Chan C.K., Porter J.F., Li Y.G., Guo W., Chan C.M.. J. Am. Ceram. Soc. 82 (1999) 566

[10] Linsebigler A.L., Lu G., Yates J.T.Jr., Chem. Rev. 95 (1995) 735; Watson S.S., Beydoun D., Scott J.A., Amal R., Chem. Eng. J. 95 (2003) 213; Mills A., Lee S.K., Lepre A., J. Photochem. Photobiol. A 155 (2003) 199; Habibi M.H., Vosooghian H. J., Photochem. Photobiol., A 174 (2005) 45

[11] Ha P.S., Youn HJ, Jung H.S., Hong K.S., Park Y.H., Ko K.H., J. Colloid Interface Sci. 223 (2000) 16

[12] Chao H.E., Yun Y.U., Xingfang H.U., Larbot A. J. Eur. Ceram. Soc. 23 (2003) 1457

[13] Banfield J.F., Bischoff B.L., Anderson M.A., Chem. Geol. 110 (1993) 211

[14] Gouma P.I., Dutta P.K., Mills M.J., Nanostruct. Mater. 11 (1999) 1231

[15] Serpone N., J. Photochem. Photobiol A: Chem 104 (1997) 1

[16] Rajeshwar K., J. Appl. Electrochem. 25 (1995) 1067

[17] Nosaka Y., Fox M.A., J. Phys. Chem. 92 (1988) 893

[18] Fujishima A., Hashimoto K., Watanabe T., TiO_2 photocatalysis. Fundaments and applications, 1st ed. Tokyo: BKC; 1999; Mardare D., Tasca M., Delibas M., Rusu G.I., Appl. Surf. Sci. 156 (2000) 200

[19] Cozzoli P.D., Comparelli R., Fanizza E., Curri, M.L., Agostiano A., Mater. Sci. Eng. C 23 (2003) 707; Joo J., Kwon S.G., Yu T., Cho M., Lee J., Yoon J., Hyeon T., J. Phys. Chem. B 109 (2005) 15297; Chae S.Y., Park M.K., Lee S.K., Kim T.Y., Kim S.K., Lee W.I., Chem. Mater. 15 (2003) 3326

[20] Kikuchi Y., Sunada K., Iyoda T., Hashimoto K., Fujishima A., J. Photochem. Photobiol. A 106 (1997) 51

[21] Blake D.M., Maness P.C., Huang Z., Wolfrum E.J., Huang J., Jacoby W.A., Sep. Purif. Methods 28 (1999) 1.

[22] A., Le Hunte S., J Photochem Photobiol A: Chem 108 (1997) 1

[23] O., Huisman C.L., Reller A., Progress in Solid State Chemistry 32 (2004) 33

[24] Sclafani A., J. Phys. Chem. 100 (1996) 13655

[25] Kormann C., Bahnemann D.W., Hoffmann M.R., Environ. Sci. Technol. 22 (1988) 798; Hoffmann A.J., Carraway E.R., Hoffmann M.R., Environ. Sci. Technol. 28 (1994) 776; Carraway E.R., Hoffmann A.J., Hoffmann M.R., Environ. Sci. Technol. 28 (1994)786

[26] Chan C.K., Porter J.F., Li Y.G., Guo W., Chan C.M.. J. Am. Ceram. Soc. 82 (1999) 566

[27] Tanaka K., Capule M.F.V., Hisanaga T., Chem Phys Lett 187 (1991) 73

[28] Howe R. F. and Grätzel M. J., Journal of Physical Chemistry 91 (1987) 3906

[29] Hurum D.C., Agrios A.G., Crist S.E., Gray K.A., Rajh T., and Thurnauer M. C., Journal of Electron Spectroscopy and Related Phenomena 150 (2006) 155

[30] Canevali C., Morazzoni F., Scotti R., Bellobono I.R., Giusti M., Sommariva M., D'Arienzo M., Testino A., Musinu A. and Cannas C. International Journal of Photoenergy Volume 2006, Article ID 90809, Pages 1–6

[31] Berberick L.J., Bell M.E., Journal of Applied Physics, 11, (1940), 681

[32] Schmidt, Ann. d. Physik, 14, 9, (1902), 919

[33] Tang. H, Prasad K., Sanjinès R., Schmid P. E., Lévy F., J. Appl. Phys., 75(4), 1994, 2042

[34] Carp O., Huisman C.L., Reller A., Progress in Solid State Chemistry 32 (2004) 33

[35] Watson S.S., Beydoun D., Scott J.A., Amal R., Chem. Eng. J. 95 (2003) 213

[36] Bach U., Lupo D., Comte P., Moster J.E., Weissortel F., Salbeck J., Nature 395 (1998)583

[37] Livage J., Henry M., Sanchez C., Prog. Solid State Chem. 18 (1988) 259; Sugimoto T., AdV. Colloid Interface Sci. 28 (1987) 65; Anderson M.A., Gieselmann M.J., Xu Q.J., Membr. Sci. 39 (1988) 243; O'Regan B., Grätzel M., Nature 353 (1991) 737; Kormann C., Bahnemann D.W., Hoffmann M.R., J. Phys. Chem. 92 (1988) 5196; (a) Barringer E.A., Bowen H.K., Langmuir 1 (1985) 414 (b) Barringer E.A., Bowen H.K., Langmuir 1 (1985) 420; Jean J.H., Ring T.A., Langmuir 2 (1986) 251; (a) Look J.L., Zukoski C.F., J. Am. Ceram. Soc. 75 (1992) 1587 (b) Look J.L., Zukoski C.F., J. Am. Ceram. Soc. 78 (1995) 21; Vorkapic D., Matsoukas T.J., Am. Ceram. Soc. 81 (1998) 2815; Vorkapic D., Matsoukas T.J., Colloid Interface Sci. 214 (1999) 283; Penn R.L, Banfield J.F., Geochim. Cosmochim. Acta 63 (1999) 1549; Barbé C.J., Arendse F., Comte P., Jirousek M., Lenzmann F., Shklover V., Grätzel M., J. Am. Ceram. Soc. 80 (1997) 3157

[38] Campostrini R., Ischia M., Palmisano L., J. Therm. Anal. Cal. 75 (2004) 13

[39] Legrand-Buscema C., Malibert C., Bach S., Thin Solid Films 418 (2002) 79

[40] Song K.C. and Pratsinis S.E., J. Am. Ceram. Soc., 84 (2001) 92

[41] Li Y., White T.J. and. Lim S.H, Journal of Solid State Chemistry 177 (2004) 1372

[42] Bacsa R.R., Kiwi J., Appl. Catal. B: Environ. 16 (1998) 19

[43] Pottier A., Cassaignon S., Chaneac C., Villain F., Tronc E., Jolivet J.P., J. Mater. Chem. 13 (2003) 877

[44] Niederberger M., Bartl M.H., Stucky G.D., Chem. Mater. 14 (2002) 4364

[45] Koelsch M., Cassaignon S., Ta Thanh Minh C., Guillemoles J-F., Jolivet J.-P, Thin Solid Films 451-452 (2004) 86

[46] Yu S.H., J. Ceram. Soc. Jpn. 109 (2001) S65; Cansell F., Chevalier B., Demourgues A., Etourneau J., Even C., Garrabos Y., Pessey V., Petit S., Tressaud A., Weill F.J., Mater. Chem. 9 (1999) 67; Rajamathi, M.; Seshadri, R. Curr. Opin. Solid State Mater. Sci. 2002, 6, 337.; Gautam U. K., Ghosh M., Rajamathi M., Seshadri R., Pure Appl. Chem. 74 (2002) 1643; Demazeau G.J., Mater. Chem. 9 (1999) 15; Li J., Chen Z., Wang R.-J., Proserpio D.M., Coord. Chem. Rev. 190-192 (1999) 707

[47] Hakuta Y., Ura H., Hayashi H., Arai K., Ind. Eng. Chem. Res. 44 (2005) 840

[48] Cheng H., Ma J., Zhao Z. and Qi L., Chem. Mater. 7 (1995) 663

[49] Oguri Y., Riman R.E., Bowen H.K., J. Mater. Sci. 23 (1988) 2897

[50] Yanquing Z., Erwei S., Zhizhan C., Wenjun L., Xingfang H., J. Mater. Chem. 11 (2001) 1547

CHAPTER 2

Aims and Development of the Work

In the past decades many papers reported the use of the TiO_2 for different applications. The photocatalytic applications involving titania nanoparticles are one of the most attractive field because the potential huge impact in an industrial context. In fact the ability of titania nanoparticles to promote photoreducing/oxidizing reactions with organic and inorganic matter, as described on the paragraph 1.5.1, allows the possibility to use this kind of material for pollutants reduction in many industrial processes such as purification of water and air.

In this context the high photocatalytic performances reached by the different kind nanoparticles developed in the past years collided with the direct inapplicability of the particles for industrial applications: being the particles nanodimensioned the spreading risk in the environment could be an additional problem despite the chemical inertia of the titanium oxide. An additional limitation for industrial purposes using nanoparticles is the high separation and recovering costs of the catalyst. The natural technical response to bypass these industrial limitations is the immobilization of the catalyst on a support or embedding it in a matrix. The direct immobilization on a support, involving high temperatures and then the formation of chemical bonds between the particles, showed as drawback the reduction of the active surface in charge to react with pollutants, as detailed on paragraph 1.3. So that the catalyst immobilization could be the only possible way to preserve the exposed surface of the oxide avoiding its spreading on the environment.

The first part of the work, the chapter 3, is focused on the preparation of an organic membrane embedding commercial neat titania nanoparticles. The incorporation into an organic matrix implies a chemical activity between the catalyst and the organic matrix itself i.e. the matrix is degraded as well as the pollutants. These interactions involving radical species are studied in details by EPR measurements.

In order to avoid the degradation of the matrix described in the chapter 4, in the chapter 5 is described a new material where the TiO_2 nanoparticles are embedded in a silica matrix obtaining a composite inorganic/inorganic material. Being silica a stable oxide the degradation phenomena highlighted using an organic matrix are completely avoided. To assure the accessibility of the pollutants to the catalyst the material should be porous and the nanoparticles should not be completely embedded into the matrix. The porosity of the silica is obtained using a sacrificial templating polymer: PEG. During the SiO_2 sol-gel synthesis the different solubility of the polymer and of the silica are exploited to create a hybrid *Class I* material. After calcination the voids left by the polymer chains confer the desired porosity to the material. Creating this material the concepts explained in the paragraph 1.3 are extensively applied and studied. In order to avoid the embedding of the TiO_2 nanoparticles in the matrix their surface was previously functionalized with some different organic molecules to drive their behavior during the material formation. The functionalized particles can be considered a *Class II* material. The different surface functionalizing molecules as well the different catalytic conditions for the silica formation are studied playing a crucial role on the final morphological and photocatalytic properties of the material. The obtained material shaped in form of pellets is tested for water purification from phenol and for air purification in order to remove the NOx contamination.

The same reaction technique used to functionalize the nanoparticles in the chapter 4 is used, in the chapter 5, to functionalize some rutile titania nanoparticles with a RAFT reagent. The reagent allows to lead a “polymerization from” reaction of styrene. The polystyrene chains are growth starting the reaction in the proximity of the surface thanks to the peculiarity of the transfer polymerization reagent (RAFT) anchored on the surface. The obtained material, i.e. the nanoparticles, are surrounded by a dense covering layer of

polymer. Following the classification of the Chapter 1 the functionalized nanoparticles are a *Class II* material and being nanoparticles the final material is a nanocomposite. The obtained nanocomposite is used as dielectric material exploiting the high dielectric constant of the rutile TiO_2, as described in the paragraph 1.5.2. The nanocomposite material showed a dielectric behavior related to some percolative phenomena which are evidenced by the electric measurements and subsequently related to the morphology of the material.

In conclusion the present work, despite it covers three different materials, is organized focusing the attention on the application of the principles explained on the introduction regarding the hybrid and nanocomposite materials. The phenomena involved to realize hybrid and nanocomposite materials are exploited to modify the material in order to optimize its performances.

CHAPTER 3

TiO_2-Polymeric Membranes for Photocatalysis

3.0 Introduction

As described in the paragraph 1.5.1 the titanium dioxide's capability to catalyze oxidative processes under UV irradiation is widely studied, as it concerns its efficacy and its mechanism[1].

Literature is mainly focused on the investigation of different chemical routes[2], e.g hydrothermal[3] or sol-gel[4], and of physical methods[5] to prepare nanostructured TiO_2; moreover, the various strategies to dope TiO_2 by transition[6] and non transition[7] elements, thus allowing photoactivation under visible light, have been thoroughly investigated however the obtained results were just a bathochromic shift of the photoactivation radiation leading to a slight absorption at the lowest wavelength range of the visible spectrum.

The main guideline to optimize the catalyst performances seems to be the improvement of its ability to keep the charges induced by irradiation, holes and electrons, separated [8]. In fact, the reductive and oxidative processes at the surface of TiO_2 may be enhanced by hindering the electron-hole recombination, d-e processes reported in Fig. 1.8.

However, for large-scale use of the catalyst, either in liquid and gas phase reactions, it is necessary to provide an easy recovery of it, while powdered oxide is definitely not the most suitable material for industrial applications. The huge recovering costs of a nanodimensioned powder and its environmental risks, despite the chemical inertia of TiO_2, limited up to now its industrial application.

Different TiO_2 hosts were proposed, inorganic[9] or polymeric[10], being careful that the host was able to fully retain the catalyst, at the same time allowing complete passage of products and light. Generally, the use of polymeric membranes to entrap inorganic catalysts shows specific practical advantages: i) the catalyst is embedded into the membrane without any covalent bond formation, thus avoiding its chemical modification; ii)

polymeric membranes show different affinities for different chemicals, therefore the absorption and the diffusion of the reactants can be modulated; iii) the photocatalytic degradation process may be performed in a system in which reaction and separation processes occur in a single stage; iv) finally, all advantages of true membrane processes, such as modularity, design and easy scale–up, may be attained.

Among the most innovative materials to immobilize both homogeneous and heterogeneous catalysts, polymeric membranes have been profitably utilised, constituted by acrylates and metacrylates copolymerized with other photoreactive monomers and/or pre-polymers, grafted onto suitable supports, either polymeric and composites or others[11]. These materials are light weight, have good mechanical properties, depending mainly on the choice of the support, have easy formability, as well as convenient resistance to aging and chemicals under suitable conditions. The embedding of the catalyst i.e. titania nanoparticles led to the realisation of a nanocomposite material if the particles dimensions are preserved during the embedding into the polymeric membrane. In fact, as explained in the paragraph 1.3, if the particles aggregate, because the different affinity of the surface with the polymeric precursors of the matrix, and considering these aggregates as larger particles we cannot define this material as a nanocomposite but just as a composite.

In spite of the relevant use of the membranes in several photooxidative processes, no adequate investigations on the action mechanism of the embedded catalysts and on the fate of photoactive species during the reaction have been performed yet. The catalytic reactions act at the surface of the inorganic particles and then, considering these phenomena under the point of view of the composite material the interphases, between the inorganic/organic counterparts, are one of the crucial parameters regarding not also

the realisation of the composite e.g. the aggregation of the catalyst but also the performances of the material.

In the present chapter, it is reported a combined kinetic and mechanistic study of TiO_2 embedded in polyester acrylate membranes, produced by photografting process and tested in the phenol mineralization by using molecular oxygen as the oxygen donor, a typical process for the removal of environmental chemical contaminants. Phenol, as a model of aromatic compounds, was chosen among other organic pollutants due to its use as a raw material in many petrochemical, chemical, and pharmaceutical industries. Moreover, due to their stability, high toxicity and carcinogenic properties, phenolic compounds have caused considerable damages and threats to the ecosystem and human health. Therefore, their removal from wastewater is a point of great interest, as demonstrated by the huge number of studies focused on their photodegradation and on the detection of the intermediates formed during the degradation reactions[12].

In the present study, the kinetic behaviour of the embedded TiO_2 catalyst was compared to the same powdered catalyst used in slurry in the phenol photomineralization. The charge carriers formed by UV irradiation were detected by EPR (Electron Paramagnetic Resonance), and their amount and stability were related to the photochemical efficiency in order to describe the catalytic mechanism of TiO_2 embedded into polymeric membranes and to suggest a rationale for the most suitable embedding. The aim has also been to show that the inclusion of TiO_2 into polymeric membranes not only allows easy manipulation of the catalyst, since the polymeric membrane is able to fit the reactor's shape very conveniently and to keep the photocatalyst at the interface in the closest contact with the reaction solution, but also, surprisingly, that the catalyst is assisted by the membrane and by O_2 in keeping the holes separated from the electrons, during the irradiation process. In particular, the interaction of holes with the polymeric membrane

results in the formation of peroxy radicals which can be considered responsible for the stabilization of both holes and electrons (trapped on Ti^{3+} centres). Similar modifications of the electronic properties of the embedded catalyst are fully unexpected and open new directions for the photoactivity control.

3.1 Preparation

Patented photocatalytic membranes containing TiO_2 (*PHOTOPERM BIT*/313® by BELLOBONO INNOVATIVE TECHNOLOGIES, B.I.T. srl, Milan, Italy) were prepared by a photografting process[13]. The photografted process is based on UV induced polymerization of polymer precursor previously mixed with the nanoparticles.

A polyester multifunctional acrylate patented blend, in which the acrylate group was the main photoreactive moiety, was photografted by a UV photoinitiating system added to the mixture. The final blend was air-sprayed onto polypropylene non-woven tissue and cured under UV light for a very rapid photografting. A final overall loading of 101±10 g/m^2 of membrane containing a P25 (Degussa) TiO_2 based photocatalyst was obtained. After 96 hours at RT the grafted tissue was stored 16 hours at 55°C to remove the eventual traces of solvents.

The final loading of TiO_2 into the photografted polymer was determined by Thermo Gravimetric Analysis (TGA) measurement (Air gas flow = 50 cm^3 min^{-1}, 10°C/min, 30-1000°C) by Mettler Toledo TGA/DSC1 STAR^e System; it resulted 36.0 wt% in acceptable agreement with the nominal content of the starting mixture. The Thermogravimetric analysis measures the weight loss of a material during the heating of the sample. Being the material based on a polymer mixed with an inorganic material, increasing the temperature in air the organic counterpart burns and the final weight is just done by the inorganic particles. The difference between the pristine sample and the final weights gives the inorganic/organic ratio.

3.2 Morphological Characterization Techniques

3.2.1 X-Ray Diffraction (XRD)

X-ray diffraction (XRD) diffraction is usually used to identify the different phases of inorganic compounds and can be used for hybrid and nanocomposite materials too. Every single substance has a specific diffraction pattern i.e. the position and the intensity of the peaks can be considered as fingerprints of a substance. Electronic databases such as Inorganic Crystal Structure Database (ICSD) or JCPDS (Joint Committee on Powder Diffraction Standards) are used for comparison. If the powder crystallites are very small the pattern peaks are broad. Appling the Debye-Scherrer equation to the peak broadening it is possible to determine the crystallite dimension:

$$d = \frac{k\lambda}{B\cos\theta} \qquad 1$$

where k is a factor usually set to 0.9, λ is the wavelength of the radiation, B is the diffraction line broadening measured at the half of the maximum intensity (radians) and θ is the Bragg angle.

X-ray diffraction (XRD) patterns of TiO_2 powders were collected with a Bruker D8 Advance diffractometer (Cu Kα radiation) operating in the range 10-60° 2θ (2θ step 0.020°, counting time 2s per step).

3.2.2 SEM and TEM Characterization

Scanning Electron Microscopy (SEM) produces images of a surface. The signal used to reconstruct the images comes from the inelastic interaction between the surface atoms of the sample and the electrons thermoemitted by a filament. The emitted electrons are

detected to reconstruct the image. The boustrophedon movement (from the greek βουστροφηδον, it is the movement right-to-left and then left-to right one line below) of the electron beam scanning the surface giving 3-D appearance image of the specimen. Beside the emitted electrons X-rays are also produced by the interaction of the electrons with the surface. The emitted X-rays can be detected by a EDX (Energy Dispersive Spectroscopy) equipment providing some information about the sample composition. The spatial resolution of the SEM techniques is related to the machine parameters and generally varies between 20-1 nm.

In Transmission Electron Microscopy (TEM) the images are produced by focusing the electron beam into a thin specimen. Some electrons are transmitted carrying the structure information. Generally the low contrast caused by the weak interaction of the electrons with the electronic cloud of organic material atoms limits this technique to the study of inorganic compounds. If the analyzed material is crystalline a diffraction pattern can be observed and some more information inherent the material can be extrapolated. Generally the resolution of a TEM is lower than a SEM but modern High Resolution TEM (HRTEM) can go down to a resolution below 0.1 nm. The scanned area of TEM has less extent than that of SEM.

Scanning electron microscopy (SEM) measurements were performed by a LEO 1450VP instrument both on powders and on embedded catalysts.

High-resolution transmission electron microscopy (HRTEM) and electron diffraction (ED) measurements were performed using a Jeol 3010 apparatus operated at 300 kV with a high-resolution pole piece (0.17 nm point to-point resolution) and equipped with a Gatan slow-scan 794 CCD camera. The powders were suspended in isopropanol, and a 5 μL drop of this suspension was deposited on a holey carbon film supported on 3-mm copper grid for TEM investigation.

3.3 Photochemical Activity: Phenol Degradation in Water

Photodegradation experiments were carried out in a designed discontinuous batch photoreactor, as described in a previous study and reported in Figure 3.1.[14]

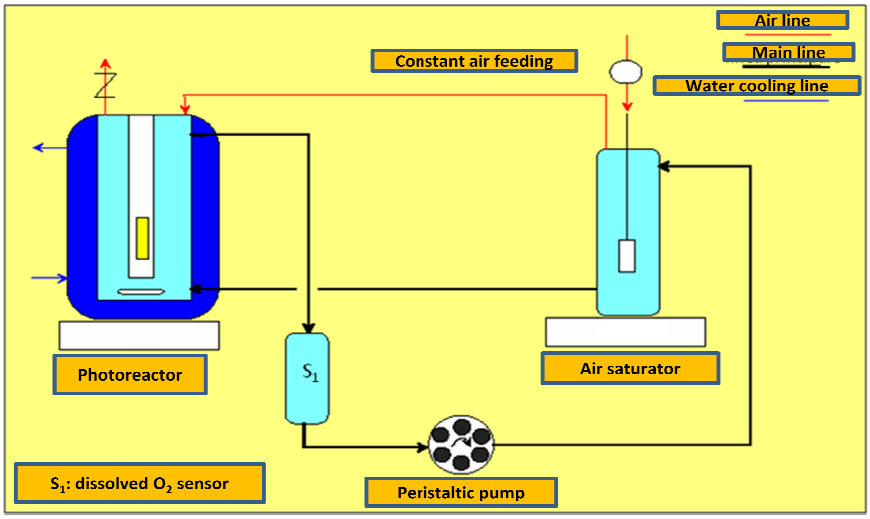

Figure 3.1. The photoreactor equipment used to study the phenol degradation in water. The membrane is inserted around the coaxial lamp contained in the photoreactor. The peristaltic pump provide the continuous and constant recirculation of the water solution containing phenol while the air saturator provide the oxygen needed for the photocatalysis reaction.

The reactor (600 ml), provided with an external cooling jacket, was equipped with a UV 125 W Hg high pressure lamp, placed in a coaxial quartz cylinder. No optical filter was adopted.

Photocatalytic tests were performed in water solution by using O_2 as the oxygen donor and operating either with TiO_2 embedded in Polymeric Membranes (TPM) or with TiO_2 Powder Slurries (TPS) as catalysts.

In the former case the membranes (size 20 cm x 10 cm; catalyst loading 0.720 g, corresponding to 1.20 g L^{-1}) were cylindrically folded and placed inside the batch reactor at 1 cm from the coaxial UV lamp. PhOH solution (600 mL containing 121±2 mg·L^{-1} of PhOH, 93±2 mg·L^{-1} as C) was recirculated by a peristaltic pump with a speed of 14 mL s^{-1}. The

temperature was kept at 25 ± 2 °C; pH and dissolved oxygen content of the suspension were monitored by on-line sensors.

In the case of the slurry, TiO_2 powder (160±5 mg; 0.25 $g \cdot L^{-1}$) was suspended by sonication in 600 mL of water containing the same concentration of PhOH and recirculated with the same speed and at the same temperature as in the experiments with membranes. It was verified that the catalyst loading in the range 0.2-1.4 $g \cdot L^{-1}$ did not affect the kinetics parameters of PhOH mineralization .

The slurry was circulated in the dark and saturated in an on-line chamber by continuously bubbling oxygen (100 mL min^{-1}). The oxygen content became maximum and constant in about 10 min. The reaction was performed by keeping the oxygen feed constant and by eliminating the excess gas through a non return check valve.

The UV source was turned on after 1 hour of recirculation in the dark .The PhOH absorption on the catalyst was checked by withdrawing suspension aliquots (6 mL) of the solution at regular intervals, analyzing the total organic carbon (TOC) by a Shimadzu TOC-V CSH analyzer. The same procedure was applied to monitor the kinetics of photoinduced PhOH degradation until the complete mineralization of the substrate. In the case of the slurry, TiO_2 powder was separated by centrifugation before TOC analysis. Finally, reference experiments were carried out in the absence of TiO_2 and TPM (Blank).

3.4 EPR Study Method of the Photochemical Activity

The EPR investigation was performed by a Bruker EMX spectrometer working at the X-band frequency and equipped with an Oxford cryostat working in the range of temperature 4–298 K.

The powder samples (P25 powder and P25 embedded in polymer matrix scratched from the polypropylene tissue) were contained within quartz glass tubes connected both to a high vacuum pumping system and to a controlled gas feed (O_2).

Spectra were recorded in vacuum conditions (10^{-5}mbar) at 130 K, before and after 10 min of UV-irradiation at the same temperature inside the EPR cavity. No significant differences resulted between the spectra recorded just before and 20 min after switching off the UV irradiation, except a small decrease of the signal intensity.

Modulation frequency was 100 kHz, modulation amplitude 2–5 gauss, and microwave power 2-5 mW. Irradiation was performed by UV 150W Xe lamp (Oriel) with the output radiation focused on the samples in the cavity by an optical fiber (50 cm length, 0.8 cm diameter).

The g values were calculated by standardization with α,α'-diphenyl-β-picryl hydrazyl (DPPH). The spin concentration was obtained by double integration of the resonance lines, referring to the area of the standard Bruker weak pitch ($9.7 \cdot 10^{12}$ ± 5% spins cm^{-1}). Care was taken in order to always keep the most sensitive part of the EPR cavity (1 cm length) filled.

Spectra simulation and fit were performed using the SIM 32 program[15].

3.5 Discussion and Results

Morphological characterization of the membranes

As expected the XRD diffraction peaks of the membranes were revealed just the titania peaks indexed as rutile TiO_2 (JCPDS, no. 21-1276), and anatase (JCPDS, no. 21-1272). The average crystallite size of TiO_2 was estimated from the broadening of the XRD peaks [110] for rutile and [101] for anatase, by means of the Scherrer equation.

The TiO_2 phase composition and the particle size in TPM samples, determined by XRD, were analogous to those of P25 powder (Anatase= 80%, average size = 22 nm; Rutile =

20%, average size = 37.5 nm). This indicates that the crystalline structure of titania powder is not affected by the embedding in membrane (See Figure 3.2).

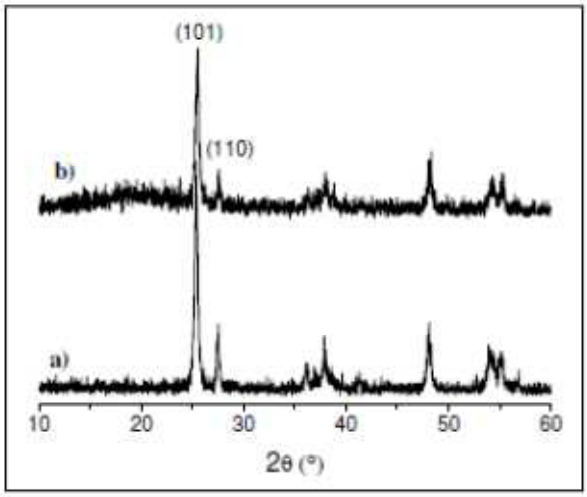

Figure 3.2. XRD patterns of a) P25 and b)TPM.

The surface morphology of TPM membranes, before and after washing with H_2O_2 under UV irradiation (see Figure 3.5), was investigated by SEM. Before washing, the membrane surface appeared non-porous and the polymer fully covered P25 crystallite aggregates (Figure 3.3a), presumably hindering the interactions between titania nanoparticles and the adsorbed pollutant. After H_2O_2 treatment (Figure 3.3b), TiO_2 aggregates became visible and organized in a porous structure, thus allowing nanoparticles more easily catalyze the photodegradation.

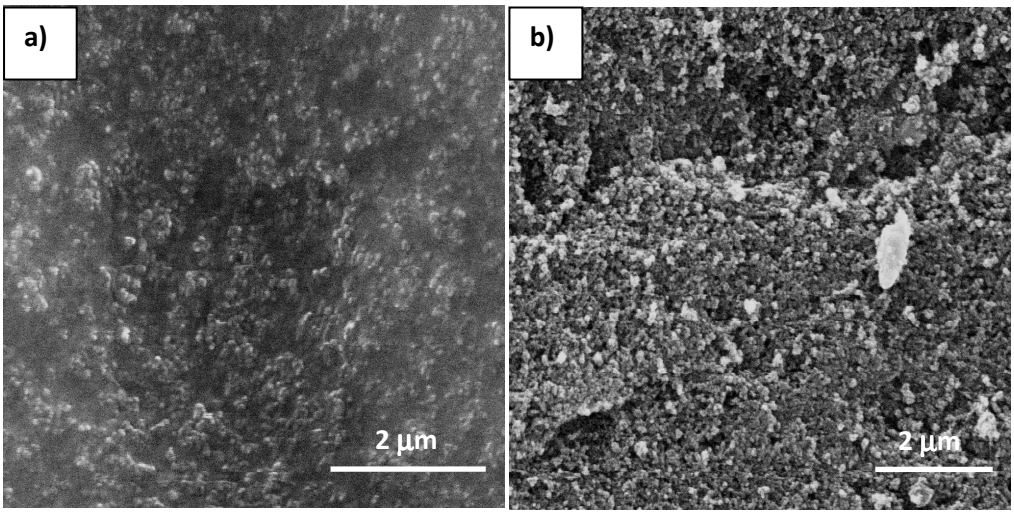

Figure 3.3. SEM micrographs of TPM membranes, before and after washing with H_2O_2 under UV irradiation

TEM and HRTEM micrographs of selected TPMs are reported in Figure 3.4.

According to the results obtained by SEM, TiO_2 nanoparticles in TPM sample before UV-treatment in H_2O_2 appear heavily covered by the membrane (Figure 3.4a). Conversely, TPMs subjected to the washing process (Fig. 3.4b) and 6 runs of photooxidation (Figure 3.4c), show anatase and rutile nanoparticles embedded into the membrane, but not coated. This allows them to be easily irradiated and to interact with the reactants. The oxide grains are often surrounded and separated by the polymer matrix (Figure 3.4d). However, the intimate contact between anatase and rutile nanocrystals is preserved (Figure 3.4 e and f).

TEM and HRTEM micrographs reveal rutile particles with irregular shapes, generally larger than anatase, grown in the [001] direction (Fig. 2e). Anatase nanoparticles appear more regular, and the fringes corresponding to the [101] crystallographic planes are most frequently observed (Figure 2 f).

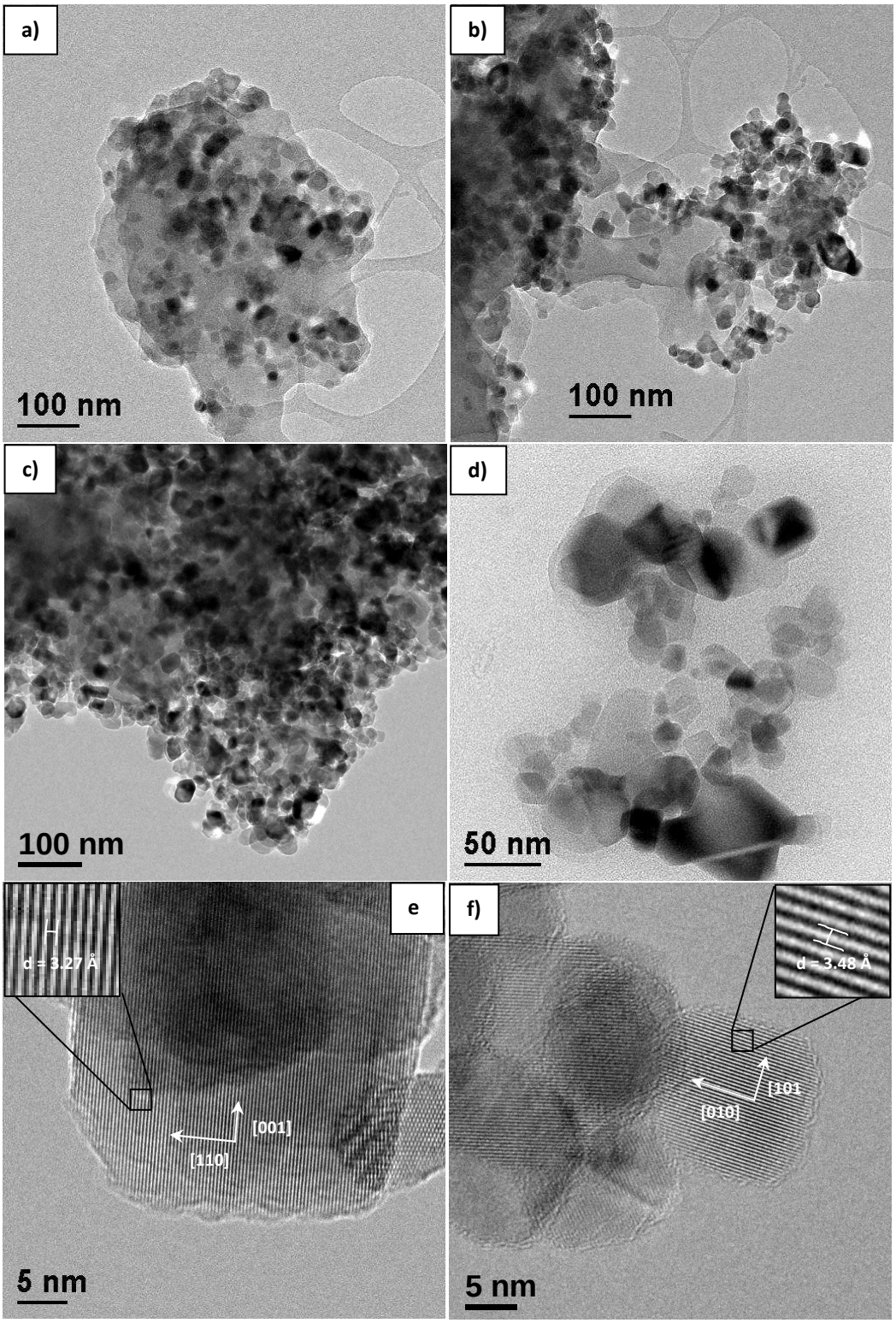

Figure 3.4. TEM micrographs of TPM membranes: (a) before and (b) after washing treatment with H_2O_2 under UV irradiation; (c, d) after 6 runs of phenol photooxidation. HRTEM micrographs of (e) rutile and (f) anatase nanocrystals in TPM.

Photocatalytic activity

Before carrying out photocatalytic tests the as prepared membranes were washed in the photoreactor for 24 h with a solution of H_2O_2 2M under UV irradiation in order to fully remove the non-polymerized monomeric/oligomeric species. At the end of the washing process, residual organics, eventually released in solution and monitored as Total Organic Carbon (TOC), were found to be substantially absent. (See Figure 3.5)

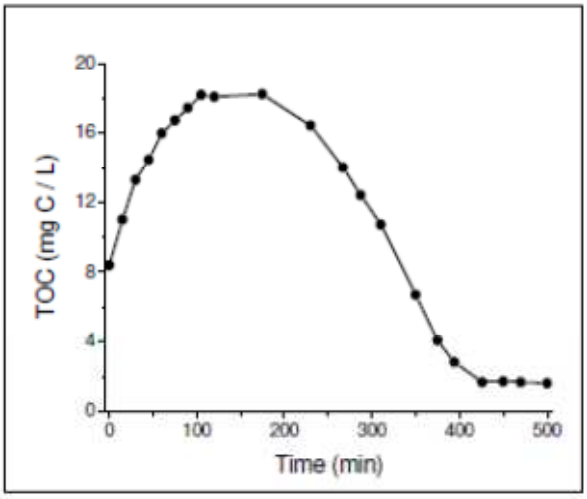

Figure 3.5: TOC release during the initial washing process of TPM in H_2O_2 under UV irradiation

The TPM photocatalytic activity in the PhOH mineralization was measured in water solution and compared with that of TPS. The photocatalytic tests were performed by repeating six successive degradation runs, in order to validate the reproducibility of the TPM catalytic behaviours. In all the performed experiments, during the initial stage of recirculation in the dark (60 min), the phenol absorption on the membrane leads to depletion of the loaded PhOH of about 5.0±2 %. The experimental data related to TOC disappearance and the fitted curves of PhOH mineralization for both TPM samples (runs 1 and 6) and TPS are reported in Figure 3.6a. The blank test is also reported for comparison.

The catalyst activity was evaluated by measuring the maximum degradation rate $(dC/dt)_{max}$, which corresponds to the maximum slope point of the fitted curves and the half

degradation time $t_{1/2.}$ Both $(dC/dt)_{max}$ and $t_{1/2}$ values were normalized to the same mass (160 mg) of TiO_2 .

The trends of the calculated values of $t_{1/2}$ and $(dC/dt)_m$ for TPMs are reported in Figure 3.6b. The results demonstrate that TPMs have significant photocatalytic activity in phenol degradation, even if it is lower than that of the powdered TPS. In particular, $t_{1/2}$ decreases and $(dC/dt)_{max}$ increases in the first three runs, then they remain constant and centered on the highest value in the successive runs.

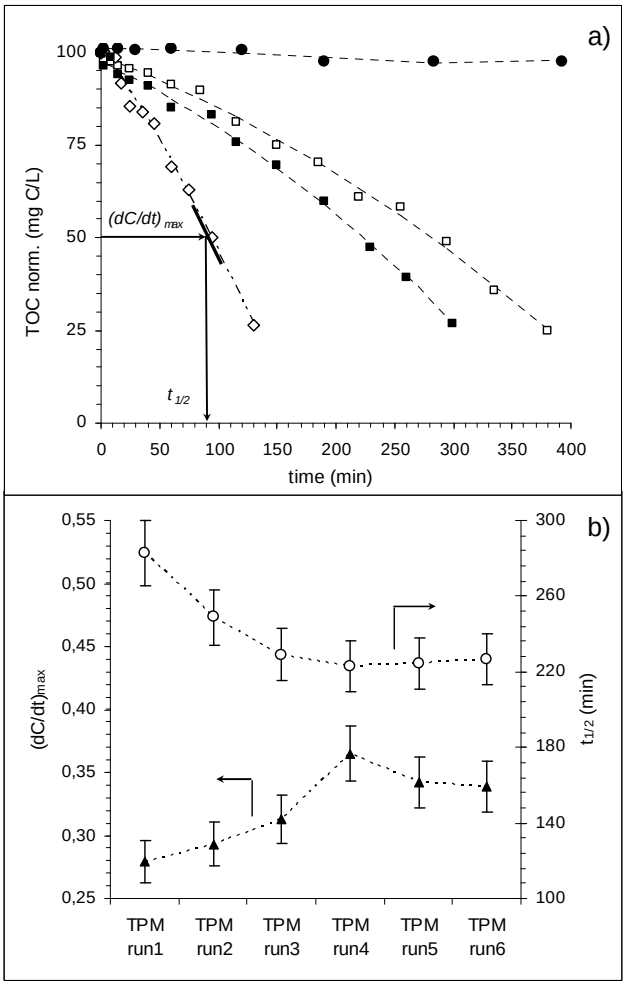

Figure 3.6. (a) Mineralization curves of phenol (given as TOC%) under UV irradiation in the presence of O_2 of: (●) blank, without catalyst; (□)TPM, first run; (■)TPM, sixth run; (◇) P25 slurry.

(b) Maximum degradation rate $(dC/dt)_{max}$ and half degradation time $t_{1/2}$ of six successive degradation runs.

In the blank test without the catalyst the PhOH mineralization rate is very low, thus indicating a negligible contribution of the direct PhOH photolysis to the whole process.

The overall results confirm that the polymeric membrane does not substantially affect the peculiar photocatalytic properties of the embedded P25.

In a previous investigation[14] about the effects of the immobilization process on the photocatalytic activity, aggregation and coarsening of the oxide nanoparticles were demonstrated to induce a severe depletion of the photoactivity. In that work P25, immobilized on glass fibers, was tested in the same conditions as TPSs. Its photoefficiency was really quenched ($t_{1/2}$ = 524 min, $(dC/dt)_{max}$= 0,220), and this effect was ascribed to the formation of compact nanoparticle aggregates. Conversely, P25 nanocrystals embedded in the TPMs undergo less coarsening effects and maintain higher free surface, suitable both for UV irradiation and to the adsorption/reaction of PhOH substrate (see Fig.3.4 b and c), thus improving the overall catalytic efficiency of TPMs ($t_{1/2}$ = 295-225 min, $dC/dt)_{max}$= 0,360-0.275).

EPR investigation

EPR spectra were carried out on P25 powder and on TPMs. Membranes were examined before and after successive runs of photocatalytic tests six hour long.

In order to characterize and to study the stability of photogenerated electrons and holes, all samples were UV irradiated at 130 K either in vacuum ($p<10^{-5}$mbar) (Figure 3.7 line b, Figure 3.8) and under oxygen atmosphere (7 mbar) (Figure 3.7 line c, Figure 3.8). In the latter case, residual O_2 was removed by evacuation at 10^{-5} mbar before acquisition of the EPR spectra.

Finally, to simulate the photografting process undergone by the TPM membranes during the preparation, P25 nanopowder was subjected to UV irradiation at 298 K in the presence of 20 mbar of O_2 in the EPR cavity. After this treatment, the excess of oxygen was

removed by evacuation at 10^{-5} mbar and the spectra were acquired before and after UV irradiation in vacuum at 130 K (Figure 3.7 lines d, e).

The main results obtained from the EPR spectra of powdered P25 are reported below.

i) Before UV irradiation in vacuum (Figure 3.7, line a), the spectrum showed a broad signal, centered at g =1.979, very similar to that described by Gray et al. and interpreted as a tetrahedrally distorted Ti^{3+} center in the interfacial region between rutile and anatase of P25 [16].

ii) After irradiation in vacuum, the total amount of Ti^{3+} species increases (Figure 3.7 line b). The spectrum is complex, due to the superimposition of three different resonances: broad lines attributable to Ti^{3+} in the interfacial region; resonance lines at g = 1.989, corresponding to the perpendicular g-tensor component of anatase Ti^{3+} centers ($g_{\|}$ is not detectable due to overlap with the other lines)[16, 8a, d]; finally an intense feature with $g_{\perp}$ = 1.964 and $g_{\|=}$ 1.946, assigned to Ti^{3+} centres in rutile[16,17]. These result are in agreement with our previous EPR investigations on phase controlled hydrothermal samples[4,18]. It turned out that Ti^{4+} centres of rutile are more able to trap photogenerated electrons with respect to those of anatase whatever the amount of anatase in titania. This suggested an electron transfer occurring from the higher energy conduction band states of anatase to those of rutile lying at lower energy. Finally, no signals associated with surface trapped holes in titania (O^- species) were detectable.

iii) The main difference observed after irradiation of P25 under O_2 (7 or 20 mbar) is the disappearance of the rutile electron trapping sites probably due to photooxidation, while Ti^{3+} centres associated to the anatase phase are still visible in the spectrum. Moreover, a new signal attributable to two different Ti^{4+}-

O_2^- species[8b, d, 19] ($g_{1(A)}$ = 2.037, $g_{1(B)}$= 2.022 g_2 = 2.008, g_3= 2.001) becomes evident (Figure 3.7 line c).

iv) The spectrum acquired in vacuum at 130 K, after the irradiation at 298 K in the presence of 20 mbar of O_2, shows the resonance lines of the O_2^- species chemisorbed on TiO_2 (Figure 3.7 line d). The subsequent UV-irradiation in vacuum, generates only the Ti^{3+}centers associated to the anatase phase, while the intensities of superoxide features remain more less constant (Figure 3.7 line e). This suggests that photooxidation of P25 at room temperature bleaches the electron trapping sites of rutile, more vulnerable to oxidation reactions.

In order to compare Ti^{3+} centres detected in P25 with those in membrane embedded-TiO_2 nanoparticles, EPR spectrum of a selected TPM sample irradiated in vacuum under the same conditions as P25 was reported (Figure 3.7, line f). Significantly, TPM shows the same Ti^{3+}centers associated to anatase and interfacial tetrahedral trapping sites reported in Fig 4e for P25. This demonstrates that the photografting process undergone by the TPM membranes acts as photooxidation causing the annihilation of rutile Ti^{3+} sites.

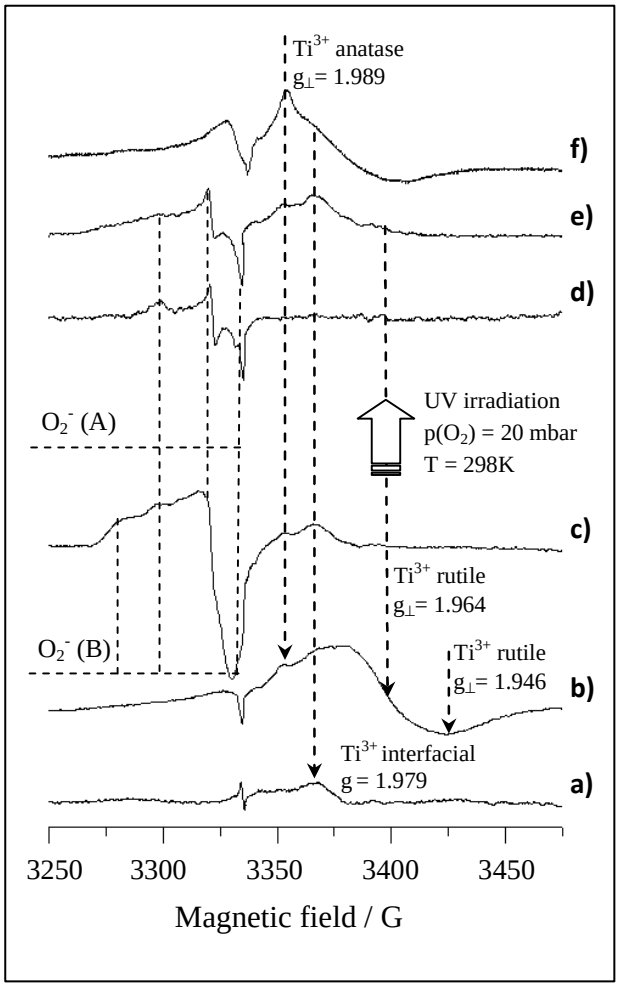

Figure 3.7. P25 spectra before (line a) and after UV irradiation either in vacuum ($p<10^{-5}$mbar) (line b) and under 7 mbar of O_2 (line c). Spectra were acquired at 130 K after evacuation at 10^{-5} mbar.

P25 was subjected to UV irradiation at 298 K in the presence of 20 mbar of O_2 in the EPR cavity. After this treatment, the excess of oxygen was removed by evacuation at 10^{-5} mbar and the spectra acquired before and after UV irradiation in vacuum at 130 K (lines d, e). EPR spectrum of a selected TPM sample irradiated under vacuum under the same conditions is also reported (line f). Dashed lines are guide to detect the different paramagnetic species

Figure 3.8A and 3.8B show the EPR spectra of selected TPM samples irradiated in vacuum and under 7 mbar of O_2, respectively. Specifically the spectra of TPM after 30' of the first photocatalytic run and after completion of the first and the sixth run were shown. The spectrum of a membrane without P25, undergone the same treatments, was also

reported for comparison (Figure 3.8AB line a). The most significant results for TPMs are the following:

i) After irradiation in vacuum (Figure 3.8A line a), EPR spectra show resonance lines attributable to a radical species associated to the polymer matrix (see later).

ii) The Ti^{3+} signal arises in the TMP after 30' of the first photocatalytic run (Figure 3.8A, line b), and its intensity increases after the conclusion of the run (Figure 3.8A, line c), then slightly decreases in the sample which completed the sixth test.

iii) Irradiation under oxygen leads to the increase of the radical amount associated to the polymer matrix and unexpectedly, of the Ti^{3+} quantity which becomes much higher than that observed for P25 after the same treatment (Figure 3.8B, lines b, c and d, Figure 3.9). These results suggest that in TPM photogenerated holes are effectively trapped by the polymeric matrix, while electrons are involved in reduction of Ti^{4+} to Ti^{3+} centres. Thus, the membrane is strongly effective in keeping the electron and hole charges separate.

iv) Figure 5 C reports the deconvolution of EPR signals of selected TPMs, after the completion of the first and the sixth run. They reveal the presence of different paramagnetic components: one isotropic line at g_{iso} = 2.0028 relatable to a C-centered species and two superimposed anisotropic signals at $g_{||}$= 2.032, $g_{\perp}$= 2.0024 (species P[I]) and at $g_{||}$= 2.022, $g_{\perp}$= 2.0024 (species P[II]) attributable to peroxy radicals[20]. It is worth noting that the relative amount of peroxy radicals increases with the number of photodegradation runs and becomes predominant after the last (Figure 3.8B line d). On the other hand, the C-centered species dominates in the initial steps of the reaction, then it decreases (Figure 3.8B, line b). This suggests that holes, reacting with the covalent bonds of the

membranes, first form C-centred radicals and then their interaction with O_2 gives rise to the generation of peroxy radicals.

v) The oxygen interaction with C-centered radicals to form peroxy radicals seems to be the driving force which keeps the UV induced charges separate.

The trend of the relative amounts of the paramagnetic species in TPM and P25 samples are shown in Figure 3.9

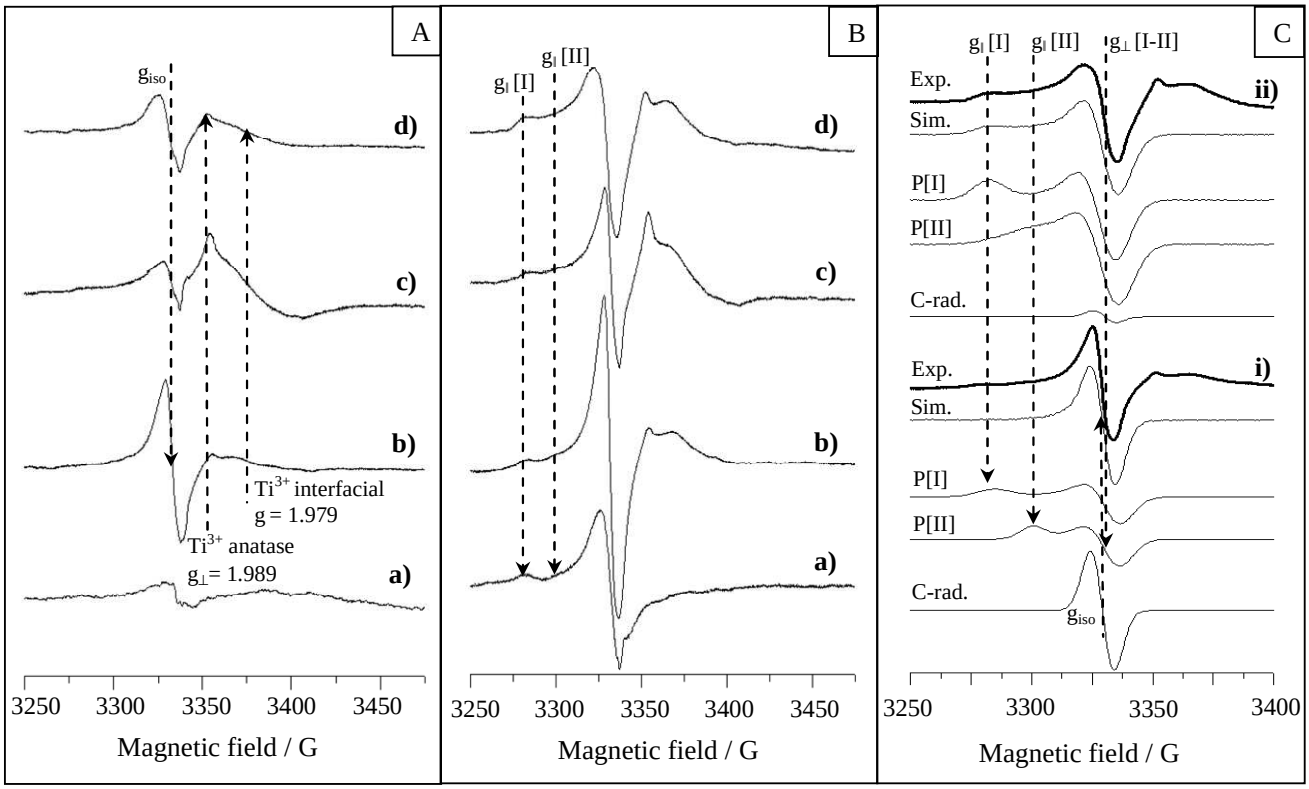

Figure 3.8. EPR spectra under vacuum (A) and in the presence of 7 mbar of O_2 (B) of TPM after 30' of the first photocatalytic run (line b), after completion of the first (line c) and the sixth run (line d). Membrane without P25, undergone the some treatments, is also reported for comparison (line a).

(C) Deconvolution of EPR signals of TPM after the completion of the first (i) and the sixth run (ii). Dashed lines are guide to detect the different paramagnetic species.

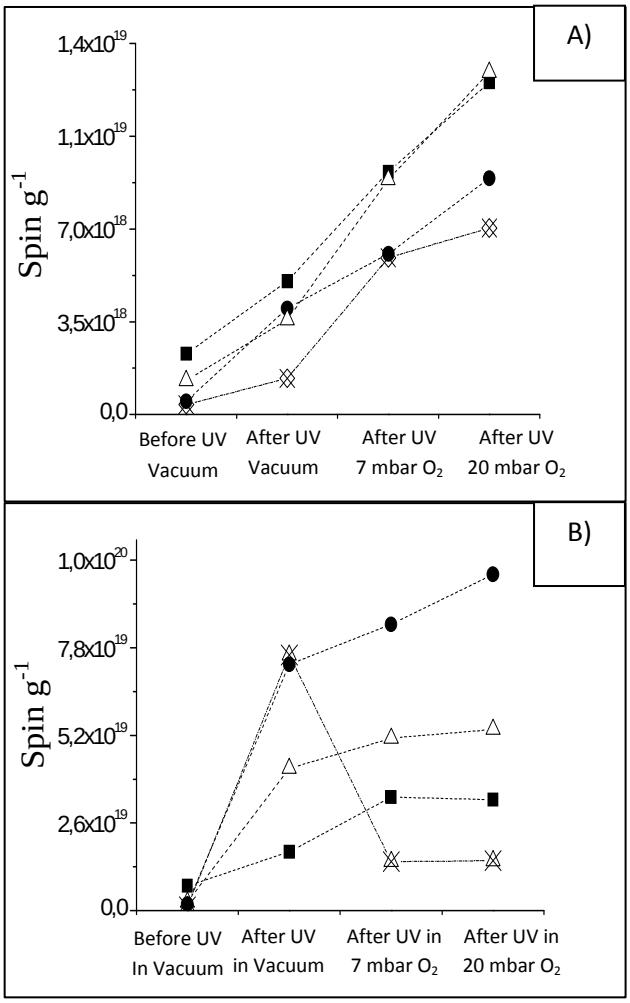

Figure 3.9. Trends of the relative amounts of membrane matrix radicals (A) and Ti^{3+} species (B) calculated for some selected samples: (□) membrane without P25; (■) TPM after 30' of the first run; (●) TPM after the completion of the first run; (∆); TPM after six runs; (○) P25

3.6 Conclusions

It is here reported a kinetic and mechanistic study of TiO_2 embedded in polyester acrylate membranes, produced by the photografting process and tested in the phenol photodegradation.

The photografting process of the mixture, containing the catalyst and the matrix precursors,allows to create a new material organic/inorganic combining the catalytic properties of the titania nanoparticles and the structural properties of the polymeric matrix to support the catalyst.

Despite the catalyst is nanometrically dimensioned during the embedding into the matrix the polarity of the particles surface induces their partial aggregation forming micrometrical agglomerates.

The overall results confirmed that the polymeric membrane does not significantly affect the peculiar photocatalytic properties of P25 and demonstrate that when TiO_2 is embedded into the membrane matrix, its photoactivity is enhanced with respect to that displayed after simple catalyst supporting.

This effect was attributed to the lower coarsening of titania nanocrystals into the TPM membrane which retains a surface area suitable both to UV irradiation and to the adsorption/degradation of PhOH.

In addition, the EPR investigation evidenced that since the membrane is in intimate contact with TiO_2, the photo produced holes generate C-centered radicals on the membrane, which in turn react with O_2 to form peroxy radicals. This process contributes to keeping the electrons located on Ti^{3+} centers separate from the holes fixed on the polymer, possibly enhancing the photocatalytic efficacy.

Thus, for the first time, it was reported that the embedding of TiO_2 into polymeric membrane not only helps in modulating the absorption of reactants and the catalyst

physical properties, or makes the separation process after reaction easy, but also provides unexpected effects on the stability of charge separation. Therefore it appears that, in the case of embedded TiO_2, the change of membrane composition aimed at varying the hole trapping ability of polymers, can be a future challenge to really improve the catalytic efficacy.

References

[1] Carp, O.; Huisman, C.L.; Reller, A.; Prog. *Solid State Chem*. 2004, 32, 33-177

[2] Chen, M.; Mao, S. S.; *Chem. Rev*. 2007, 107, 2891-2959

[3] Testino, A.; Bellobono, I.R.; Buscaglia, V.; Canevali, C.; D'Arienzo, M.; Polizzi, S.; Scotti, R.; Morazzoni, F.; *J. Am. Chem. Soc.* 2007, 129 3564-3575

[4] a) Scotti, R.; Bellobono, I.R.; Canevali, C.; Cannas, C.; Catti, M.; D'Arienzo, M.; Musinu, A.; Polizzi, S.; Sommariva, M.; Testino, A.; Morazzoni, F.; *Chem. Mater*. 2008, 20, 4051-4061. b) Bleta, R.; Alphonse, P.; Lorenzato, L.; *J. Phys. Chem*. C 2010, 114, 2039-2048

[5] a) Benfer, S.; Knozinger, E. *J. Mater. Chem.* 1999, 9, 1203-1209. b) H. Kikuchi, M. Kitano, M. Takeuchi, M. Matsuoka, M. Anpo and P.V. Kamat, *J. Phys. Chem. B* 2006, 110, 5537-5541. c) Kim, J.H.; Lee, S.; Im, H.S.; *Appl. Surf. Sci.* 1999, 151, 6-16

[6] Choi, J.; Park, H.; Hoffmann, M.R.; *J. Phys. Chem.* C 2010, 114, 783-792, and references therein.

[7] a) Di Valentin, C.; Finazzi, E.; Pacchioni, G.; Selloni, A.; Livraghi, S.; Paganini, M.C.; Giamello, E.; *Chem. Phys*. 2007, 339, 44-56. b) D'Arienzo, M; Scotti, R; Wahba, L.; Battocchio, C.; Bemporad, E.; Nale, A.; Morazzoni, F.; *Appl. Catal. B: Environ*. 2009, 93 149-155. c) Oropeza, F.E.; Harmer, J.; Egdell, R.G.; Palgrave, R.G.; P*hys.Chem.Chem. Phys*. 2010, 12, 960-969

[8] a) Hurum, D. C.; Agrios, A. G.; Gray, K. A.; Rajh, T.; Thurnauer, M. C. *J. Phys. Chem. B* 2003, 107, 4545–4549. b) Berger, T.; Sterrer, M.; Diwald, O.; Knozinger, E. *ChemPhysChem* 2005, 6, 2104–2112. c) Berger, T.; Sterrer, M.; Stankic, S.; Bernardi, J.; Diwald, O.; Knozinger, E. *Mater. Sci. Eng. C* 2005, 25, 664–668. d) Berger, T.; Sterrer, M.; Diwald, O.; Knozinger, E.; Panayotov, D.; Thompson, T. L.; Yates, J. T. *J. Phys. Chem. B* 2005, 109, 6061–6068

[9] a) Choi, H.; Sofranko, A.C.; Dionysiou, D.D.; *Adv. Funct. Mater.* 2006, 16, 1067-1074 and references therein. b) Mendez-Vivar, J.; Mendoza-Serna, R.; *Silicon Chemistry* 2006, 3, 59-64

[10] a) Vankelecom, I.F.J.; *Chem. Rev*. 2002, 102, 3779-3810. b) Dioos, B.M.L.; Vankelecom, I.F.J.; Jacobs, P.A.; *Adv. Synth. Catal*. 2006, 348, 1413-1446. c) Damodar, R.A:; You, S.J.; chou, H.H.; *J. Hazard. Materials* 2009, 172, 1321-1328

[11] a) I.R. Bellobono, E. Selli, Photochemical Production of Composite Materials and Membranes: Mechanistic Aspects and Applications, in: "*Current Trends in Polymer Photochemistry*" (N.S. Allen, M. Edge, I.R. Bellobono, E. Selli, eds.), Ellis Horwood, London, UK, 1995, pp. 102-129. b) I.R. Bellobono, Photosynthetic Membranes in Industrial Waste Minimization and Recovery of Valuable Products, in "*Membrane Technology: Application to Industrial Wastewater Treatment*" (A. Caetano, M.N. De Pinho, E. Drioli, H. Muntau, eds.), Kluwer Academic Publishers, Dordrecht, The Netherlands, 1995, pp. 17-24 c) I.R. Bellobono, E. Selli, Photografting Processes onto Polymers, in: *"Photopolymerisation and Photoimaging Science and Technology"* (N.S. Allen, ed.), Elsevier Applied Science, London (1989) pp. 115-148.

[12] a) Chen, D.W.; Ray, A.K.; *Appl. Catal. B: Environmental*, 1999, 23, 143-157. b) Ilisz, I.; Laszlo, Z.; Dombi, A.; *Appl. Catal. A: General*, 1999, 180, 25-45

[13] a) I.R. Bellobono, Italian Patents 1.189.074; 1.237.084; and 1.256.303. b) M.L. Stefanelli, to B.I.T. srl, Italian Patent 2004 A 000058 19/01/2004. c) M.L. Stefanelli, to B.I.T. srl, EP Appl. 05100298.8 19/01/2005. d) M.L. Stefanelli, to B.I.T. srl, Italian Patent Application (Pat. Attorney Dr. A. De Pasquale) 30/06/2008.

[14] Scotti, R.; D'Arienzo M.; Morazzoni, F.; Bellobono, I.R. Appl. Catal. B: Environmental, *Appl. Catal. B: Environmental*, 2009 *88,* 323-330

[15] Adamski, A.; Spalek, T.; Sojka, Z. *Res. Chem. Intermed.* 2003, *29*, 793-804

[16] a) Hurum, D. C.; Gray, K. A.; Rajh, T.; Thurnauer; *J. Phys. Chem. B* 2005, 109, 977-980. b) Anpo, M.; Shima, T.;, Fujii, T.; Suzuki, S.; Che, M.; Chemistry Letters 1987, 16, 1997-2000

[17] a) Hurum, D. C.; Agrios, A. G.; Crist, S. E.; Gray, K. A.; Rajh, T.; Thurnauer, M. C.; *J. Electron Spectrosc.* 2006, 107, 155–163. (b) Ke, S. C.; Wang, T. C.; Wong, M. S.; Gopal, N. O.; *J. Phys. Chem. B* 2006, 110, 11628–11634. (c) Kumar, C. P.; Gopal, N. O.; Wang, T. C.; Wong, M. S.; Ke, S. C.; *J. Phys. Chem. B* 2006, 110, 5223–5229.

[18] Scotti, R.; D'Arienzo M.; Testino, A.; Morazzoni, F. *Appl. Catal. B: Environmental*, 2009 *88,* 497-504

[19] a) Coronado, J. M.; Maira, A. J.; Conesa, C. J.; Yeung, K. L.; Augugliaro, V.; Soria, J.; *Langmuir* 2001, 17, 5368–5374. (b) Yeung, K. L.; Yau, S. T.; Maira, A. J.; Coronado, J. M.; Soria, J.; Yue, P. L. *J. Catal.* 2003, 17, 107–116. (c) Coronado, J. M.; Soria, J; *Catal. Today* 2007, 123, 37–41. (f) Attwood, A. L.; Murphy, D. M.;

Edwards, J. L.; Egerton, T. A.; Harrison, R. W.; *Res. Chem. Intermed.* 2003, 29, 449– 465. (g) Carter, E.; Carley, A. F.; Murphy, D. M.; *J. Phys. Chem. C* 2007, 111, 10630–10638.

[20] a) Carter, M.; Carley, A.F.; Murphy, D.M. *ChemPhysChem* 2007, *8*, 113-123. b) Attwood, A.L.; Edwards, J.L.; Rowlands, C.C.; Murphy, D.M.; *J. Phys. Chem.* A 2003, 107, 1779-1782

CHAPTER 4

TiO_2-SiO_2 Nanocomposite for Photocatalysis

4. Introduction

In the last few years nanocrystalline TiO_2 has been extensively studied as the photocatalyst in the oxidative degradation of organic and inorganic pollutants[1]. The interaction of this oxide with UV radiation generates electron-hole pairs which are able to activate surface reactive processes [2]. The recombination rate of charges, which affects catalyst photoactivity, strongly depends on the morphological and structural properties of the oxide, such as the different crystalline phase, surface area, particle shape and porosity [3]. Consequently, the control of the photocatalytic activity of TiO_2 nanoparticles throughout the tailoring of their morphological and structural properties is a current topic of great interest.

The photodegradation of toxic compounds is usually performed by using titania nanoparticles in aqueous suspension (slurry). However, the use of nanosized powders as slurries in wastewater treatment causes difficult post-use recovery and requires expensive and time-consuming separation/recycling processes [4]. In addition, TiO_2 nanoparticles, when dispersed in the surrounding environment, may be hazardous, due to their potential inflammatory and cytotoxic effects [5]. These drawbacks can be avoided by immobilizing or embedding the TiO_2 nanoparticles on a support. Many inorganic or polymeric materials have been employed for this purpose: : silica glass shaped as beads [6], rings [7], reactor walls [8] and fibers [9]; quartz [10]; zeolites [11]; perlite [12]; pumice [13]; alumina-based ceramics [14]; stainless steel [15]; aluminium [16]; cotton fibers [17]; polyester, acrylate [18], fluorinate [19] polymers. Nevertheless, both immobilization and embedding frequently lower the catalyst exposed area compared to that of the powder suspension [20].

Polymeric substrates show poor resistance to thermal treatments and undesired sensitivity to photooxidative processes, compared to inorganic ones [20b]. Inorganic membranes, consisting of macroporous ceramic substrates covered by micro/mesoporous active TiO_2

layers, seem promising alternatives for several large scale catalytic processes [21]. In fact, the porous skeleton of the ceramic framework provides chemical and thermal stability, mechanical durability, low pressure drops and rapid mass transport of fluids, due to the extensive interconnection between the macropores. This structure guarantees high accessibility to the catalyst active sites and fast uptake/release cycles. In addition, the mesoporosity of the titania layer preserves the permeability of the ceramic matrix and provides an effective contact between the target molecules and the catalyst particles [22].

Different approaches, based on soft-chemistry routes, hydrothermal synthesis, and chemical (CVD)/physical (PVD) vapour deposition, were proposed in order to obtain oxide coatings on preformed macroporous ceramic matrices [23]. The ideal active layers should be homogeneous, chemically and thermally stable, loading large amounts of material crucial for the catalytic activity and without pore occlusion which limits the whole permeability.

In this context, we propose a novel sol-gel synthetic strategy, employing hybrid organic-inorganic reactants for the preparation of a macroporous silica matrix and the simultaneous surface grafting of preformed TiO_2 nanocrystals. The goal is to design a TiO_2-SiO_2 (TS) composite material with the following characteristics:

- high macroporosity and UV-transparency of the silica matrix, which guarantees easy mass transport towards the catalyst surface sites and allows effective interaction of TiO_2 with UV radiation;

- TiO_2 nanocrystals grafted on the surface of the ceramic matrix, whose well defined morphological and structural properties determine high photoactivity;

- minimum loss of photoactivity due to catalyst immobilization, in comparison to the slurry TiO_2;

- improved thermal stability and durability without leaching of the grafted catalyst.

The macroporous silica network was produced by the sol-gel process based on hydrolysis and condensation of tetramethylorthosilicate (TMOS) in the presence of polyethylenglycol (PEG) as the sacrificial template [24]. Due the TMOS sol-gel transition, phase separation occurs between the silica gel network and the polymer. Starting from a uniform solution containing the polymer and the TMOS, the species are molecularly mixed and the hydrogen bonds between the PEG and the hydroxyl-silanes generate *class I* hybrid material. Proceeding the silanes hydrolysis-condensation the silica network formation induces the separation of the PEG chains in warm-like shape structures. The PEG also acts as a carrier of TiO_2 particles into that will form macropores of silica matrix (see scheme 4.1). In order to disperse TiO_2 in the PEG phase, the oxide particles were functionalized with carboxylic acid or amine derivatives [25], which make the TiO_2 surface less hydrophilic, improving the interactions with the polymeric chains. Subsequent annealing at 500°C removes both PEG and functionalizing organic molecules and generates the interconnected macroporous silica network. Thus, the TiO_2 crystals, previously being dispersed in the PEG phase, graft onto the silica surface channels, preserving their crystal phase and size.

TS composites were prepared by using anatase and commercial P25 nanoparticles with known morphological and structural characteristics and high photoactivity [3a,3b,26]**,** which were functionalized by carboxylic acid and amine derivatives having different side chains (propionic acid, exylamine and 2-methoxyethylamine). The influence of the functionalizing agent on the dispersion of TiO_2 nanoparticles in PEG and, consequently, on their final exposure and dispersion on silica macropore walls was demonstrated.

Photocatalytic activity of TS samples was tested in the degradation reaction of PhOH in aqueous solution and compared to the same anatase in slurry. It turned out that the

immobilization procedure uncommonly preserves the catalytic properties of the TiO_2 nanocrystals.

The proposed new synthetic strategy may be potentially applied both to graft different functional oxides to ceramic macroporous substrates, keeping high functional properties eventually modulating the porous architecture of the silica matrix by changing the sol-gel synthesis parameters.

4.1 Preparation

All chemicals and solvents were purchased from Sigma-Aldrich as analytical grade and used as received without further purification. Deionised water (18 MΩ cm) was used for the procedures that required water.

4.1.1 TiO_2 Functionalisation with Organic Molecules

Nanocrystalline TiO_2 anatase and P25 was obtained by hydrothermal synthesis, according to the previously reported procedure [26], by reacting aqueous solutions of $TiOCl_2$ (Aldrich, 99 %) and NH_3 (Fluka, > 25 wt %) in a teflon lined autoclave (Parr, model 4768Q). The autoclave was heated at a rate of 2.67 °C/min just to 30 °C below the set-point temperature, then at a rate of 0.75 °C/min up to 220°C. TiO_2 surface was functionalized following a modified literature procedure [27]. In anhydrous conditions, 20 mL of the organic reagent (propionic acid, PA; exylamine, EA; 2-methoxyethylamine, MA) was added to 3.30 g of TiO_2 suspended, after ultrasound treatment, in 40 mL of anhydrous methanol. The amount of the organic reagents was in large excess compared to the oxide. The obtained suspensions were refluxed for 8 hours and kept overnight under stirring at room

temperature (RT). Finally, the suspensions were divided into 6 aliquots and the particles were separated by centrifugation at 6000 RPM for 30 min and recovered by decantation. In order to remove the unreacted chemicals and the residual traces of methanol, each aliquot was washed for 30 min under ultrasound conditions by ethyl acetate (2 times with 10 mL) and CH_2Cl_2 (2 times with 10 mL), respectively. After each washing treatment, the surnatant was separated by centrifugation and decantation. The final wet powders were dried in air at RT overnight, and the residual solvent evaporated 24 hours in vacuum (10^{-2} torr). The capped NPs are labelled TiO_2-PA, TiO_2-EA and TiO_2-MA when functionalised with propionic acid, exylamine and methoxyexylamine respectively.

4.1.2 Synthesis of the Hybrid Material and Nanocomposite TiO_2-SiO_2 (TS)

TS was prepared by using TiO_2-PA, TiO_2-EA and TiO_2-MA. The whole synthesis procedure of TS is shown in Scheme 4.1.

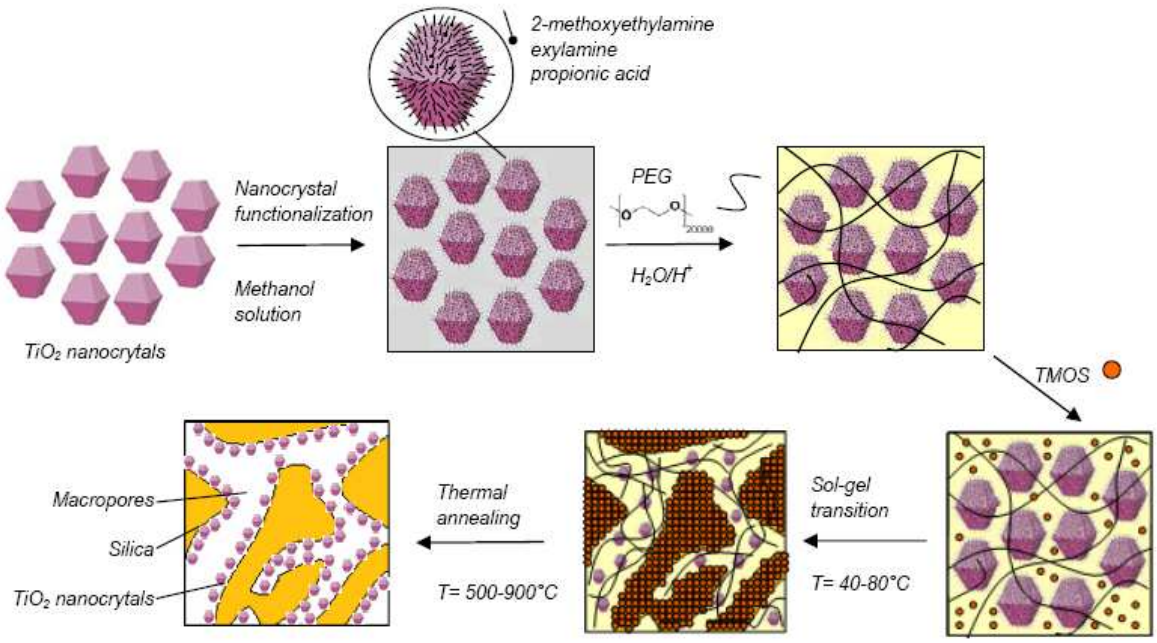

Scheme 4.1. Overall synthesis process.

Specifically 0.723 g of polyethylene glycol (PEG 20000) were dissolved in a water solution of acetic acid (6.90 mL, 0.10 M) under magnetic stirring. After the completed dissolution of the polymer, 150 mg of TiO_2-PA, TiO_2-EA, and, corresponding to a nominal content of the 10.7 % w/w on the final TS material, were added and uniformly dispersed under ultrasound (2-3 minutes) treatment. Then, 3.10 ml (3.17 g) of TMOS were added to the PEG/TiO_2 mixture and stirred for 5 minutes at RT. Sol-gel transition was induced by storing the samples in closed vessels at 40 °C for 24 hours and, subsequently, at 80 °C for 24 hours than removed the surnatant and rinsed the obtained gel with water (3 times with 20 ml). The gel was aged and dried heating in open vessel at 100 °C for 24 hours. TS material was successively oven dried at 150 °C for 1 hour and calcined in air at 500 °C for 5 hours. The final calcination was also performed at 600 °C, 700 °C, 800 °C and 900 °C in order to study the effect of the annealing temperature on the material structure and morphology (e.g. porosity, surface area, titania crystal phase and size) and on the photoactivity. TS was also prepared by using pristine anatase, according to the same described procedure. TS samples from TiO_2-PA, TiO_2-EA and TiO_2-MA and from pristine TiO_2 are labelled TS-PA, TS-EA, TS-MA and TS-UC, respectively.

4.2 Morphological and Chemical Characterization

X-ray diffraction (XRD) patterns of the powders were collected with a Brucker D8 Advance (Cu K_α radiation) in the range 20-80° 2θ (2θ step 0.025°, count time of 2 s per step). TiO_2 nanoparticles functionalized with organic molecules were characterized by ATR-FTIR and Solid-state NMR. ATR-FTIR analysis was performed by a Perkin Elmer Spectrum 100

instrument (1cm^{-1} resolution spectra, 650-4000 cm^{-1} region, 16 scans). Quantitative determination of the amount of organic molecules which functionalizes the oxide, was performed by Thermo Gravimetric Analysis (TGA) and Differential Scanning Calorimetry (DSC) measurements performed with a Mettler Toledo TGA/DSC1 STAR^e System, at constant gas flow (50 cm^3 min^{-1}). Thermal profile was the following: 40 °C 5 min (under N_2); 40-150 °C 10 °C min^{-1} (under N_2); 150 °C 5 min (under N_2); 150-1000 °C 10 °C min^{-1} (under air).

Scanning electron microscopy (SEM) measurements were performed by a LEO 1450VP instrument. Transmission electron microscopy (TEM), High-resolution transmission electron microscopy (HRTEM) and electron diffraction (ED) measurements were performed using a Jeol 3010 apparatus operated at 300 kV with a high-resolution pole piece (0.17 nm point to point resolution) and equipped with a Gatan slow-scan 794 CCD camera. The powders were suspended in isopropanol, and a 5 μL drop of this suspension was deposited on a holey carbon film supported on 3 mm copper grid for TEM investigation.

4.2.1 Solid State NMR

Nuclear Magnetic Resonance (NMR) is a widely used technique used to identify the nuclei interactions in molecules, polymer and even solids. The NMR technique exploit the nuclei spins when introduced into a magnetic field. The resonance frequencies of the different nuclei depend by the chemical surrounding e.g. the chemical bonds. The correlation between the detected radio frequencies and the chemical bonds allows to identify the atoms connections. These nuclei interactions depend on the direction: for liquid

experiments the brownian motion provides the averaging of the signal while for solid state NMR sample magic angle spinning is used for the averaging of the signal.

Solid-state NMR analyses were carried out with a Bruker Avance 400WB NMR spectrometer operating at a carrier frequency of 400.13 MHz for ^{1}H. ^{13}C NMR spectra were acquired with cross-polarization and under the following conditions: ^{13}C frequency, 100.06 MHz; π/2 pulse length, 2.8μs; ^{1}H decoupling pulse power, 47 kHz; recycle delay, 5 s; contact time during CP, 2 ms; number of scans, 14000. Samples were packed in 4 mm zirconia rotors, which were spun at 8 kHz under air flow. Adamantane was used as secondary reference.

4.2.2 Mercury and Nitrogen Porosimetry

Porosimetry is a technique used to determine different quantifiable morphological properties of a porous material: pore diameter, surface area, total pore volume and consequently bulk and absolute densities. The technique is based on the intrusion of a no wetting fluid (generally mercury for macropores and nitrogen for meso/micropores) under pressure. The correlation between pressure and volume of the intruded fluids is used to determine the porous properties of the material.

The size distribution of macropores (> 50 nm) was measured by mercury porosimetry with a Pascal 140/240 Thermo Fisher instrument, assuming 140° as contact angle between mercury and sample. The pressure range varied between 15.8 kPa and 200 MPa

Specific surface area (SSA) by BET method [28], desorption cumulative pore volume (DCPV) and pore size distribution of micro- and mesopores (< 50 nm) by BJH method [29] were measured by nitrogen physisorption using Quantachrome Autosorb-1 apparatus. Powder samples were evacuated at 200 °C for 16 h before the analysis.

4.3 Photochemical Activity: Phenol Degradation in Water

Photodegradation experiments were carried out in a specifically designed discontinuous batch photoreactor described in detail in chapter 3 [30]. The reactor (600 mL), provided with an external cooling jacket, was equipped with a UV 125 W high pressure Hg arc lamp and placed in a coaxial quartz cylinder without optical filter. Photocatalytic tests were performed in aqueous solution by using O_2 as oxygen donor and operating either with TS materials or with pure TiO_2 powder slurries as catalysts. Approximately 1.20 g of TS (TiO_2 loading 0.128 g, corresponding to 0.21 g L^{-1}) were grossly moulded and dispersed in 600 mL of phenol (PhOH) aqueous solution (121 ± 2 mg L^{-1} of PhOH, 93 ± 2 mg L^{-1} as C). The obtained mixture was recirculated by a peristaltic pump with a speed of 14 mL s^{-1}. TS samples were moulded to have the same hydrodynamic conditions of the pure titania used as slurry in photocatalytic experiments.

In the case of pure titania slurry, TiO_2 powder (160 ± 5 mg; 0.25 g L^{-1}) was suspended by sonication in 600 mL of water containing the same concentration of PhOH and recirculated at the same conditions as in the experiments with TS. The reaction was performed at 25 ± 2 °C, by keeping the oxygen feed constant and by eliminating the excess of gas through a non return check valve. The dissolved oxygen content was monitored by an online sensor. The slurry was circulated in the dark and saturated in an online chamber by continuously bubbling oxygen (100 mL min^{-1}). The oxygen content became maximum and constant in about 10 min. The UV source was turned on after 1 h of recirculation in the dark. The PhOH adsorption on the catalyst was checked by withdrawing suspension aliquots (6 mL) of the solution at regular intervals and analyzing the TOC by a Shimadzu TOC-V CSH analyzer. Powders were separated by centrifugation before TOC analysis. The same procedure was applied to monitor the kinetics until the complete mineralization of the

substrate. Finally, reference experiments (Blank) were carried out in the absence of TiO_2 and TS.

4.4 Photochemical Activity: NO_x Degradation in Air

4.4.1 Problem and current technology brief overview[31]

Every combustion reaction such as fuel in an engine or waste into an incinerator produces NO_x because the nitrogen contained in the air reacts with oxygen at high temperature. In industrial context the NO_x reduction is currently done by Selective Catalytic Reduction (SCR) in DENOX plant. SCR technology is based on the reduction of nitrogen oxide converting it in molecular nitrogen and water:

$$4\ NO + 4\ NH_3 + O_2 \rightarrow 4\ N_2 + 6\ H_2O$$

The exhausted gas containing the nitrogen oxides are then reduced by ammonia using V_2O_5 and WO_3 supported on a TiO_2 ceramic matrix at temperature between 265–425 °C. The reaction efficiency is generally around the 80%. The reaction temperature has to be strictly controlled because lower temperature reduce the SCR efficiency while higher temperatures cause the oxidation of ammonia nitrogen into NO_x as well. The technological problems for the realization of an efficient DENOX plant are mainly due to need of temperature control of continuous providing of ammonia and the the intrinsic under-stoichiometric content of the ammonia. In fact because of the ammonia toxicity the reaction has to convert all the ammonia into molecular nitrogen avoiding release of it into the atmosphere. With these preliminary remarks it is easy to imagine the complexity of a DENOX plant as well its cost.

Instead and more conveniently NO_x can be oxidized transforming them into harmless nitrate species. The NO_x oxidation can be conducted using photocatalytic reactions involving TiO_2 as catalyst as it follows[32]:

$$OH^- + h^+ \rightarrow OH^\cdot$$

$$NO + 2\ OH^\cdot \rightarrow NO_2 + H_2O$$

$$NO_2 + OH^\cdot \rightarrow NO_3^- + H^+$$

$$O_2 + e^- \rightarrow O_2^-$$

$$NO + O_2^- \rightarrow NO_3^-$$

Holes and electrons are photoinduced in TiO_2. By reacting with water and oxygen they oxidize nitrogen oxides. Compared to the SRC technology no harmful reactant is provided but just water and oxygen and no temperature control is needed. The drawback of this technology is the fixation of the nitrates on the TiO_2 surface. In fact the catalyst surface is covered by the reaction products and it is unable to continue the oxidation. The catalyst surface has to be regenerated removing the nitrates which can be removed by washing the catalyst. In the present work different washing media are tested. Moreover in order to study the best reaction conditions for NO_x oxidation the influence of the lamp power is study. It is well known that under UV illumination the NO can be oxidized to NO_2. The photocatalyst efficiency for NO_x oxidation has to be measured avoiding the eventual influence of the UV lamp power. Thus we used lamps with two different power consumption: 125W and 6W. In view of an industrial application, NO_x concentration of the inner gas can be varied in a large range, thus we studied also the influence of this parameter versus the catalyst efficiency. Some other applications involving TiO_2 were

investigated in literature in the past decades. The most studied was the realization of TiO_2 embedded in cement to coat external walls or pavement[33].

4.4.2 The material and the test reactor

The TS material obtained as cylindrical pellets with 0.5-0.8 cm base diameter and 0.5-0.8 cm height are introduced in a cylindrical quartz coaxial reactor (Figure 4.1) provided with a UV lamp. The pellets layer surrounding the lamp is approximately 1 cm thick and 8 cm height. The NO_x concentration is controlled by two mass flows connected with synthetic dry air and 80 ppm NO_x in nitrogen cylinders. The gas mixture is humidified bubbling it into deionized water; then it passes through the photoactive material and is analyzed by chemiluminescence NO_x analyzer (SARTEC, model 200E).

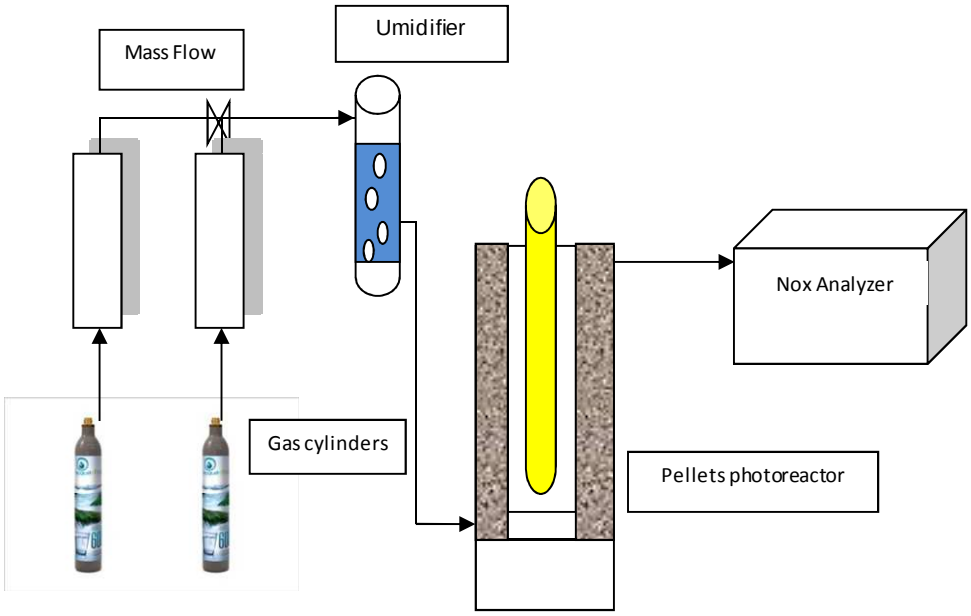

Figure 4.1. NO_x photoreactor scheme. The gas cylinders content is synthetic dry air and 80 ppm of NOx in nitrogen. The UV lamp is sketched as a yellow cylinder inserted in a quartz coaxial reactor, the photocatalytic pellets surround the lamp.

We tested to types of materials in the NO_x measurements. One material was the same TS material used for phenol degradation tests prepared in pellets shape. The other one (TS-P25) was a material prepared by the same procedure as to prepare the TS one but, implying commercial TiO_2 (Degussa P25). The purpose to use commercial TiO_2 was to demonstrate the generality of the procedure. We want to demonstrate that the matrix characteristics are independent from the catalyst nature but depend only on the titania surface functionalisation and the reaction conditions.

4.5 Discussion and Results

4.5.1 Characterization of pristine and functionalized TiO_2 nanoparticles

The XRD pattern of pristine anatase TiO_2 nanoparticles is reported in (Fig.4.2). The average crystallite size, estimated from the peak of (101) reflection using the Scherrer's equation, resulted 10.5 nm.

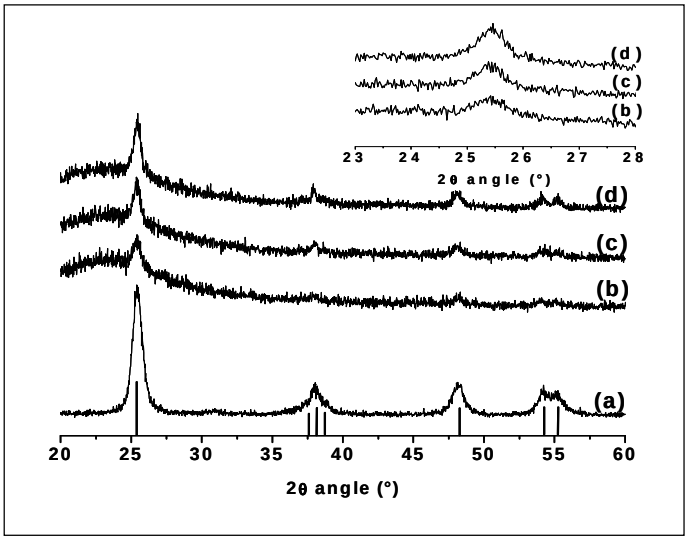

Figure 4.2. XRD powder pattern of (a) anatase powder and TS-MA calcined at (b) 500, (c) 700 and (d) 900°C. (d). Inset: magnification of (101) peak. The vertical lines indicate position and intensities of anatase reflections.

The XRD patterns of TiO_2-PA, TiO_2-EA, TiO_2-MA, TiO_2 functionalized with propionic acid, exylamine and 2-methoxyethylamine respectively, revealed the same size and phase of the pristine TiO_2 nanoparticles.

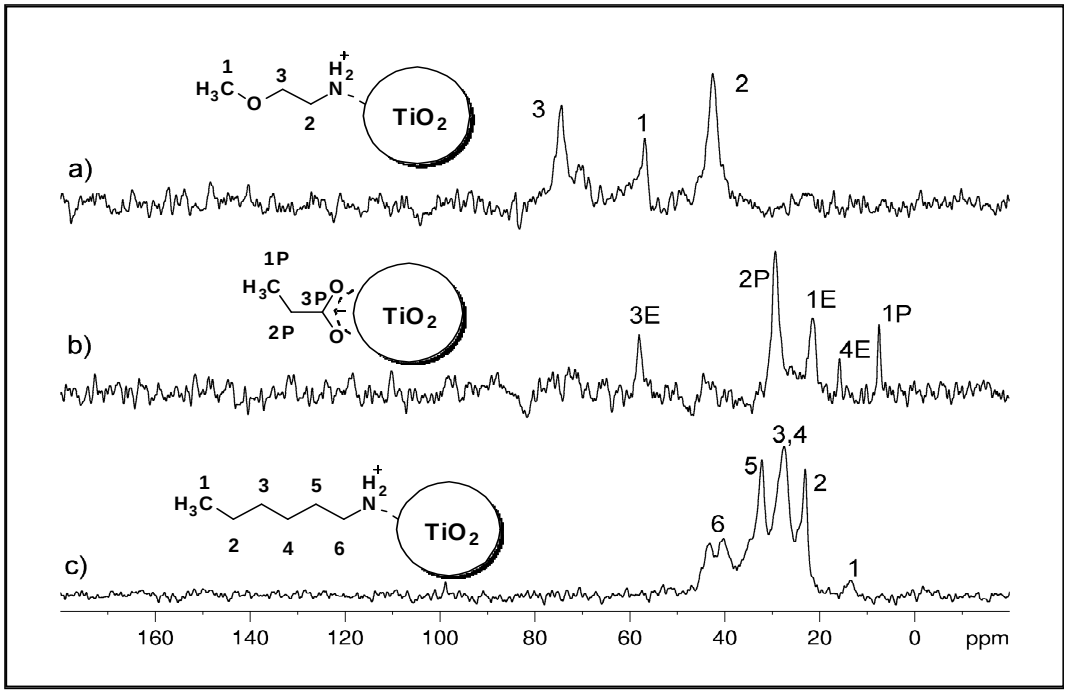

Figure 4.3. ^{13}C CPMAS NMR spectra of a) TiO_2-MA b) TiO_2-PA with residues of ethyl acetate and c) TiO_2-EA. Molecular structures and peak assignment, as reported in Table 1, are shown.

TiO_2-PA, TiO_2-EA, TiO_2-MA nanoparticles were characterized by means of solid-state ^{13}C NMR and ATR-FTIR. The obtained NMR spectra assessed the effective functionalization of the anatase surface (Fig. 4.3). The detected ^{13}C signal peaks were assigned according to the literature [34] values and are summarized in Table 4.1.

Table 4.1. . ^{13}C chemical shifts and signal assignments (The reference values are from liquid NMR studies of the pure species) [34]

Unit	TiO_2-PA	Ref.	Unit	TiO_2-EA	Ref.	Unit	TiO_2-MA	Ref.
1 [P]	7.5	8.9	1 [H]	13.5	14.1	2 [M]	42.6	41.8
4 [E]	15.8	14.3	2 [H]	23.1	22.8	1 [M]	57.0	58.7
1 [E]	21.7	21.0	3 [H]	27.5	26.7	3 [M]	74.4	74.9
2 [P]	29.4	27.6	4 [H]	28.7	31.9			
3 [E]	58.1	60.4	5 [H]	32.2	34.1			
3 [P]	[nd]	181.5	6 [H]	40.2;43.2	42.4			
2 [E]	[nd]	171.1						

[P] Propionic acid. [E] Ethyl acetate. [H] n-hexylamine. [M] 2-metoxyethylamine. [nd] Not detected

The ^{13}C NMR spectra of TiO_2-EA and TiO_2-MA exhibit the signals due to hexylamine and 2-methoxyethylamine, respectively (Table 4.1). In particular, the two different signals in the TiO_2-EA spectrum attributed to carbon C-6, are explained by the γ-gauche effect [35]. The hexylamine chains can exist in two stable conformations, i.e. *trans* and *gauche* states of the C-4 - C-5 bond, which cause different electronic shielding at carbon C-6. Accordingly, the gauche conformation induces an upfield shift of the ^{13}C resonance compared to the trans one. It is assumed that the attachment of the chains to the anatase surface freezes the two conformational states on the NMR timescale, and the different conformations give rise to two different resonances of carbon C-6.

This behaviour is not detected in the TiO_2-MA sample, where the MA chain is too short to exhibit such a conformational effect.

The ^{13}C NMR spectrum of TiO_2-PA shows the signals of methyl and methylene groups of PA (Table 4.1). The lack of C=O peaks can be ascribed to the poor signal-to-noise ratio and to the large chemical shift anisotropy, which causes spinning sidebands and a distribution of the overall intensity over several signals resonances. Moreover, for carbonyl groups the signal enhancement due to ^{13}C-^{1}H cross-polarization is rather limited due to the lack of directly bonded protons. In TiO_2-PA spectrum, the observed ethyl acetate signals are due to traces of residual washing solvent.

FTIR spectra of TiO_2-PA, TiO_2-EA, TiO_2-MA, compared to those of PA, EA and MA and of pristine anatase, are shown in Fig.4.4.

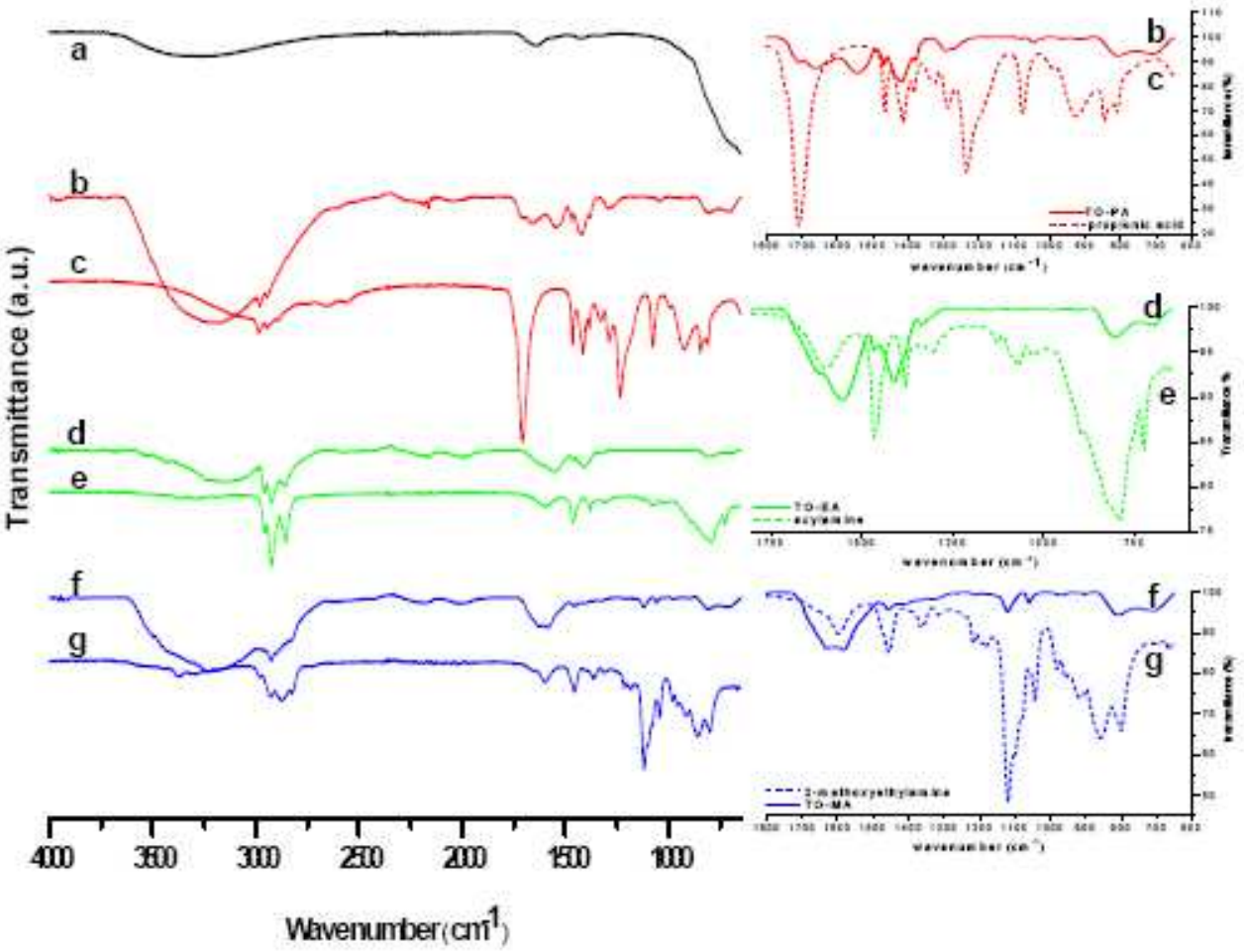

Figure 4.4. . FTIR spectra of (a) bare nanoparticles, (b) TO-PA, (c) propionic acid, (d) TO-EA, (e) n-exylamine, (f) TO-MA and (g) 2-methoxyethilamine. Inset, the same spectra enlargement in the range 1800-600 cm^{-1}.

The spectra confirm the grafting of the organic molecules on titania nanoparticles in agreement with the ^{13}C CPMAS NMR results. In TiO_2-PA, the PA grafting is demonstrated by the presence of the carboxylate stretching modes and the disappearing of the carbonyl stretching one. In TiO_2-MA and TiO_2-EA, the EA and MA surface interactions are evidenced by the bands assigned to the amino groups linked to the acid surface sites of the oxide.

The typical bands of the carboxylic group in PA, C=O stretching at 1705 cm^{-1}, C-O-H in plane deformation at 1415 cm^{-1} and C-O stretching at 1240 cm^{-1} (Figure 4.4c), disappear in TiO_2-PA (Figure 4.4b), where the bands of carboxylate group, C-O asym. and symm. stretchings at 1545 cm^{-1} and 1420 cm^{-1}, are evident, indicating the formation of the chemical bond between the carboxylic group and the surface Brönsted acid sites[36]. The characteristic bands of amines in EA (N-H asymmetric and symmetric stretchings at 3370 cm^{-1} and 3285 cm^{-1}; $N-H_2$ scissoring at 1600 cm^{-1}; C-N stretching at 1070 cm^{-1}; N-H wagging at 795 cm^{-1}) and MA (N-H asymmetric and symmetric stretching at 3370 cm^{-1} and 3293 cm^{-1}; $N-H_2$ scissoring at 1598 cm^{-1}; C-N stretching at 1120 cm^{-1}; N-H wagging at ~ 850 cm^{-1}) are also present in TiO_2-EA and TiO_2-MA (inset Figure 4.4), In particular, the bands involving the amino group are broadened and shifted compared to the corresponding bands of MA and EA. Such effects are related to the link between the amino group and the acidic sites of the oxide surface[37]. Besides, the permanent presence in all IR spectra of the typical alkyl groups bands of CH stretching in the region between ≈3000-2750 cm^{-1}, and of CH_2 scissoring at 1460 cm^{-1} due to the side chains of PA, EA and MA in spite of the repeated washing cycles, supports the formation of a chemical bond between the functionalizing molecules and TiO_2 nanoparticles in all the examined samples.

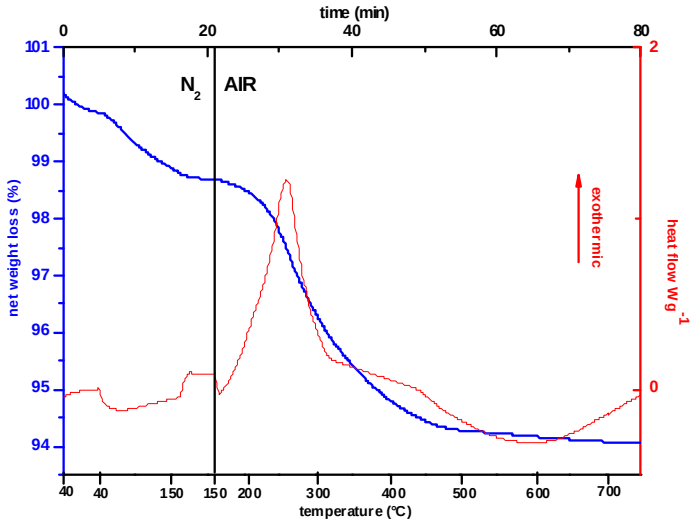

Fig. 4.5. TGA and DSC curves of TiO_2 anatase crystals capped with 2-methoxyethylammine

Table 4.2. Surface density of functional molecules on titania nanoparticles

Functionalizing agent	MW [g mol^{-1}]	Net loss [weight %]	Σ [molecules nm^{-2}]	D [nm]
Propionic Acid	74.1	1.18	0.60	1.46
Exylamine	101.2	3.31	1.25	1.01
2-Methoxyethylamine	75.1	1.72	0.86	1.22

The number of functionalizing molecules linked to the anatase nanocrystals (Table 4.2) was evaluated by thermogravimetric weight loss in the interval 150°C < T < 600°C (Fig. 4.5), due to the combustion of the organic species. The amount of the functionalizing molecules, expressed as weight %, was calculated by the net weight loss of surface functionalised TiO_2, i.e. the total weight loss, excluding that of bare TiO_2. The density of surface molecules Σ [molecules nm^{-2}] was calculated by using the BET Specific Surface Area value of bare anatase (162 m^2 g^{-1}). Finally, the distance between the functionalizing

molecules $D = (4/\pi\Sigma)^{1/2}$ [nm] was estimated. The results show that both surface density and distance of the linked molecules are in agreement with the literature data of similar systems [38].

The ability of functionalized particles to be dispersed in organic matrices was tested by simply mixing pristine TiO_2, TiO_2-PA, TiO_2-EA and TiO_2-MA with water and diethyl ether. The mixture water/diethyl ether was chosen to simulate the conditions of the sol-phase, assimilating the water to the aqueous solution of TMOS and the diethyl ether to the PEG phase. Fig. 4.6 shows the better dispersion of TiO_2-MA particles (d) in the ether phase compared to TiO_2-EA (c) which tends to segregate in the organic phase while TiO_2-PA (b) and bare TiO_2 (a) form homogeneous dispersions in the aqueous phase. This behaviour suggests that the short chain of PA is not able to confer enough hydrophobicity to TiO_2 nanoparticles to be dispersed into organic solvent, unlike TiO_2-EA and TiO_2-MA which have longer chains. In addition, TiO_2-MA nanoparticles are better dispersed in diethyl ether than TiO_2-EA, due to the presence of ether group, which makes them more similar to the solvent as for the polar character.

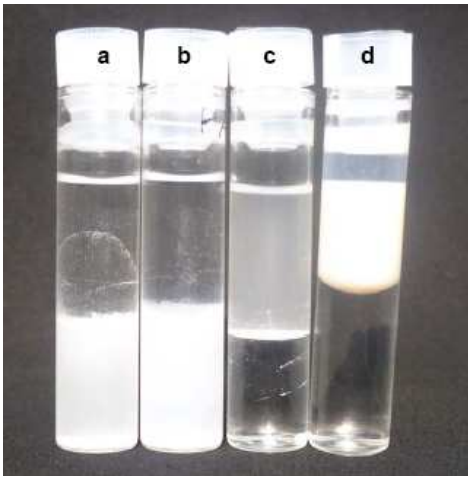

Figure 4.6. Test tubes containing ≈ 10 mg of (a) bare titania; (b) TiO_2-PA; (c) TiO_2-EA and (d) TiO_2-MA in water/diethyl ether mixture.

4.5.2 Morphological and structural characterization of TiO_2-SiO_2 samples

Macroporosity of TS-MA, TS-PA, TS-EA and TS-UC materials, calcinated at 500 °C were measured by Hg porosimetry. The dimension and the size distribution of the macropores are similar for all samples and not depending on the functionalizing molecules. 60% of the macropores have an average pore radius in the range 0.82 - 1.21 μm, while the total porosity is about 75 ± 5% of the total volume. TS-MA macropore distribution is shown as example in Fig. 4.7.

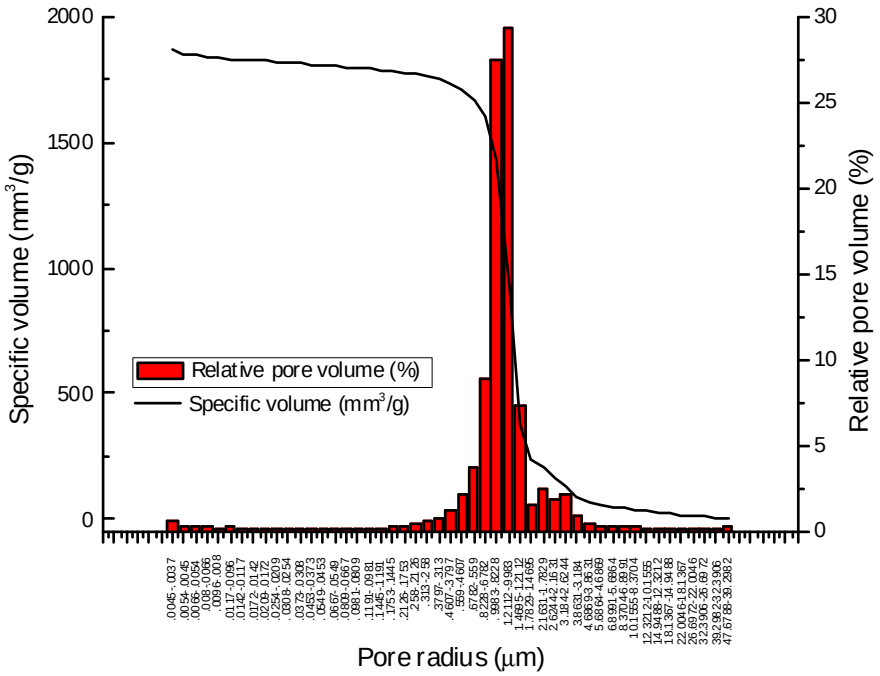

Figure 4.7. Hg-porosimetry of TS-MA calcined at 500°C

SEM analysis shows that the average size of silica particle in the matrix in all TS samples is about 2.5 μm and confirms the interconnected macroporous structure whose dimensions are in agreement with the porosity measurements (Fig. 4.8a, sample TS-MA reported).

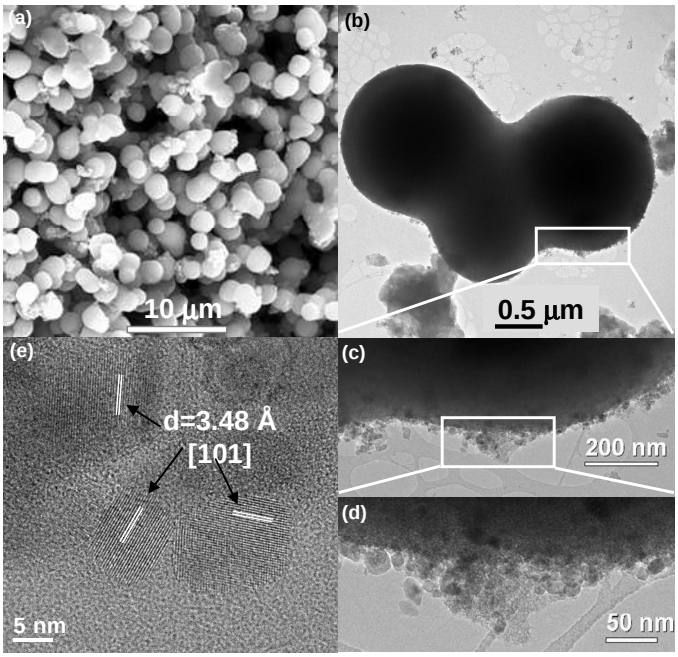

Figure 4.8. (a) SEM, (b, c, d) TEM and (e) HRTEM images at different magnifications of TS-MA after calcination at 500°C.

TEM and HRTEM micrographs demonstrate that TiO_2 nanocrystals are grafted on the surface of silica channels, the exposure and dispersion of the TiO_2 crystallites on silica depending on the side chain of the functional molecules and on their affinity with the PEG. The best result in terms of TiO_2 distribution was obtained for TS-MA, where TiO_2 crystals maintain the size of pristine anatase and interact with the ceramic surface without forming large aggregates (Fig. 4.8b-d). Comparison of the different samples (Fig. 4.9) reveals a relevant influence of the functionalizing molecules used on the TiO_2 crystallite dispersion.

In the absence of functionalizing molecules (TS-UC), TiO_2 particles are almost totally embedded in the silica matrix (Fig. 4.9a). In TS-PA, TiO_2 particles are only partially located on the silica surface (Fig. 4.9b), while in TS-EA, TiO_2 crystallites form large superficial aggregates (Fig. 4.9c) instead absent in TS-MA (Fig. 4.9d), as shown in Fig. 4.9d or more clearly in Fig. 4.8c, 4.8d.

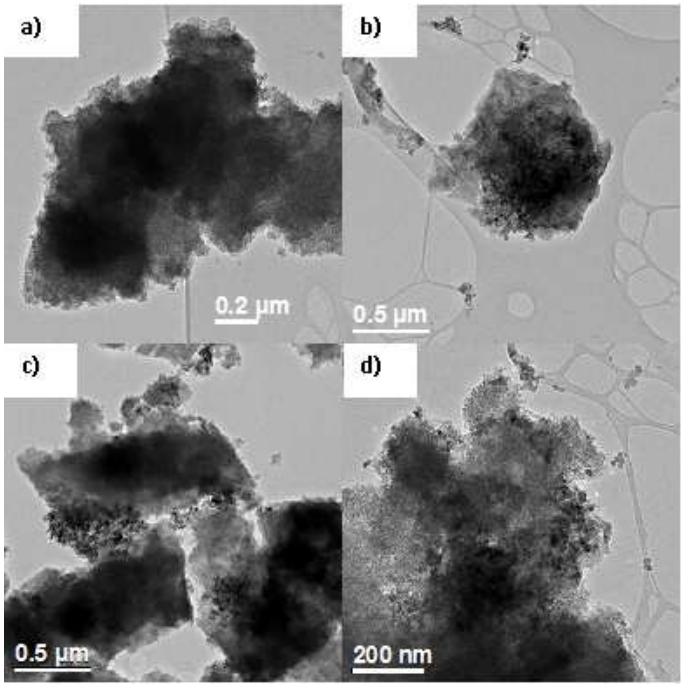

Figure 4.9. TEM image of different TS materials calcinated at 500 °C: (a) TS-UC, (b) TS-PA; (c) TS-EA; (d) TS-MA.

The different morphology of the materials may be related to the different chains of the functionalizing molecules and to their affinity with PEG. In particular, differently from the case of exylamine and 2-methoxyethylamine, the surface modification induced by the short side chains of propionic acid prevents a suitable dispersion of TiO_2 nanoparticles into the organic PEG phase during the sol formation. Consequently, PEG is not able to drive TiO_2-PA particles into the silica macropores and to avoid their embedding**.** Besides, the affinity

of the methoxy group of MA with PEG is higher than that of the alkyl chain of exylamine. This implies that TiO_2-MA particles remain well dispersed without secondary aggregation in the PEG phase. On the other hand, the TiO_2-EA particles are both incompatible with the silica phase and not well dispersible by PEG resulting in secondary particle aggregations. The effect of the temperature on the stability and morphology of the TS structure was investigated by annealing TS-MA samples at 600, 700, 800, and 900 °C. XRD diffraction (Fig. 4.2bcd) and HRTEM analysis evidence that supported TiO_2 also maintains the anatase phase at the highest temperature treatment, wherein the anatase-rutile transition usually occurs [39]. Moreover, the average size of the particles does not substantially change (Fig. 4.2 inset) even at 900 °C. These effects can be ascribed to the distribution and grafting of titania nanoparticles on the silica surface, either preventing crystal growth or phase transformation usually due to oriented attachment of primary anatase nanocrystals [26]. Finally, at each temperature, no modifications of the macroporous structure were detected, as revealed by Hg porosimetry and SEM analysis (not reported).

Nitrogen physisorption experiments were performed on the pure silica host and on all TS materials. In particular, the adsorption-desorption isotherms and the corresponding pore-size distribution of TS-UC (pseudo-type I) and of TS-MA (type IV) are shown in Fig. 4.10.

The isotherms of TS-UC display high adsorption at low relative pressure, typical of a microporous structure (Fig.4.10a). At higher relative pressure**,** between 0.4 and 0.8 P/P_0, the curve exhibits a very small hysteresis loop indicative of the presence of a small amount of mesopores. This is also confirmed by the corresponding pore-size distribution (Fig. 4.10a inset) in which only a weak peak in the mesopore range appears.

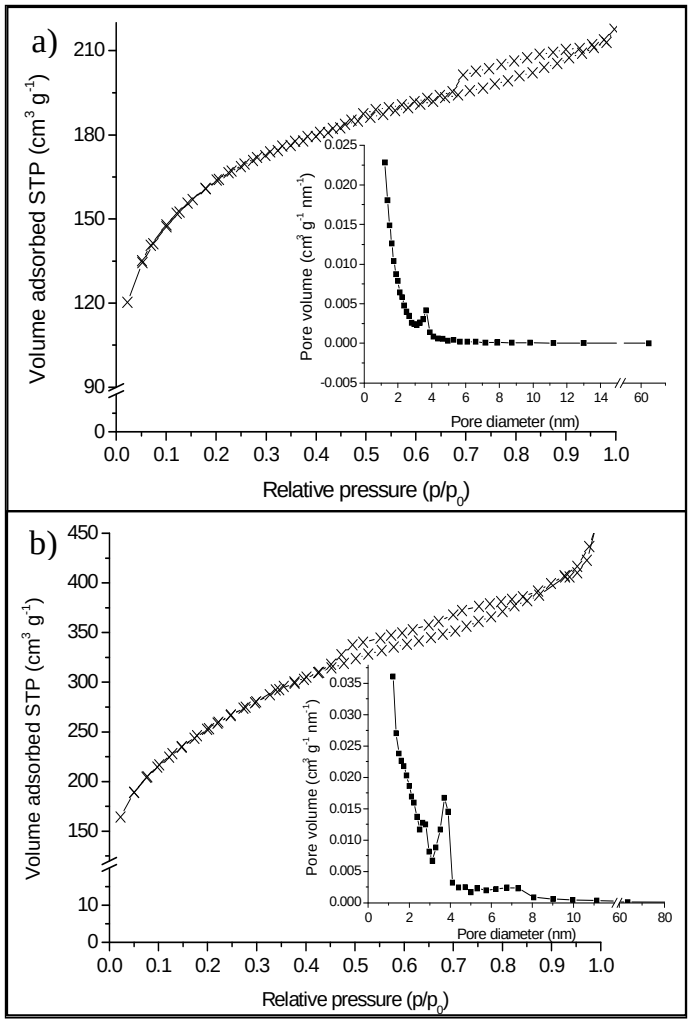

Figure 4.10. Adsorption/desorption isotherms at liquid nitrogen temperature for a) TS-UC and b) TS-MA samples. The curves correspond to a pseudo-type I (a) and type IV (b) isotherms with capillary condensation in the mesopores. Inset: pore size distributions.

Similar isotherms were obtained for pure silica and TS-PA composite (Fig. 4.11a). On the other hand, TS-EA and TS-MA, obtained from TiO_2 nanocrystals functionalized with EA and MA, showed significantly different isotherms. In particular, for TS-MA the resulting isotherm is of type IV and presents a wide hysteresis loop suggesting a remarkable contribution of mesopores (Fig. 4.10b). The pore size distribution (Fig. 4.10b inset) confirms the existence of mesopores with average pore diameter centered on 3.6 nm. A

similar behaviour was observed for TS-EA (Fig. 4.11b), which shows an analogous type IV isotherm but with less pronounced hysteresis loop, suggesting a lower presence of mesopores. Increasing the calcination temperature up to 900 °C, the shape of nitrogen adsorption-desorption isotherm changes and becomes similar to that observed for TS-UC with a decreased contribution of the mesopores (Fig. 4.11c).

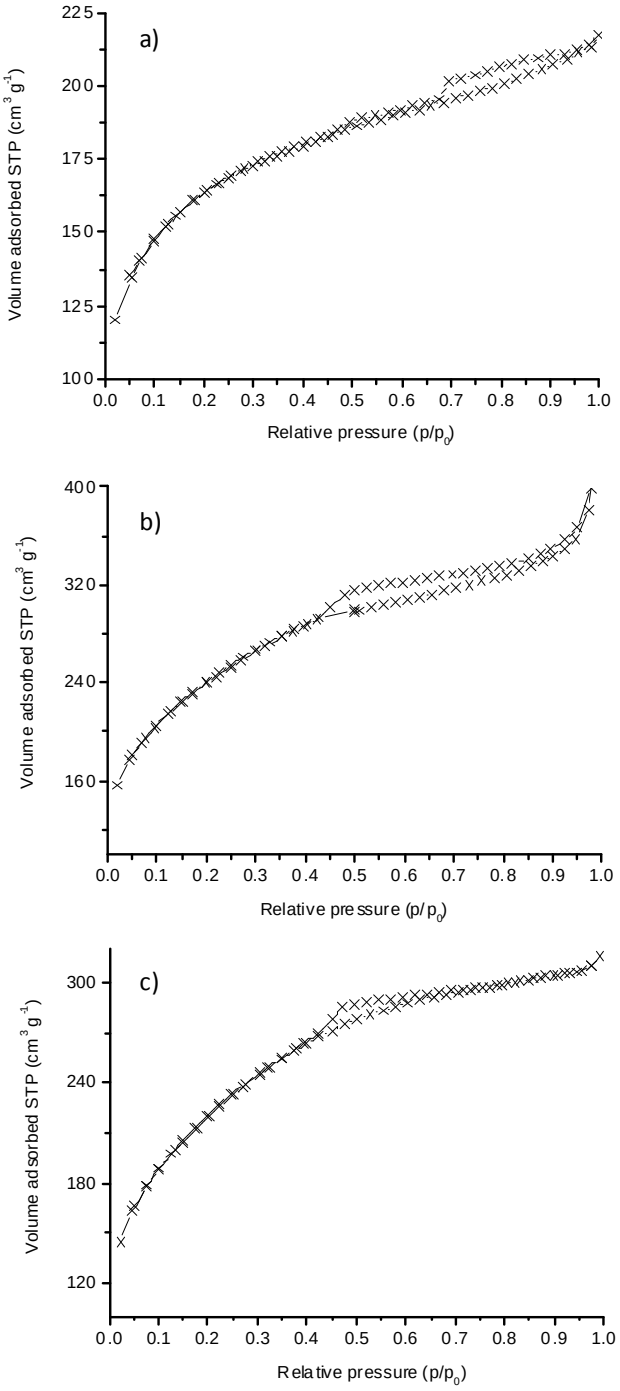

Figure 4.11. Adsorption/desorption isotherms at liquid nitrogen for a) TS-PA, b) TS-EA and c) TS-MA calcined at 900°C

In order to better elucidate the relation between porosity and structure of the functionalizing molecules, the mesopore and micropore volumes of the pure silica and of the composites were calculated and reported in Fig. 4.12. It is very evident that the micropore volume, mainly associated to the silica matrix, remains quite constant in all the samples while there is a huge increase of the mesopore volume in TS-EA and TS-MA compared to the value calculated for TS-UC. On the contrary, TS-PA keeps the mesopore volume unvaried in comparison to TS-UC. Finally, the increase of the calcination temperature to 900 °C in TS-MA produces a relevant but not drastic reduction of the mesopore volume, probably due to the growth of nanoparticle aggregates.

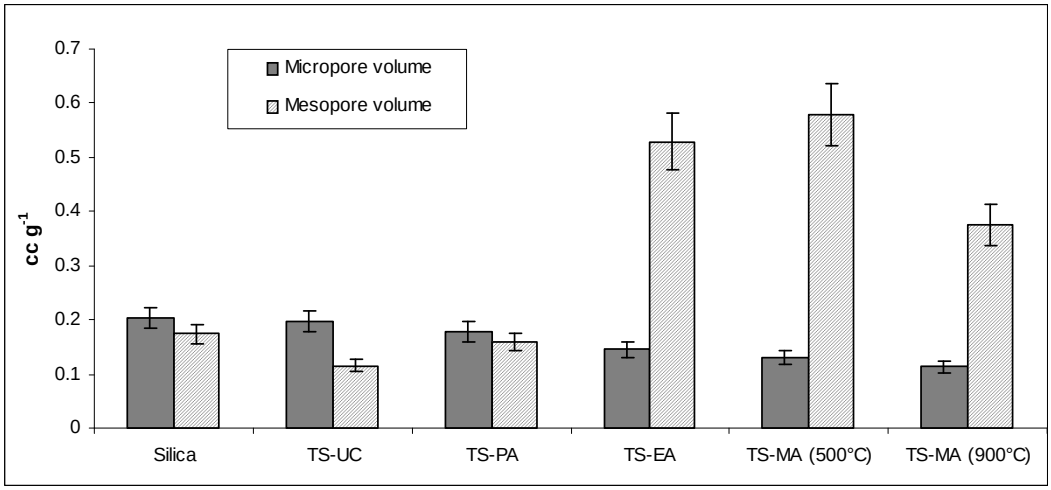

Figure 4.12**.** Mesopore and micropore volumes calculated by the BJH method for pure silica and different TiO_2-SiO_2 samples.

These results confirm the key role of the TiO_2 functionalization in controlling the extent of mesoporosity of the composite materials, in agreement with the corresponding TEM images. In TS-MA, titania nanocrystals well dispersed on the silica surface without secondary aggregation (Fig. 4.9d), originate intra-grain mesoporosity. The lower mesoporosity of TS-EA is relatable to the tendency of TiO_2 crystallites to form large

superficial aggregates (Fig. 4.9c). The very low mesoporosity of TS-PA and TS-UC, similar to that of the pristine silica, depends on TiO_2 nanoparticles fairly totally embedded in the silica matrix (Fig. 4.9a).

The characterization of the material TS-P25 was conducted measuring the material porosity, Hg and N_2 intrusion measurements, and comparing the data with the results obtained for the TS material: the porosities are comparable. The TS-P25 has the same morphological properties of the TS.

4.5.3 Photocatalytic degradation of phenol in water

The photocatalytic activity of TS samples obtained by differently functionalized anatase nanocrystals was measured in the PhOH mineralization in the presence of O_2 under UV radiation and compared to the powder anatase in slurry. The catalyst activity was evaluated by measuring the maximum degradation rate $(dC/dt)_{max}$, which corresponds to the maximum slope point of the fitted curves and the half degradation time $t_{1/2.}$ Both $(dC/dt)_{max}$ and $t_{1/2}$ values were normalized to the same mass (160 mg) of TiO_2.

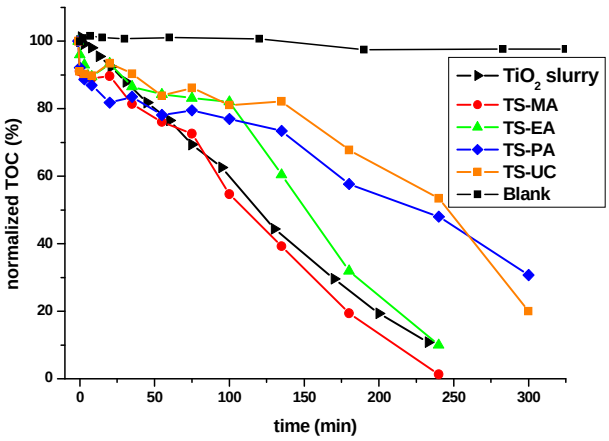

Figure 4.13. Mineralization curves of phenol (given as TOC %) in the presence of O_2 of TS-PA, TS-EA, TS-MA and TS-UC samples compared with TiO_2 catalyst in slurry and with the blank test without catalyst.

The experimental data related to TOC disappearance of PhOH mineralization, for TS samples and slurry, are reported in Fig. 4.13, where 100% TOC at t = 0 is the PhOH concentration measured just before switching on UV irradiation. In all the performed experiments, during the initial phase of recirculation in dark (30 min), the loaded PhOH concentration decreased by about 5.0 ± 1.5 %.

The trends of the calculated values of $t_{1/2}$ and $(dC/dt)_{max}$ are reported in Fig. 4.14a.

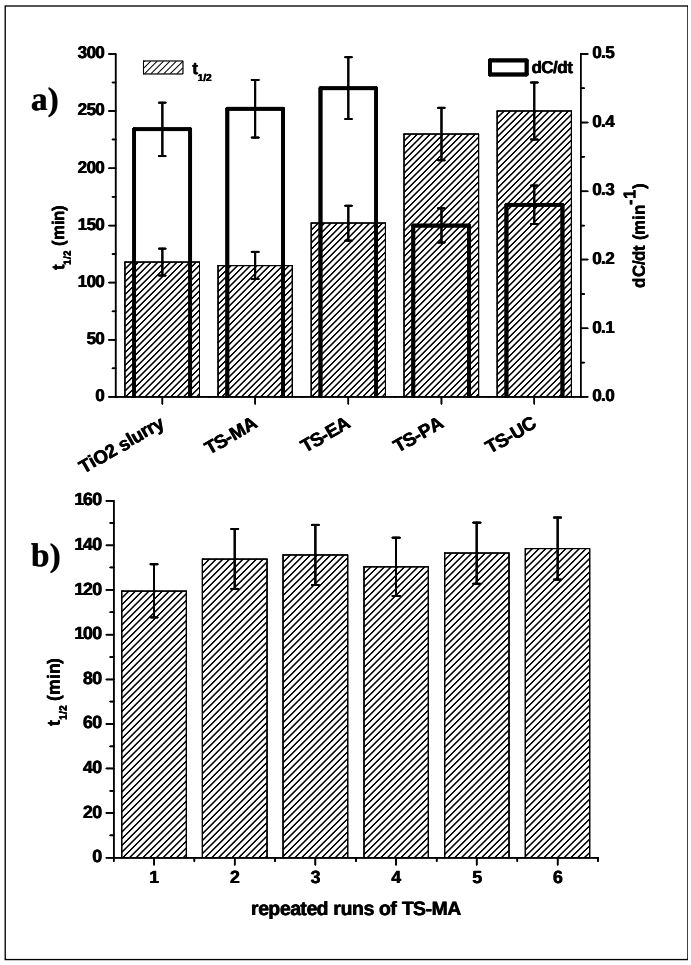

Figure 4.14. (a) Maximum degradation rate $(dC/dt)_{max}$ and half degradation time$_{1/2}$ of different TS materials compared with TiO_2 catalyst in slurry; (b) $t_{1/2}$ of TS-MA after six repeated photomineralisation runs.

In the blank test, without the catalyst, the PhOH mineralization rate is very low, thus indicating a negligible contribution of the direct PhOH photolysis to the whole process. The

overall results evidence that the photoactivity of TS compounds is strongly related to the nature of the functionalizing molecules. In particular, $t_{1/2}$ value decreases and $(dC/dt)_{max}$ correspondingly increases by increasing the chain length of the molecules as well as their affinity with PEG. In particular, TS-PA and TS-UC display the lowest photoactivity, while TS-EA and TS-MA show higher efficiencies. Surprisingly, TS-MA shows the same performance of anatase slurry, thus demonstrating that the TiO_2 immobilization procedure did not affect its catalytic properties. This behaviour can be related to the macroporosity of the silica matrix and to the high catalyst dispersion of anatase nanocrystals on the surface which induces extended mesoporosity in TS-MA composite. These properties guarantee easy mass transport through the material, high accessibility of the catalyst at the solid liquid interface and an intimate contact between the target molecules and the nanoparticles.

The photocatalytic tests were repeated for six successive degradation runs with the same batch, in order to validate the reproducibility of the TS-MA catalytic behaviours. Photoactivity remains substantially constant as demonstrated by the negligible variation of the $t_{1/2}$ (Fig. 9b) and $(dC/dt)_{max}$ (not reported in the figure) calculated for the successive runs.

Finally, the different calcination temperatures have a minor effect on the catalytic properties of TS-MA, as assessed by the very slightly increase of $t_{1/2}$ values with the temperature (115 ± 6 min, 125 ± 6 min and 133 ± 7 min for calcination temperature of 500 °C, 700 °C and 900 °C, respectively) and by the constancy of $(dC/dt)_{max}$ (0.42 ± 0.02 min^{-1}). The overall results confirm that even at highest calcination temperatures morphology of silica, TiO_2 phase and TS-MA composite porosity (see section 3.2) are substantially unchanged preserving the photoactivity.

4.5.4 Photocatalytic degradation of NO_x in air

Experimental details. The gas the reactor used to measure he NOx abatement is a flowing trough reactor i.e. there is no gas recirculation. So that the catalyst efficiency for NO_x abatement is expressed as a percentage of the outlet NO_x concentration. Because the reactor has a flowing through set up a large gas amount is needed to measure some stable values. The measurement precision is generally affected by a time delay to have stable data values because some time is needed to equilibrate the entire pipe lines. Moreover because the NO_x cylinder has a concentration of 80 ppm while the final dilution is in the order of ppb, the mass flow controlling the NO_x has a lower operative range compared to the mass flow controlling the air. So that the controlling range error is higher for the NO_x cylinder than the air one: if the nominal inner concentration is always the same the opening error of the mass flow can cause different effective concentration values. This error is generally of the order of some 10-20 ppb and is stable for every measure campaign: when the nominal value is set the real value doesn't vary till the measure ending. With those assumptions we have to wait some minutes to have stable data.

Gas concentration dependency. Because of the intrinsic discrepancy between the nominal and effective concentrations, we verified if the normalized data, the percentage ratio between outer and inner gas concentrations, can provide the right information regarding the catalyst efficiency. In Fig. 4.15 is reported the abatement efficiency of the TS-P25 with different inner concentrations expressed in ppb. The catalyst efficiency is 74±4% with inner concentration varying from 400 to 120 ppb. Considering the error incertitude the efficiency is quite independent from the concentration. So we can compare the data collected from different measure campaigns despite the variability of the inner gas concentration due to the experimental set up.

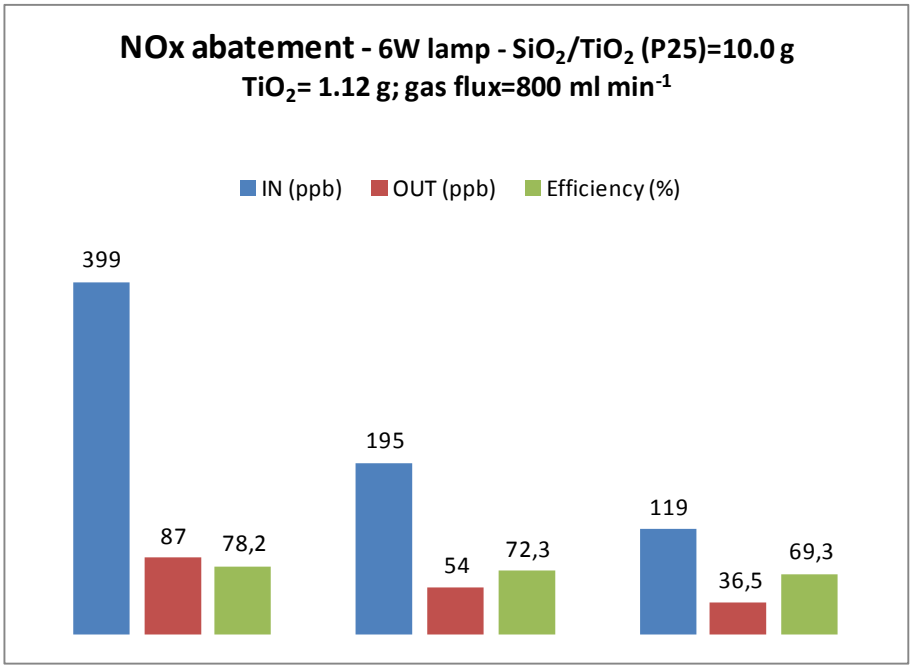

Figure 4.15. NOx abatement efficiency of TS-P25 material respect the inner gas concentartions.

In Fig. 4.16a is reported the NO_x degradation of the TS material by using different lamp intensities with entrance flux flowing inner concentration of 400 ppb and 1200 ml/min. The abatement efficiency Vs. lamp power is around 30 and 90% for 6 and 125W respectively. The efficiency is strictly affected by the radiation intensity.

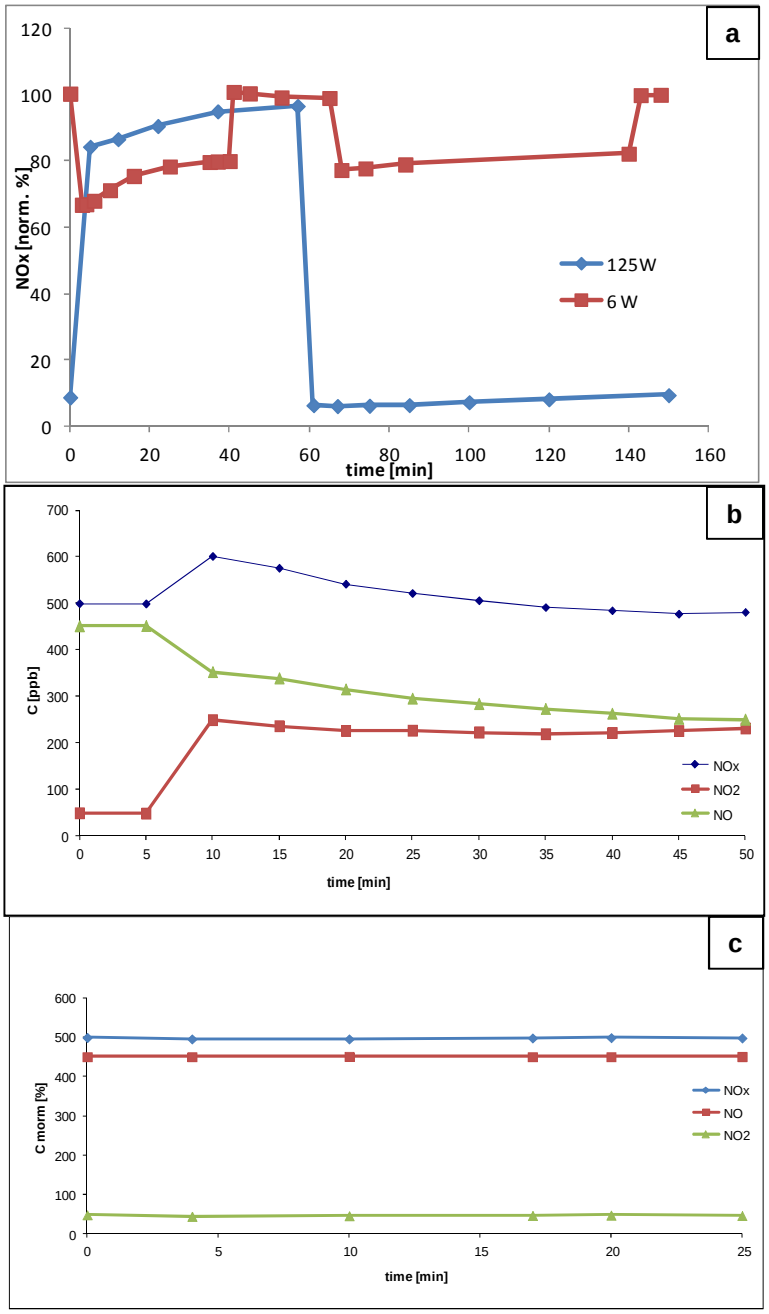

Figure 4.16. a) photocatalytic activity of TS pellets with different lamp power; b) blank of the 125W lamp (no catalyst); c) blank of the 6W lamp (no catalyst). Every experiment was conducted with 1200ml/min as gas flux and 400 ppb as nominal inner gas concentration.

Radiation intensity dependency. Fig 4.16b and c show the effluent gases concentrations (NO, NO_2 and NO_x) in the presence of the two lamp intensities 125 and 6 W respectively without catalyst. The experiments were conducted to measure the lamp influence. The 125 W lamp is able to convert the NO into NO_2 while the 6 W lamp is totally not influent.

Because of the influence of the intensity light on the oxidative phenomena, the 6W lamp was used in order to measure the catalytic activity of the materials avoiding any lamp contribute.

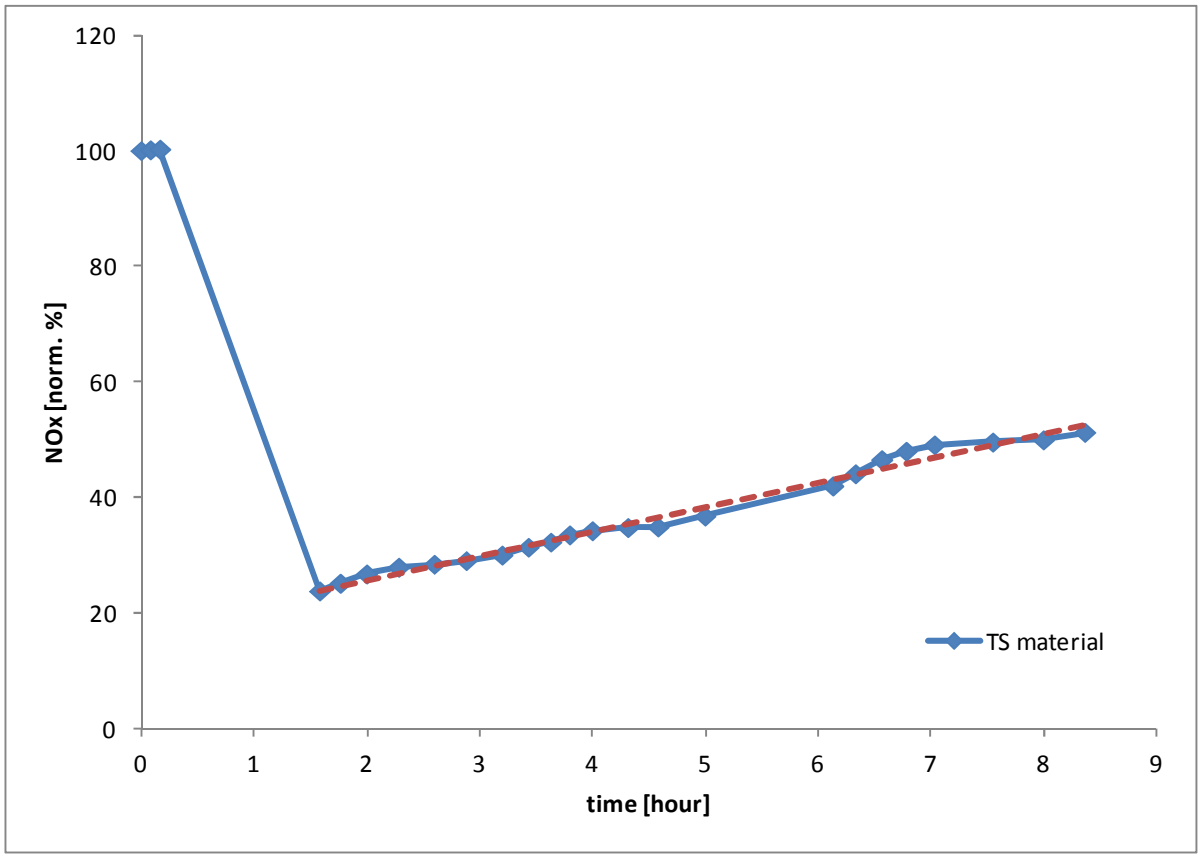

Fig. 4.17. NO_x degradation curve obtained with TS-P25 material as catalyst. The long measuring time is obtained collecting the data from two degradation measurements data sets. The first data set finished after 5 hours while the second started after 2 hours, in the dark, to condition the experimental set-up.

Catalyst saturation. In order to evaluate the catalyst activity reduction several hour measurement could be conducted. As reported in figure 4.17 the data obtained from two measured data sets can be collected and summarized in one curve. After the 5th hour the measure was interrupted. The measure was restarted after the system conditioning i.e. fluxing the gas till the gases concentration measurement is stable. The smoothness of the overall curve suggests that the data combination seems a good approximation of a long

measuring session. During the time the material efficiency was decreases passing from 75% to 50% after 8h 30'. The efficiency decreasing rate is 4.2% base point per hour and it is calculated by the slope of the linear regression curve (red line in Fig. 4.17). The efficiency decrease can be attributed to the surface passivation of the catalyst due to the NO_x conversion into nitrates (see paragraph 4.4) fixed onto the particles surface.

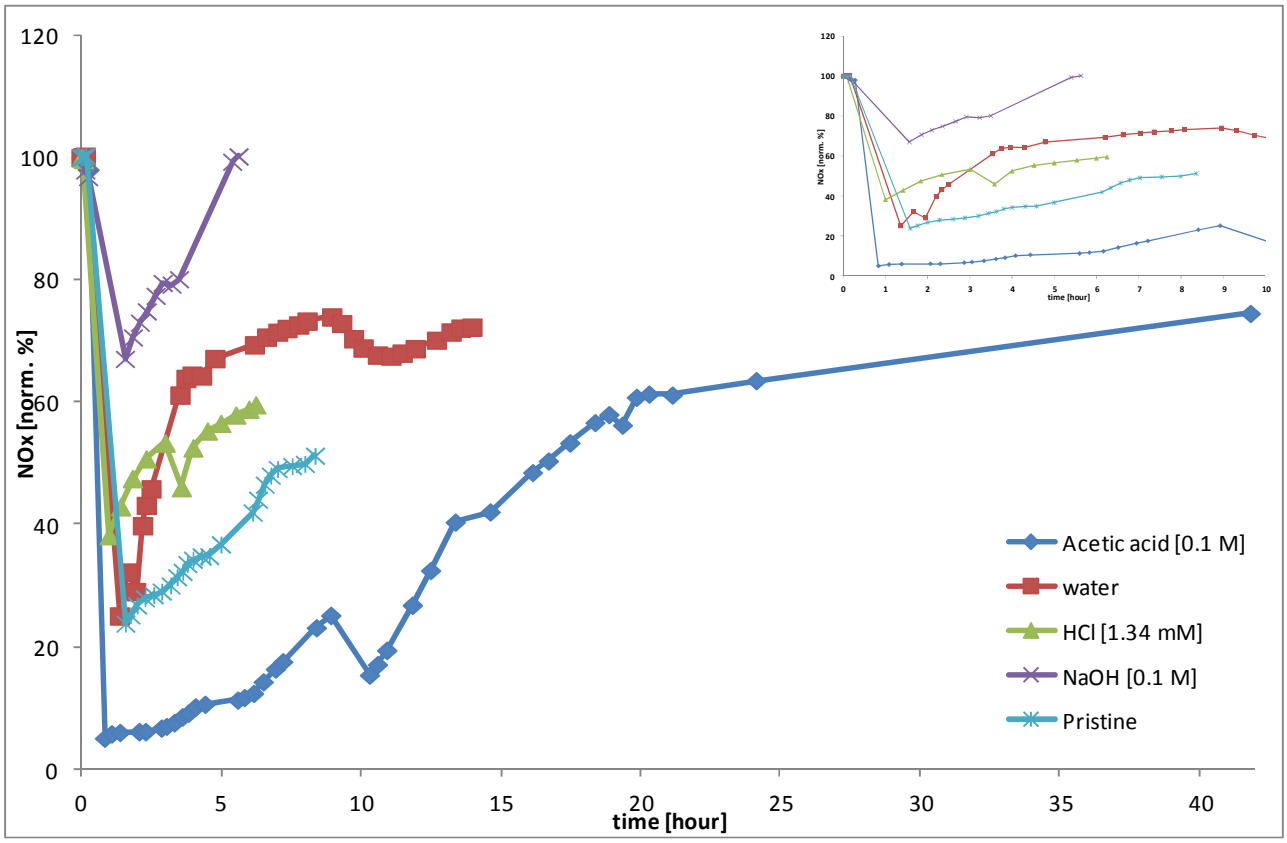

Fig 4.18. Restoring of the catalytic activity washing the TS-P25 catalyst with different solutions. In the insert the magnification of the first 10 hours reaction time.

Catalyst restoration. The catalyst saturation caused by nitrates[40] has to be eliminated washing out the NO_3^-. Different aqueous solutions were tested (water, acetic acid 0.1 M, HCl 1.34 mM, NaOH, 0.1M) submersing the pellets contained in the reactor with the tested solution for 12 hours then rinsed twice with water and then dried at 150°C. After every washing process the material was tested and saturated again (not reported in the figure) to test the other solution. In figure 4.18 the effect of the nitrates removal was evaluated

comparing the photocatalytic activity after washing with the pristine one. The HCl concentration of 1.34mM was choose to have a solution with the same pH of the acetic acid one. As evidenced by the figure 4.18 and more in detail in the magnification the best results were obtained washing with acetic acid and water. The water solution is able to restore the initial condition approximately along the first 2 hours. After this time the catalyst efficiency decreases higher than the pristine one. It seems that the nitrate removal is partial. The best restoring effect was obtained with the acetic acid solution. After 16 hours the catalyst washed with the acetic acid solution has the same efficiency of the pristine one which worked for 7 hours. The explanation of the acetic acid removal ability can be be ascribed to the chelating activity of the acetic acid carboxylic group (see Fig. 4.4) on the titania surface. We used to functionalize the titania surface exploiting the carboxylic group affinity with the surface. The coordinative bonding is more stable than the nitrate ionic bond. Under this condition the nitrate acts as leaving group after the attack of the carboxylic acid. It is not difficult to think that after washing the surface is covered by acetic acid molecules. In the magnification of fig. 4.18 we can see that the pristine and the acetic acid curve slopes is quite the same indicating the nitrate complete removal after the acetic acid washing. Surprisingly the acetic acid is able to increase the photocatalytic efficiency compared the pristine, 95% and 74% respectively. If after washing the titania surface is covered by acetic acid molecules we could ascribe the increased efficiency to the influence of the organic molecules. Two hypothesis could be evocated. The first is the steric hindrance of the acid molecules which could influence the superficial nitrate fixation on the oxide. Being the nitrates not directly bonded to the oxide surface more reactive sites could be available to react with other NO_x molecules. The second hypothesis could evocate the results obtained in the chapter 3 where we demonstrated by EPR measurement that under illumination the organic compounds interact with the photoinduced holes forming some carbon radical. Because the radical is located far from

the crystal surface the electron holes recombination phenomena are reduced. The charges recombination reduction effect, well described in the chapter 1, implies some charges stabilization. Less recombination phenomena implies more charges availability to react with oxygen and water producing the oxidizing species of NO_x and then an increased efficiency.

Despite several efforts, investigating the material by XPS and FT-IR, the nitrates concentration into the material is too low to be detected and every mechanism explanation around the washing activity of the different solutions can be done just speculating on the photodegradation curves.

4.6 Conclusions

TiO_2-SiO_2 composite materials with nanostructured TiO_2 particles grafted onto macroporous silica support were successfully obtained by a novel sol-gel synthetic strategy which employs hybrid organic-inorganic reactants. The materials exhibits high thermal stability and a photocatalytic activity comparable to that of powder TiO_2 in slurry.

The macroporous silica network was synthesized by hydrolysis and condensation of TMOS assisted by PEG as templating agent. TiO_2-SiO_2 were prepared by grafting preformed titania nanocrystals, suitably functionalized by different organic molecules which facilitate their interaction with PEG, onto the macropores of the silica matrix, avoiding their embedding into the support.

Titania dispersion on the silica surface depends on the chain structure of the functionalizing molecules as well as on their affinity with PEG. In particular, the highest affinity of the methoxy group of 2-methoxyethylamine towards PEG enables TiO_2

nanocrystals to maintain the pristine size and to disperse on the silica surface as small mesoporous aggregates, independently of the calcinations temperature.

The double order porous structure of the composites allows high photocatalytic yields. Particularly, TS-MA shows outstanding photoactivity, equal to that of the slurry. This is relatable to the macroporosity of the silica matrix and to the high catalyst dispersion of anatase nanocrystals on the surface, which induces extended mesoporosity of TS-MA composite. These properties guarantee easy mass transport through the material, high accessibility of the catalyst interface and an effective contact between the pollutant molecules and the nanoparticles. The overall results confirm the ability of the immobilization procedure to preserve the functional properties of the photoactive oxide.

Therefore, these highly stable TiO_2-SiO_2 meso/macroporous composite represents a very promising material, easy to be obtained and to be used in various applications. The simplicity of the immobilization method should, in principle, be applicable to support different oxides maintaining unchanged their peculiar functional properties. The use of commercial titania (Degussa P25) to produce another material TS-P25 with similar porosity of TS allowed to demonstrate that the method depicted in the scheme 1 is a general way to produce a catalytic material varying the catalyst and keeping substantially unvaried the matrix of the nanocomposite. Both TS and TS-P25 materials were prepared as pellets and tested in a pre-industrial reactor for NO_x degradation. When fresh prepared the TS-P25 catalytic efficiency passes from 75% to 60% in 6 hours of reaction. In order to remove the nitrate fixed on the surface different aqueous solution were tested. Using acetic acid the efficiency passed from 95% to 70% in 12 hours of reaction. The increased efficiency could be ascribed to the photoinduced charges stabilization caused by the formation of some carbon radical due to the presence of acetic acid molecules chemically bonded onto the surface.

References

[1] a) M. R. Hoffmann, S. T. Martin, W. Choi, *Chem. Rev.* **1995**, *95*, 69; b) T. T. Thomson, J. T. Yates, *Chem. Rev.* **2006**, *10*, 4428; c) X. Chen, S. S. Mao, *Chem. Rev.* **2007**, *107*, 2891.

[2] a) P. Salvador, *J. Phys. Chem. C* **2007,** *111*, 17038; b) U. Diebold, *Surf. Sci. Rep.* **2003**, *48*, 53; c) P. Davit, G. Martra, S. Coluccia, *J. Japan Petr. Inst.* **2004**, *47*, 359; d) J. Theurich, M. Lindner, D. W. Bahnemann, *Langmuir* **1996**, *12*, 6368; e) R. Vinu, G. Madras, *Environ. Sci. Technol.* **2008**, *42*, 913; f) M. Ampo, T. Shima, Y. Kubokawa, *Chem.Lett.* **1985**, *12*, 1799

[3] a) R. Scotti, M. D' Arienzo, A. Testino, F. Morazzoni, *Applied Catalysis B: Environmental* **2009,** *88*, 497; b) R. Scotti, I. R. Bellobono, C. Canevali, C. Cannas, M. Catti, M. D'Arienzo, A. Musinu, S. Polizzi, M. Sommariva, A. Testino, F. Morazzoni, *Chem Mater.* **2008,** *20*, 4051.

[4] a) R. Molinari, L. Palmisano, E. Drioli and M. Schiavello, *J. Membr. Sci.* **2002**, *206*, 399; b) W. Y. Wang, A. Irawan, Y. Ku, *Wat. Res.* **2008,** *42*, 4725; c) W. Xi, S. V. Geisen, *Wat. Res.* **2001**, *35*, 1256.

[5] L. Reijnders, *J. Hazard. Mater.* **2008**, *152*, 440.

[6] M. Tashibi, C. R. Ngah, N. Aziz, A. Mansor, A. Z. Abdullah, L. K. Teong, A. R. Mohamed, *Ind. Eng. Chem. Res.* **2007**, *46*, 9006.

[7] J. Fernandez, J. Kiwi, J. Baeza, J. Freer, C. Lizama, H. D. Mansilla, *Appl. Catal. B* **2004**, *48*, 205.

[8] a) J. C. Lee, M. S. Kim, B. W. Kim, *Wat. Res.* **2002**, *36*, 1776; b) M. D. Nikolaki, D. Malamis, S. G. Poulopoulos, C. J. Philippopoulos, *J. Hazard. Mater.* **2006**, *137*, 1189.

[9] a) S. Horikoshi, N. Watanabe, H. Onishi, H. Hikada, N. Serpone, *Appl. Catal. B* **2002,** *37,*117; b) M. K. Aminian, N. Taghavinia, A. Irajizad, S. M. Mahdavi, *J. Phys. Chem. C* **2007,** *111*, 9794.

[10] a) I. N. Martyanov, N. J. Klabunde, *J. Catal.* **2004**, *225*, 408; b) M. G. Antoniou, D. D. Dionysiou, *Catal.Today* **2007**, *12*, *4*215.

[11] a) Y. Xu, C. H. Langford, *J. Phys. Chem B* **1997**, *101*, 3115; b) F. Li, S. Sun, Y. Jiang, M. Xia, M. Sun, B. Xue, *J. Hazard. Mater.* **2008**, *152*, 1037.

[12] S. N. Hosseini, S. M. Borghei, M. Vossoughi, N. Taghavinia, *Appl. Catal. B* **2007**, *74*, 53.

[13] S. K. Kansal, M. Singh, D. Sud, *J. Hazard. Mater.* **2008**, *153*, 412.

[14] T. H. Xie, J. Lin, *J. Phys. Chem. C* **2007**, *111*, 9968.

[15] a) J. Shang, W. Li, Y. Zhu, *Mol. Catal. A* **2003,** *202*, 187; b) N. Kieda, T. Tokuhisa, *J. Ceram. Soc. Japan* **2006**, *114*, 42.

[16] H. Chen, S. W. Lee, T. H. Kim, B. Y. Hur, *J. Eur. Ceram. Soc.* **2006**, *26*, 2231.

[17] a) Z. Liuxue, W. Xiulian, L. Peng, S. Zhixing, *Surf. Coat. Techn.* **2007**, *201*, 7607; b) B. Tryba, *J. Hazard. Mater.* **2008**, *151*, 623.

[18] a) I. R. Bellobono, R. Barni, F. Gianturco, *J. Membrane Sci.* **1995**, *102*, 139; b) F. Ascari, I. R. Bellobono, P. M. Tozzi, *Fresenius Env. Bull.* **2003**, *12*, 1195; c) I. R. Bellobono, F. Ascari, C. Lagrasta, *Fresenius Env. Bull.* **2003**, *12*, 1536

[19] a) L. G. A. van de Water, T. Maschmeyer, *Top. Catal.* **2004**, *29*, 67; b) Y. S. Lin, *Sep. Purif. Technol.* **2001**, *25*, 39.

[20] a) R. Scotti, M. D'Arienzo, F. Morazzoni, I. R. Bellobono, *Applied Catalysis B: Environmental* **2009**, *88,* 323; b) M. D'Arienzo, M. Crippa, A. A. Essawy, R. Scotti, L. Wahba, P. Gentile, I. R. Bellobono, S. Polizzi, F. Morazzoni, *J. Phys. Chem. C* **2010**, *114*, 15755

[21] a) Y. H. Wang, X. Q. Liu, G. Y. Meng, *Materials Science and Engineering A* **2007**, *445*, 611; b) M. A. Anderson, M. J. Gieselmann, Q. Xu, *J. Membr. Sci.* **1988**, *39*, 243; c) F. Bosc, A. Ayral, P. A. Albouy, L. Datas, C. Guizard, *Chem. Mater.* **2004**, *16*, 2208; d) G. Balasubramanian, D. D. Dionysiou, M. T. Suidan, V. Subramanian, I. Baudin, J. M. Laıˆne´, *J. Mater. Sci.* **2003**, *38*, 823; e) P. C. A. Alberius, K. L. Frindell, R. C. Hayward, E. J. Kramer, G. D. Stuchy, B. F. Chmelka, *Chem. Mater.* **2002**, *14*, 3284; f) S. Y. Kwak, S. H. Kim, S. S. Kim, *Environ. Sci. Technol.* **2001**, *35*, 2388.

[22] a) H. Choi , E. Stathatos, D. D. Dionysiou, *Applied Catalysis B: Environmental* **2006**, *63* 60; b) F. Bosc, P. Lacroix-Desmazes, A. Ayral, *Journal of Colloid and Interface Science* **2006**, *304* 545; c) A. Julbe, V. Rouessac, J. Durand, A. Ayral, *Journal of Membrane Science* **2008**, *316*, 176; d) H. Bai, Z. Liu, D. D. Sun, *Chem. Commun.* **2010**, *46*, 6542; e) H. Choi, A. C. Sofranko, D. D. Dionysiou, *Adv. Funct. Mater.* **2006**, *16*, 1067.

[23] P. Colombo, C. Vakifahmetoglu, S. Costacurta, *J. Mater. Sci.* **2010**, *45*, 5425.

[24] N. Tanaka, H. Kobayashi, N. Ishizuka, H. Minakuchi, K. Nakanishi, K. Hosoya, T. Ikegami, *Journal of Chromatography A* **2002**, *965*, 35.

[25] N. Nakayama, T. Hayashi, *Colloids and Surfaces A : Physicochem. Eng. Aspects* **2008**, *317*, 543.

[26] A. Testino, I. R. Bellobono, V. Buscaglia, C. Canevali, M. D'Arienzo, S. Polizzi, R. Scotti, F. Morazzoni, *J. Am. Chem. Soc.* **2007**, *129*, 3564.

[27] N. Nakayama, T. Hayashi, *Colloids and Surfaces A: Physicochem. Eng. Aspects* **2008,** *317*, 543.

[28] S. Brunauer, P. H. Emmet, E. Teller, *J. Am. Chem. Soc.* **1938**, *60*, 309.

[29] E. P. Barret, L. G. Joyner, P. P. Halenda, *J. Am. Chem. Soc.* **1951**, *73*, 373.

[30] R. Scotti, M. D'Arienzo, F. Morazzoni, I. R. Bellobono, *Appl. Catal., B* **2009**, *88*, 323.

[31] http://en.wikipedia.org/wiki/Selective_catalytic_reduction

[32] A. Fujishima_, T. N. Rao, D. A. Tryk, Journal of Photochemistry and Photobiology C: Photochemistry Reviews 1,**2000**, 1–21

[33] D. H. Chen, K. Li, Photocatalytic Coating on Road Pavements/Structures for NOx Abatement, U.S. Environmental Protection Agency Research Triangle Park, NC 27711

[34] a) D. P. Cistola, D. M. Small, J. A. Hamilton, *J. Lipid Res.* **1982**, *23*, 795; b) H. Tomita, F. Sanda, T. Endo, *J. Pol. Sci. Part A: Pol. Chem.* **2001**, *39*, 3678; c) E. Breitmeier, W. Voelter, in *Carbon 13 NMR Spectroscopy*, VCH Verlagsgesellschaft GmbH, Weinheim, Germany **1987**, Ch 2.

[35] a) A. E. Tonelli, in *NMR Spectroscopy and Polymer Microstructure: The Conformational Connection*, VCH Verlagsgesellschaft GmbH, Weinheim, Germany **1989**, Ch.6; b) D. M. Grant and B.V. Cheney, *J. Am. Chem. Soc.* **1967**, *89*, 5315.

[36] L. Ojam¨ae, C. Aulin, H. P edersen, P.O. K¨all, *J. Colloid Interface Sci.* **2006**, *296*, 71

[37] D. V. Leff, L. Brandt, J. R. Heath, *Langmuir* **1996**, *12*, 4723

[38] I.Luzinov, D. Julthongpiput, H. Malz, J. Pionteck, V. V. Tsukruk *Macromolecules* **2000**, *33*, 1043.

[39] C. Byun, J. W. Jang, I. T. Kim, K. S. Hong, B. W. Lee, *Materials Research Bulletin* **1997**, *32*, 431.

[40] H.Y. Huang et al./Applied Catalysis B: Environmental 33 (2001) 127–13v

CHAPTER 5

TiO_2-Polystyrene Nanocomposite as Dielectric Material

5.0 Introduction

High dielectric constant (ε_r) materials received great interest from various technological applications as gate dielectrics,[1] electroactive devices[2] and charge-storage capacitors.[3] Moreover the same materials were investigated as a base for storage energy devices in electric powered vehicles and pulse power applications.[4] In these contexts, polymeric materials offer a new approach towards low cost and flexible large area electronic devices,[5] although they require the dielectric properties to be enhanced[6,7] preserving flexibility. In fact high dielectric constant materials, like titanium dioxide (ε_r = 31, anatase; $\varepsilon_r \approx 114$, rutile),[8] strontium titanate ($\varepsilon_r \approx 150$)[9] or $Ba_{0.6}Sr_{0.4}TiO_3$ (ε_r = 4000)[10], display the right electrical properties but they are not easily processable,[11] instead easily processable systems such as polymers, poly(methyl methacrilate) (ε_r = 3.12)[12] or polystyrene (ε_r = 2.6, PS)[13], typically exhibit low dielectric constants.

Polymer-inorganic composites in principle offer the possibility of combining the desired electric properties with flexibility and printability.

Recent studies showed a moderate increase in the dielectric permittivity by incorporating high ε_r nanofillers such as titania,[14] zirconia,[15] alumina,[16] barium titanate[17] into a polymeric matrix. Badheka[17] reported that the incorporation of nanometric particles of barium titanate (40 vol %) in PS increases the dielectric constant from 2.6 to a significant 20, but it is still much lower than the value ε_r = 1700 [18] of the ceramic phases.

The dielectric properties of a composite material depend on the ε_r of the components, i.e. the matrix and the filler, and particularly on the loading, size, shape and orientation of the particles.[19] Many models described the effective dielectric properties of materials incorporating particles into a continuous matrix[19]. When the filler volume within the matrix increases, the formation of a microcapacitor network occurs.[20] These microcapacitors are

formed by neighbouring conductive filler particles and thin layers of dielectric in between, contributing to a very large capacitance.[21] Some of the conductive filler particles within the capacitive microstructures are connected in parallel and some others in series. The connection in parallel is able to increase the material capacitance.[21] The large capacitance contributed by these microcapacitors induces a significant increase in the intensity of the local electric field and promotes the accumulation of charge carriers at the filler-matrix interface. This polarization, known as Maxwell-Wagnar effect, is responsible for the enhancement of the dielectric constant.[22] When the density of the microcapacitors becomes very relevant, a conductive network takes place and a percolation phenomenon appears as a discharge between the electrodes.[23]

Basing on this model the trend of the electric properties with the filler concentration shows three regions.[24] The first region is defined for low filler amount, the dielectric constant gradually rises with the concentration. The particles are randomly dispersed and their contribution to the ε_r is well predictable by the classical mixing formulae.[19] Further increase of the filler concentration i.e. the second region causes the formation of microaggregates acting as microcapacitive structures. The consequent enhancement of the dielectric constant can be described according to:[24,25,26]

$$\varepsilon_r = c\, A^{-q} \qquad (1)$$

where ε_r is the relative dielectric constant, c is a constant prefactor, $A = (v_c - v)/v_c$ is the reduced volume fraction, v is the volume fraction of the particles, v_c is the percolation threshold and q has the critical value about 1. In order to fit the experimental data, some authors use the dielectric constant of the matrix as c prefactor[24]; we will use q, v_c and c as adjustable parameters. In the third region, at high filler concentration, the microaggregates connect, causing the formation of the conductive network and the consequent ε_r decrease.[26] Between the second and the third region lies the percolation threshold i.e. the

critical filler volume fraction where the connectivity between the particles extends throughout the system.[19] Furthermore the dielectric loss (tanδ) defined as the ratio between the lossy response to the electric field and the lossless one, arises.[27] Tanδ is representative of the material energy dissipation, thus a suitable material should have high ε_r and low tanδ.

It appears that at the microscopic level the amount and the distribution of a specific filler into the matrix are the main parameters to control to achieve high ε_r and low tanδ. The beneficial properties derived from the dispersion of high dielectric inorganic particles into a polymer matrix result maximized when the particles are homogeneously distributed at the nanometric level.[28] Unfortunately polymer matrices are not generally polar and compatible with the surfaces of the inorganic particles. Thus, one of the main issues in the fabrication of nanocomposites is the surface modification of the filler nanoparticles to make them compatible with the polymer.

TiO_2 surface strongly chemisorbs low molecular weight molecules containing functional groups like amines,[29] phosphonic acids,[30,31,32] or carboxylic acids.[33] However, the short ligands are insufficient to completely hinder particle aggregation through residual hydroxyl groups. Thus the use of bulkier surface modifiers would drastically diminish the possibility of close contacts between nanoparticles[34] and polymer chains grafting nanoparticles can provide a bulky shielding of the surface. Two main strategies can be used: ‘‘grafting to’’ and ‘‘grafting from’’. In the ‘‘grafting to’’ approach, polymer chains with an active terminal group react with suitable sites on the nanoparticle surface. Some authors used this approach to synthesise TiO_2 anatase core shell particles with different grafted polymers.[35, 36, 37] Although this method is relatively easy, the attachment of some chains to the surface results in a spatial hindrance which can limit the reaction between a great number of chains and the functional groups at the surface. Hence, this method leads to relatively low

grafting densities. In the ‘‘grafting from’’ approach the polymer is directly grown on the nanoparticle surface, previously functionalized with molecules capable of initiating the polymerization. The low hindrance of the initiators results in a high coverage of the surface. Thus the monomeric units diffuse towards the propagating sites giving the advantage of a dense and thick polymer layer.

Many surface-initiated polymerization techniques have been used to graft polymer chains onto silica and titania such as the atom-transfer radical polymerization (ATRP),[38,39] nitroxide-mediated polymerization (NMP)[40] and the reversible addition-fragmentation chain transfer polymerization (RAFT).[41,42] Among these methods, RAFT polymerisation is known to be a powerful tool to obtain polymers with low polydispersity and consequently a uniform polymeric layer[41] on the surface. These properties well compatibilize the inorganic phase with the polymer matrix thus providing homogeneous filler dispersion.

Here we report the preparation of new composite materials obtained by coupling polystyrene matrix with rutile TiO_2 nanocrystals. These hybrids show high dielectric constant and low dissipation factor.

Polystyrene-functionalized core-shell TiO_2 rutile nanoparticles were obtained via “grafting from” polymerization of styrene using RAFT agents anchored on the titania surface . The anchoring allows to obtain *class II* hybrid material because the coordinative bonding of the RAFT reagent with the superficial titanium atoms.[43] Then the particles were dispersed into polystyrene matrix. The filler amount which can be added before approaching the percolation threshold resulted very high compared with those reported in the literature.

The material was morphologically studied by Transmission Electron Microscopy (TEM) and electrically characterized by impedance spectroscopy. Combining the results it appeared that the formed chestnut-like rutile aggregates play a decisive role in building the

capacitive microstructures which increase the dielectric polarization effects. As well as the polystyrene shell provides an excellent compatibilization of the particles, a homogeneous dispersion of the inorganic semiconductor into the organic matrix and a very thin layer of dielectric material between the neighbouring filler particles.

5.1 Preparation

All chemicals and solvents were purchased from Sigma-Aldrich as analytical grade and used as received without further purification, with the exception of styrene which was distilled at reduced pressure and dehydrated on $CaCl_2$.

5.1.1 Synthesis of the RAFT chain transfer agent (CTA)

The RAFT chain transfer agent (CTA), S-1-Dodecyl-S'-(α,α'-dimethyl- α''-acetic acid) trithiocarbonate was synthesized following the procedure introduced by Lai et al.[44]. 1-Dodecanethiol (48.07 ml, 0.20 mol), acetone (120 ml), and tricaprylylmethylammonium chloride (3.24 g, 0.008 mol) were mechanical stirred in a jacketed reactor at 10 °C under N_2 atmosphere. A NaOH (50%) solution (8.38 ml, 0.21 mol) was then added dropwise in 20 min. and stirred for 15 min. Then a solution of acetone (24.54 ml, 0.33 mol) and carbon disulfide (12.07 ml 0.20 mol) was added dropwise in 20 min. After further 20 min, 24.36 ml (0.30 mol) of chloroform were added, followed by dropwise addition of NaOH (50%) solution (40 ml, 1.53 mol) in 30 min. After overnight under stirring, 600 ml of distilled water were added at room temperature, followed by 50 ml of concentrated HCl (37*%)*. Nitrogen was purged through the reactor with vigorous stirring to evaporate the acetone. The obtained solid was suspended in 600 ml of 2-propanol and the undissolved solid (S,S'-

bis(1-dodecyl) trithiocarbonate) was filtered off. The 2-propanol solution was evaporated and the resulting solid was recrystallized from hexanes two times.

Yield 47.12 % of yellow crystalline solid; m_p = 63.01 °C determined by DSC. FT-IR ATR: 1060 cm^{-1} C=S groups, 1703 cm^{-1} C=O groups. ^{1}H NMR ($CDCl_3$): 0.90 (t, 3H, -C**H$_3$**), 1.28 (m, 16H, -(C**H$_2$**)$_8$-), 1.40 (m, 2H, CH_3-C**H**$_2$-), 1.70 (m, 2H, -S-CH_2-C**H$_2$**-), 1.74 (s, 6H, -C**H$_3$**), 3.37 (t, 2H, -S-C**H$_2$**-), 11.90 (s, 1H, -O**H**). ^{13}C NMR ($CDCl_3$): 14.14 (-CH_3), 22.70-31.93 (-$(CH_2)_8$-), 37.07 (-S-CH_2-), 55.61 (-**C**$(CH_3)_2$), 179.18 (C=O), 220.77 (-**C**=S).

5.1.2 TiO_2 Functionalisation with RAFT reagent

The preparation of core-shell particles was performed in two steps (Scheme 5.1): a) functionalisation of TiO_2 nanoparticles with the RAFT agent (TiO_2-CTA) b**)** RAFT polymerization of styrene (TiO_2-ST).

Nanocrystalline TiO_2 rutile was obtained by hydrothermal synthesis, according to the previously reported procedure [45], by reacting aqueous solutions of $TiOCl_2$ (Aldrich, 99 %) and NH_3 (Fluka, > 25 wt %) in a teflon lined autoclave (Parr, model 4768Q) at 220°C.

5 g of TiO_2 were suspended, in anhydrous conditions, in 50 ml of anhydrous methanol. A large excess of S-1-Dodecyl-S'-(α, α'-dimethyl- α''-acetic acid) trithiocarbonate (0.5 g) was then added and the suspension was kept 96 hours in the dark under stirring at RT in inert atmosphere. The particles were recovered by centrifugation (30 min at 6000 RPM). In order to remove the unreacted CTA and the residual traces of methanol, the powder was washed for 20 minutes under ultrasound conditions with ethyl acetate (3 times with 50 mL) and CH_2Cl_2 (3 times with 50 mL). The final wet powders were dried in air at room temperature and the residual solvent evaporated under vacuum overnight.

5.1.3 Polystyrene Polymerization "From" the Surface

4.5 g of functionalized particles (TiO_2-CTA), with a resulting transfer agent net content of $1.31*10^{-4}$ mol, were kept at reduced pressure (10^{-2} torr) for 2 hours before the addition of 104 ml (0.94 mol) of styrene (styrene:CTA molar ratio = 7200). The mixture was homogeneously dispersed by ultrasound treatment and four freeze-pump-thaw cycles were performed to remove the oxygen. The polymerization reaction was conducted at 110°C for 96 h under N_2 atmosphere and was interrupted cooling the mixture in liquid N_2. In order to separate *TiO_2-PS* from the ungrafted polystyrene the solid was dissolved in CH_2Cl_2 (300 ml) and the particles separated by centrifugation (6000 RPM for 30 min). The recovered particles were washed tree times with CH_2Cl_2 in ultrasound conditions, separated by centrifugation and finally dried in vacuum overnight.

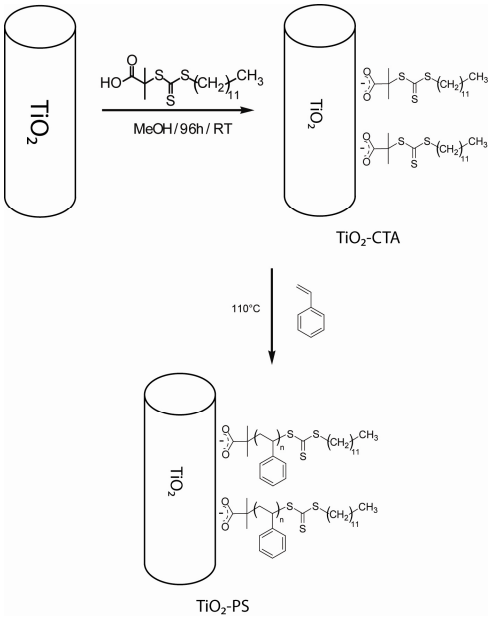

Scheme 5.1 Schematic diagram illustrating the process of RAFT polymerization on the surface of rutile nanoparticle

Cleavage of grafted polystyrene from TiO_2 nanoparticles

In order to measure the polymerization degree of the PS chains grafted on TiO_2-PS by GPC (see paragraph 5.2) the polymer was cleaved from the core shell particles according the following procedure.

About 110 mg of TiO_2-PS were dissolved in a solution of 50 mL of THF and 2 mL of HCl (2M). The solution was stirred at 80 °C under reflux for 24 hours. After the precipitation of a white powders, the solid was removed by centrifugation (6000 RPM for 15 min). The supernatant was reduced in volume and the polymer was recovered and purified through precipitation in methanol. The obtained polystyrene was dried under vacuum for 24 hours (10^{-2} torr).

5.1.4 Material Deposition and Device Realization

Different amounts of TiO_2-PS powders and commercial polystyrene Mi14 (reported in Table 5.1) were dispersed in 1 mL of chloroform and dichlorobenzene 1:1 v:v solution and the relative concentration, reported as TiO_2:PS volume fraction, was calculated using 1.04 g/cm^3 and 4.17 g/cm^3 as PS and rutile density, respectively.

Table 5.1. Amounts of TiO_2-PS and commercial PS used to prepare composites at different concentration. The relative volume fractions are calculated using 1.04 g/cm^3 and 4.17 g/cm^3 as PS and TiO_2 density, respectively

TiO_2-PS [mg]	PS Mi14 [mg]	TiO_2 % vol.	PS % vol.
230	0	64.1	35.9
180	18	49.5	50.5
135	34	36.9	63.1
95	48	28.9	71.1
65	59	19.7	80.3
35	70	11.1	88.9

In order to guarantee an appropriate dispersion during the deposition process, the suspensions underwent ultrasound treatment for 60 min. A micrometric film was obtained through blade coating deposition on a Cu substrate that constitutes the lower contact. The solvent was evaporated for 72 hours at RT and the upper contact was realized via Au sputtering deposition using two circular masks of 15.46±0.05 mm and 4.95±0.05 mm in diameter. The resulting device, modelled as a parallel and flat plates capacitor, was annealed at 140 °C under nitrogen for 4 hours before the dielectric characterization.

5.2 Characterization Methods

X-ray diffraction (XRD) patterns of the powders were collected with a Brucker D8 Advance (Cu Kα radiation) in the range 20-80° 2θ (2θ step 0.025°, count time of 2 s per step).

ATR-FTIR analysis was performed by a Perkin Elmer Spectrum 100 instrument scanning from 650 to 4000 cm^{-1} with a resolution of 4 cm^{-1} for 64 scans. Quantitative determination

of the amount of organic molecules which functionalize the oxide was performed by Thermo Gravimetric Analysis (TGA) and Differential Scanning Calorimetry (DSC) measurements on a Mettler Toledo TGA/DSC1 STAR^e System, at constant gas flow (50 cm^3 min^{-1}). Thermal profile was the following: 40 °C 5 min (N_2); 40-150 °C 10 °C/min (N_2); 150 °C 5 min (N_2); 150-1000 °C 10 °C/min (air).

Molecular weights and molecular weight distributions were determined by Gel Permeation Chromatography (GPC) using a WATERS 1515 isocratic equipped with a HPLC Pump, WATERS 2414 refractive index detector, four Styragel columns (HR2, HR3, HR4 and HR5 in the effective molecular weight range of 500–20000, 500–30000, 50000–600000 and 50000-4000000 respectively) with THF as eluent at a flow rate of 1.0 mL/min^{-1}. The GPC system was calibrated by standard polystyrene from Sigma-Aldrich.

NMR spectra were recorded on a BRUKER AVANCE 500 spectrometer using $CDCl_3$ as solvent.

Specific surface area (SSA) by BET method [46], was measured by Nitrogen physisorption with a Quantachrome Autosorb-1 apparatus. Powder samples were evacuated at 200 °C for 16 h before the analysis.

Scanning electron microscopy (SEM) measurements were performed by a LEO 1450VP instrument.

Transmission Electron Microscopy (TEM) analysis was carried out with a Jeol JEM-3010 instrument equipped with a Energy Dispersive Spectroscopy (EDS) system ISIS Series 300 manufactured by Oxford Instruments. The microscope was operated at 300 kV with a liquid nitrogen cooled sample holder. The latter was used to lower the specimen temperature down to -182°C in order to avoid beam damage. Samples were embedded into Araldite epoxy resin and then 100 nm slices were cut by Leica UC6 ultramicrotome. In

order to cut plan (rather than cross or randomly oriented) sections, in the embedding process care was taken to keep samples flat and to orient them perpendicularly to the flat base of the resin mould. The impedance measurements were performed using a HP 4282A Precision LCR Meter in configuration C_p-G. The maximum tension was 1V while the frequency varied between 20 Hz and 1 MHz. The final electrical characteristics of the material for each concentration of filler were obtained averaging the data collected for the two different dimension of the top contact.

5.3 Results and Discussion

5.3.1 Functionalised TiO_2

TEM and HRTEM images of the employed TiO_2 rutile nanocrystals are reported in Fig. 5.3.1. The hydrothermal procedure adopted allowed to produce particles which are single nanocrystals, with pronounced faceting and with highly reproducible morphology. No internal pores or amorphous surface layers were detectable. The nanocrystals have elongated prismatic shape (rod-like) with length 160-200 nm and width 25-30 nm (Fig. 5.3.1a). They grow in the [001] direction (Fig. 5.3.1b) and have the tendency to form aggregates by sharing the [110] faces.

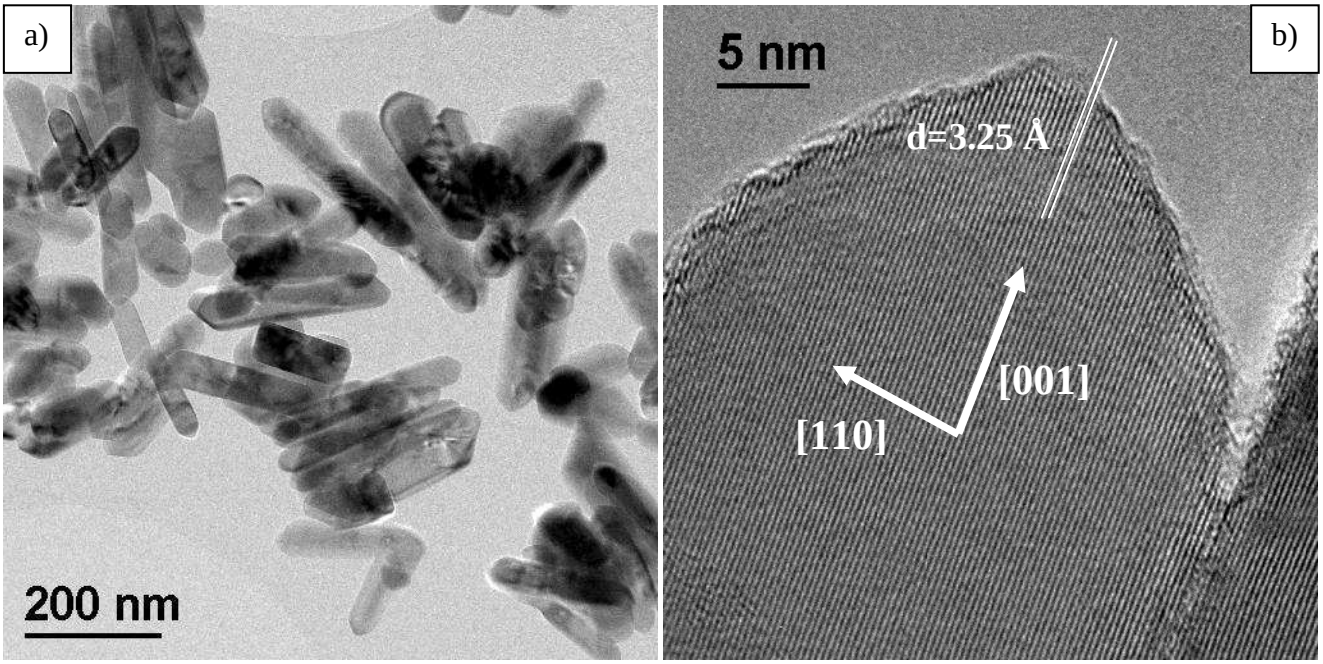

Fig. 5.3.1. TEM (a) and HRTEM (b) images of hydrothermally obtained rutile nanocrystals.

Rutile nanoparticles functionalized with RAFT chain transfer agent (TiO_2-CTA) and with polystyrene via "grafting from" polymerization (TiO_2-PS) were characterized by FTIR spectroscopy comparing them with the pristine rutile (Fig. 5.3.2) in order to assess the grafting of surface functional groups. FT-IR ATR spectrum of TiO_2-CTA showed the stretching modes of methyl and methylene groups at 2956, 2924 and 2855 cm^{-1}. This assessed the integrity of the grafted CTA aliphatic chain b 3. The CTA interaction with TiO_2 is demonstrated by the absence of the C=O vibration mode at 1703 cm^{-1}, characteristic of the free aliphatic acids, and by the presence of both asymmetric and symmetric stretching bands of the deprotonated carboxyl moiety (COO^-), respectively at 1504 and 1434 cm^{-1} [47]. The spectrum of TiO_2-PS clearly showed the presence of PS, since the notable peaks are very evident, being in the range of 3000-3100 cm^{-1} the C-H stretching modes and in the range 1450-1650 cm^{-1} the C-C stretching mode due to phenyl rings [48].

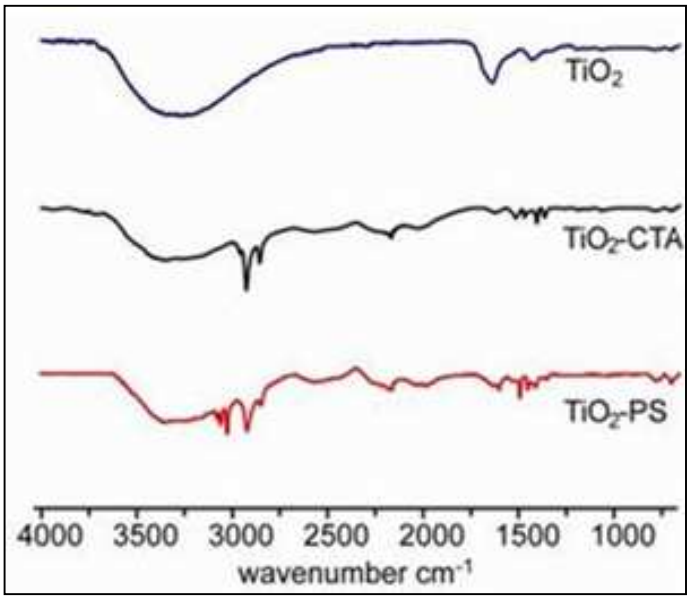

Fig. 5.3.2. FT-IR spectra of bare rutile nanoparticles, CTA grafted rutile nanoparticles (TiO_2-CTA) and PS grafted rutile nanoparticles (TiO_2-PS).

The total amount of the RAFT transfer agent grafted to TiO_2 and the average PS chain length were evaluated by TGA analysis (Fig. 5.3.3). The amount of the functionalizing molecules was calculated by the net weight loss of TiO_2-CTA between 150° C and 600° C, i.e. the total weight loss excluding that of bare TiO_2. From the measured weight loss of 1.01%, the amount of grafted RAFT in TiO_2-CTA agent was evaluated 0.28 mmol/g. Assuming that the molecules were equally distributed on the surface and referring to the surface area of pristine rutile 36 m^2/g (measured by BET), the number of molecules per nm^2 (Σ) resulted 0.5 CTA/nm^2. Thus the average distance ($D=\sqrt{4/\pi\Sigma}$) between the molecules anchored to the surface is 1.6 nm. For TiO_2-PS nanoparticles the weight loss attributed to the polymer grafted on the TiO_2 resulted 12.2±0.2 %. Assuming that each grafted transfer agent molecule enables the growth of a single chain, and that the RAFT technique ensures a very low polydispersity, the chain length was estimated in 42 styrene repeated units.

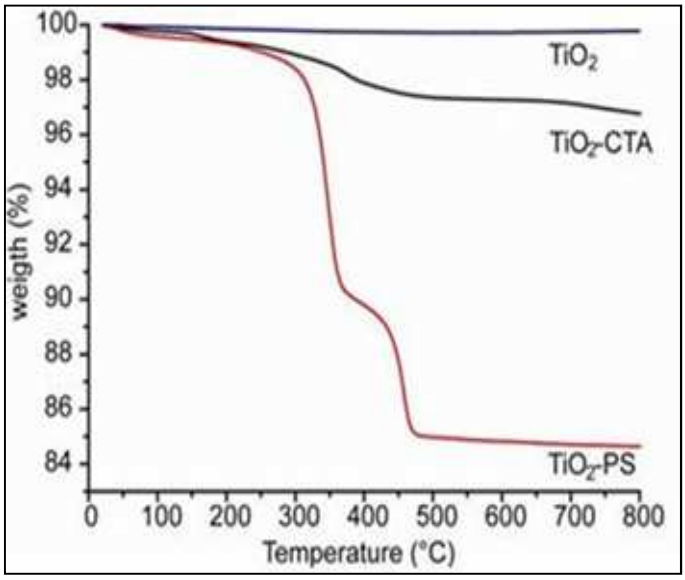

Fig. 5.3.3. TGA curves of bare rutile nanoparticles, CTA grafted rutile nanoparticles (TiO_2-CTA) and PS grafted rutile nanoparticles (TiO_2-PS).

More detailed evidence of the polymerization on the TiO_2 surface is provided by the ^1H NMR investigation of $CDCl_3$ colloidal dispersion of core shell PS/TiO_2 nanoparticles (Fig.5.3.4). The signals of PS (aromatic protons δ = 6.5-7.2 ppm, CH_2 and CH protons δ =1.3-2 ppm) with line width characteristic of long macromolecular chains and two signals of the CTA (CH_3 and CH_2 of the dodecyl residue) with reduced line width distinctive of terminal groups, were detected.

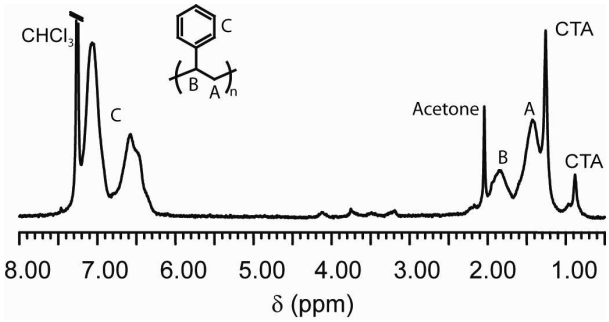

Fig.5.3.4. ^1H NMR spectrum of PS chains grafted on rutile nanoparticles

GPC analysis of the polystyrene cleaved from the nanoparticles gave molecular weight Mn= 4800 g/mol (PDI = 1.11) which, subtracting the Mw of the RAFT transfer residuals (364.62 g/mol) and considering the Mw of styrene (104 g/mol), corresponds to an average chain length of 42.6 in agreement with the evaluation by TGA.

Knowing the molecular weight of the polymer grown on the titania surface the dimension of its random coil can be evaluated. The radius of gyration, Rg, for polystyrene in a good solvent can be calculated using the formula $Rg=(b/\sqrt{6})*(Mw/Mc)^{0.6,}$ where b is the length of the Kuhn segment (1.8 nm for polystyrene), Mw is the average molecular weight, and Mc is the molar mass of the Kuhn segment (720 g/mol for polystyrene)[37]. Considering a Mw of 5300 g/mol the Rg of 2.44 nm was estimated. Taking into account that the distance between the anchored polymer chains, estimated by TGA and BET measurements, was 1.6 nm, the polymer molecules grafted on the large flat faces of titania nanocrytals are stretched away from the surface and exist in a "*brush*" regime.

The presence of a brushlike behavior of the polymer chains, can explain the relatively low molecular weight of the grafted chains obtained by the RAFT polymerization, although the monomer/transfer agent ratio of 7200 and the very long reaction time would have lead to higher molecular weight.

Considering the high concentration of CTA agents on the flat surface of rutile nanoparticles, the polymerization stops when the growing polymer chain reaches a limiting molecular weight determined by the maximum deformation possible for the random coil in the polymerization medium.

In conclusion despite the low molecular weight of the polymers and thanks to the low polydispersity index (1.11) we can gather that the shell covering particles has a high surface molecular density of homogeneous chains which ensures the compatibilization of

the inorganic filler with the matrix. The thickness of the polymeric film surrounding TiO_2 nanoparticles was estimated about 1.8 nm from as half the thickness of the layer intercalating the rutile rods (see TEM images in paragraph 5.3.2). This ensures a very thin layer of dielectric around the conductive filler particles.

5.3.2 Morphological and Electrical Properties of the Films

The morphological features of the composite material at different filler loading were investigated by TEM microscopy and are reported in Fig. 5.3.5. At low filler concentration (19.7% vol:vol) the rutile nanoparticles are well dispersed into the polystyrene matrix (Fig. 5.3.5a). Increasing the rutile concentration (Fig. 5.3.5b-c) the images reveal the formation of some chestnut-burr aggregates well detectable in Fig. 5.3.5d and typical of rutile nanorods [49]. Observing in details the rod aggregation (Fig. 5) it is evident that a thin polymeric shell (3, 7nm) intercalates the lateral shared faces of the rutile crystals which form the aggregates. At the highest filler loading, 64.1% vol:vol, the aggregates have the tendency to further assemble in large agglomerates, as evidenced by the TEM image in Fig. 5.3.6.

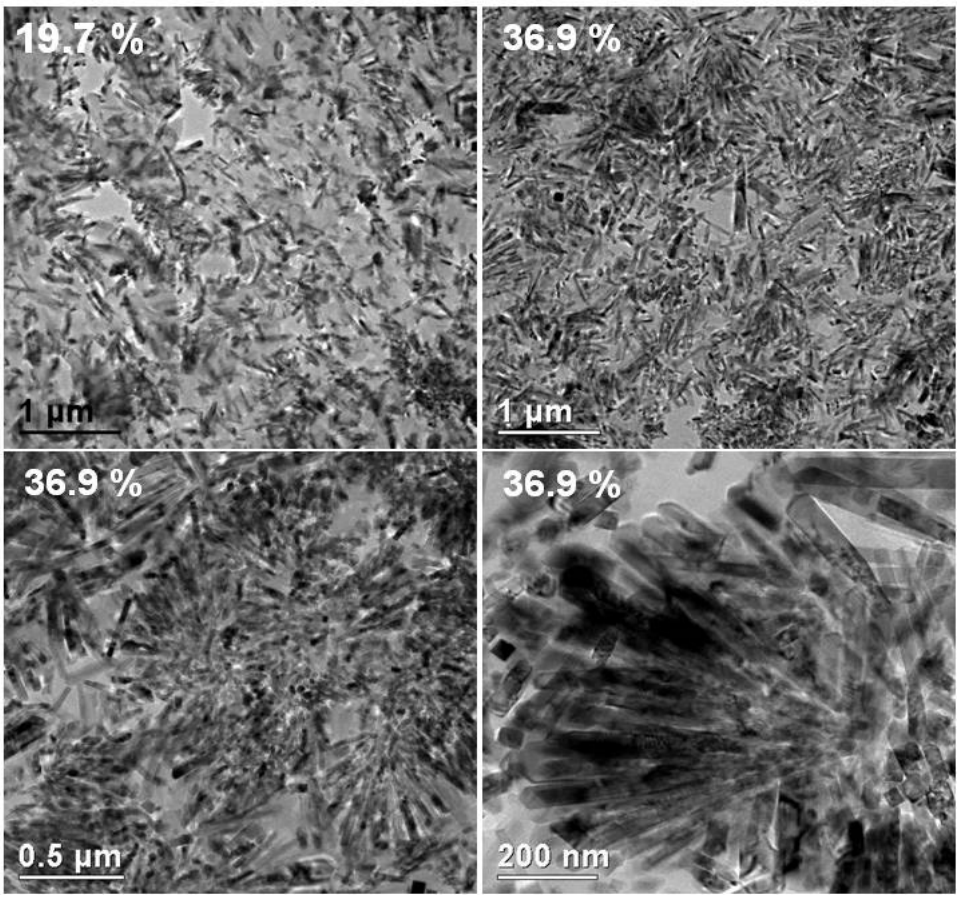

Fig.5.3.5 TEM micrographs of the TiO_2-PS composites at different TiO_2 contents (19.7%, 36.9% and magnifications)

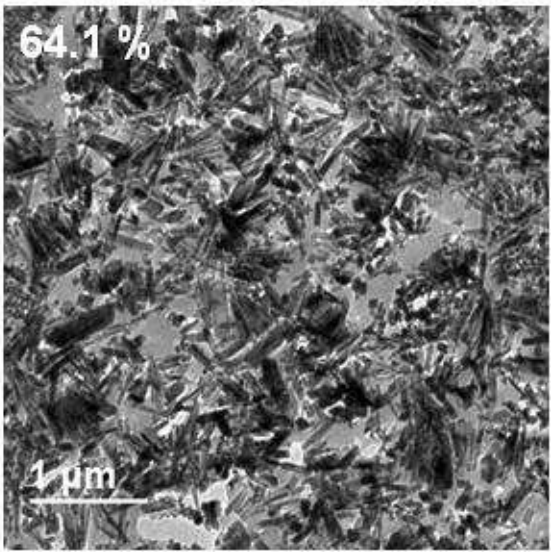

Fig.5.3.6. TEM image of the TiO_2 PS composite with a 64.1% vol:vol of TiO_2.

The effective dielectric constants of TiO_2-PS film were obtained from the measurements of capacitances C using the equation:

$$\varepsilon_r = Cd/\varepsilon_0 A \qquad (2)$$

where d is the film thickness, A is the area of the gold spot and $\varepsilon_0 = 8.854\ 10^{-12}$ F/m.

Because of the importance of geometry in the electric measurements, care was taken in measuring the film thickness. To this purpose each film was cut close to the gold spot, used as electrode, and the cross section was measured by SEM (as example see Fig. 5.3.7).

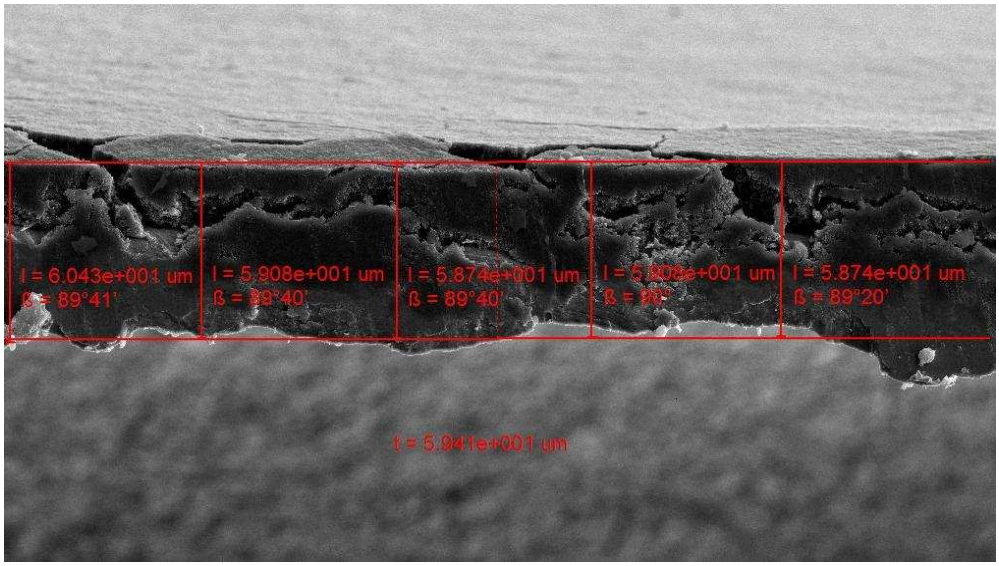

Fig.5.3.7.. SEM cross section of the TiO_2-PS composite film (36.9 % TiO_2**)** used for electric mesurements.

In Fig.5.3.8 the values of the dielectric constant ε_r, measured at 10^4 Hz for the different filler concentrations, are reported. The relative dielectric constant raises with the TiO_2 content. In order to extrapolate the percolation threshold and the q exponent, the experimental data were fitted according to the eq. 1 (plot in Fig.5.3.8). The obtained values were: q=1.09±0.04 and ν_c= 41±1% vol:vol of TiO_2 for the percolation threshold.

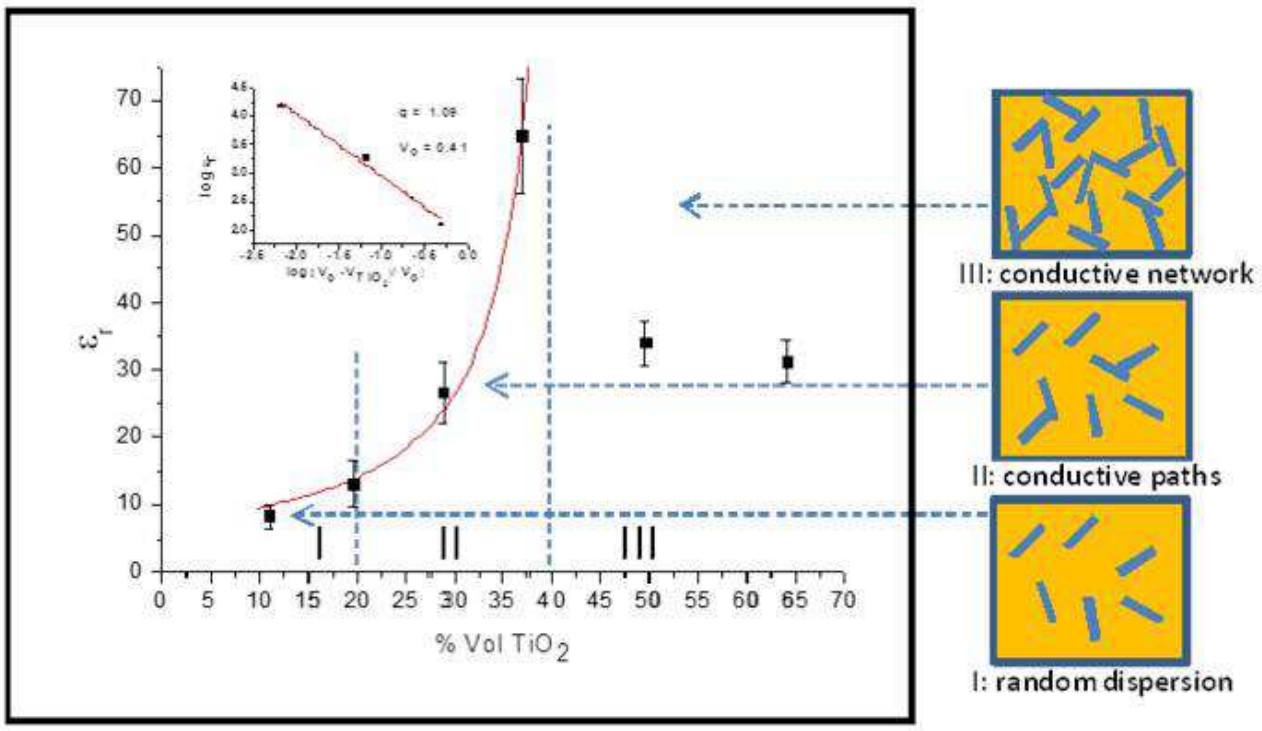

Fig.5.3.8. Variation of the dielectric constant of TiO_2 – PS composite vs the volume fraction of TiO_2 at 10^4 Hz. The inset shows the fitting of the ε_r to the Eq.1 using q, v_c and *c* as adjustable parameters. The schemes on the right represent the composite microstructures by increasing the TiO_2 concentration

The percolation threshold is indicated with a dashed line in Fig.5.3.8. This value is 17% higher than those reported in the literature [26,27] for similar systems and close to the 40% reported by Bhadra [50]. It can be observed that when the matrix is a polymer and behaves as it as continuous host embedding the filler, the percolation threshold depends mainly on the filler shape and dimensions .[51,51]. In our case none of the morphologies reported in the literature allow appropriate comparison, as the electrical properties of our composite are related to the special chestnut burr morphology which favors at the same time both aggregation and separation of rutile particles.

Following the conductivity a potential law analogous to the eq.1[48] the percolation threshold and the q value can be calculated plotting the conductivity of the composite vs. the filler

loading (see Fig.5.3.9) The obtained values for the exponent and percolation threshold were: q=1.17±0.06 and ν_c= 39±2% vol:vol. The values are in reasonable agreement with the correspondent values obtained plotting the dielectric constant.

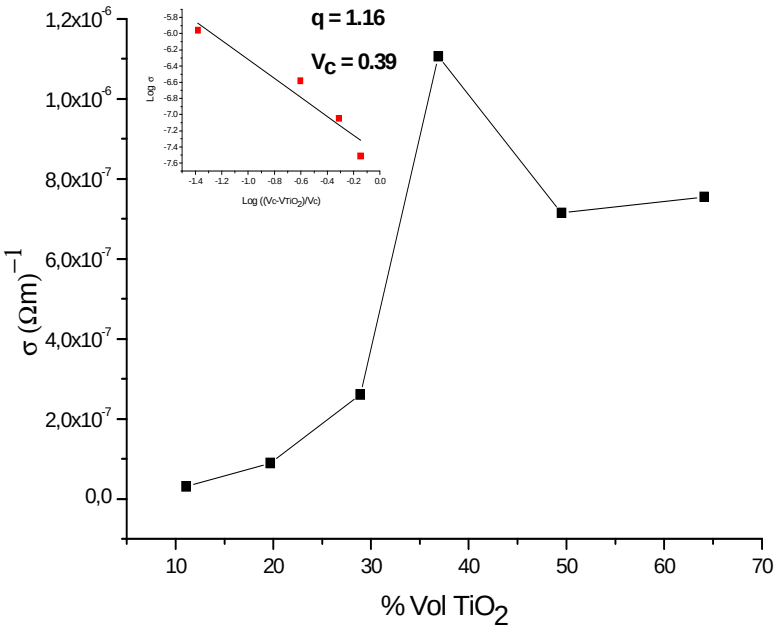

Fig. 5.3.9. Variation of the conductivity of TiO_2-PS composite vs. the volume fraction of TiO_2 at 10^4Hz. The inset shows the fitting of the □ to the Eq.1 using q, v_c and c as adjustable parameters.

According to the percolation theory, as the TiO_2 content approaches the percolation threshold ($v \rightarrow v_c$), the conductivity and the dielectric constant depend on the frequency according to:

$$\sigma \sim \omega^u \quad (3)$$

$$\varepsilon \sim \omega^{u-1} \quad (4)$$

where ω is the frequency and u is a critical exponent with value close to 1 [24].

Following the eq.4 the conductivity increases with the frequency while it becomes independent when u value approaches to 1**.** The plot in Fig. 5.3.10a reports the ε_r values

at different filler concentrations, vs. the frequency. It appears that ε_r is quite independent from the frequency up to the filler concentration of 36.9% vol:vol, which is the maximum concentration below the percolation threshold. After the percolation threshold the slope of the curves, especially at lower frequencies, slightly increases. The u values results 0.99±0.04 and 0.98±0.04 for TiO_2 concentrations of 11.1% and 36.9% respectively.

The plots in Fig. 5.3.10b report the conductivity values, for the different filler concentrations, against the frequency. The u values calculated by fitting the curves between 10^3 and 10^6 Hz, avoiding the distortion in the low frequencies range, result 0.88±0.08 and 0.84±0.08 for 11.1% and 36.9% concentrations, respectively. The obtained values calculated by dielectric and conductivity measurements have a good matching considering the standard deviations. The good fits of the impedance experimental data confirm the validity of the application of the percolative model to this TiO_2-PS composite material.

In Fig. 5.3.10c the plots of tanδ at different filler concentrations against frequency are reported. The trend of tanδ shows the typical increase approaching to the percolation threshold (e.g. from titania content of 28.9% to 36.9%). Nevertheless, the values of the tanδ below the percolation threshold are always lower than 0.10, also at the lowest frequencies. The low tanδ values can be explained by the dense and homogeneous (see TEM images in Fig.5.3.5) brush-like polymer film, which totally covers TiO_2 particles. In fact, this polymeric shell creates a dense insulating layer able to lower the mobility of the charge through the material increasing its resistance. Consequently, below the percolation threshold, this results in a low resistive current which assures low dielectric loss and low energy dissipation.

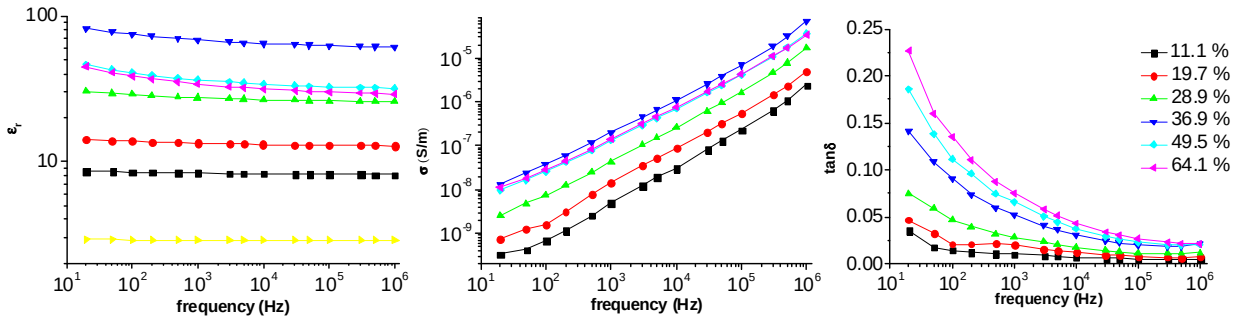

Fig.5.3.10 Spectrum impedance characteristics of the TiO_2-PS composites with different TiO_2 loading. The relative dielectric constant (a), the conductivity (b) and the dissipation factor (c) are plotted vs. the frequency. The yellow curve in a is the measured ε_r of the commercial PS.

The percolative behavior of the electrical properties in the composites can be rationalized in connection with the morphology of the composite material as the TiO_2 amount. increases. At low concentration of TiO_2, where the slight enhancement of the dielectric constant is caused by the increase of the filler content (region I in Fig.5.3.8) in accordance with the classical mixing formulae [19]. In Fig. 5.3.11 we report the plot of the three mostly used mixing formulae which predict the electric properties of the composites till the concentration of 19.6% vol:vol.

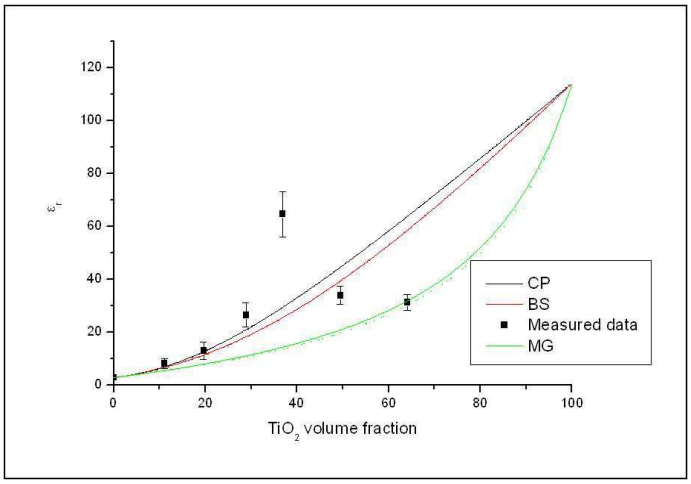

Fig. 5.3.11. Experimental values of the dielectric constant of TiO_2-PS composites at different filler loading. The curves represent the best fit according to the mixing formulae reported by Jylha[19].

The formation of these aggregates corresponds to a suddenly increase of the dielectric constant (region II in Fig.5.3.8). Thus, applying the dielectric percolation theory [52], we can ascribe to these aggregates the origin of the microcapacitive structures responsible for the increase of the dielectric properties. The intrinsic rutile tendency to the aggregation suggests that the shape of rutile crystals is well suitable to stabilize the microcapacitive structures formed by the rods and by the intercalation of a thin polymer layer between the crystals (Fig. 5.3.12). Under electric field the carrier displacement takes place and the induced polarization of the microstructures causes the large dielectric constant. This tendency of rutile to self assemble in not interconnected chestnut-like aggregates explains the high value of the percolation threshold. After the percolation threshold (filler concentration > 41%) the number of the chestnut-like aggregates increase. The aggregates become now interconnected with each other and form the percolative network which causes the sudden change of the dielectric characteristics (region III in Fig.5.3.8).

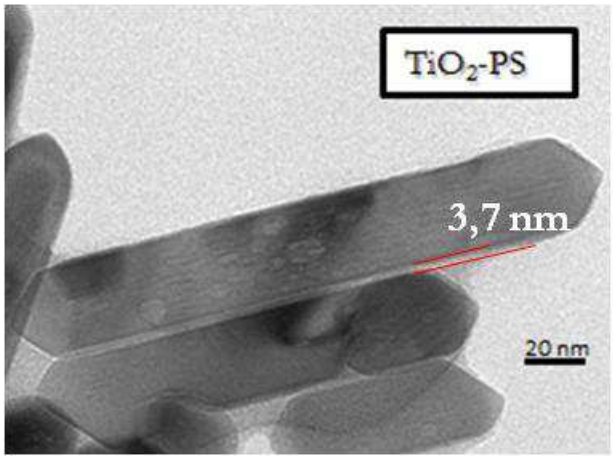

Fig.5.3.12 TEM micrograph of rutile rods coated with polystyrene shell.

5.4 Conclusions

Here a new polymeric/inorganic composite material is reported, which exhibits very high dielectric constant and high percolation threshold.

The dielectric solid was obtained by coating the surface of rutile TiO_2 particles with polystyrene grown by RAFT polymerization and by dispersing them into polystyrene matrix.

The origin of the high dielectric constant can be ascribed to the assembling of rutile nanoparticles in chestnut-like aggregates, where a number of core shell rutile crystals share their faces and form capacitive microstructures. The self-assembling properties of the rod-shape rutile are reproducible and this favors the reproducibility of the electric properties. These aggregates separated by a thin layer of polymer allow the high increase of the filler amount up to 41% vol:vol avoiding the formation of the continuous network responsible for the sudden change of the electric characteristics. The anchoring coordinative nature of the polymeric chains with the filler surface, giving a *class II* hybrid material, creates a uniform surrounding layer around the particle independent by the matrix amount concentration. This layer acts as insulating layer which seems contributing to mitigate the charge mobility and consequently the conductivity of the material. The low conductivity of the material allows to obtain low tanδ values.

Despite the high content of inorganic fillers, the dissipation factor remains low, even approaching the lower frequencies. The low tanδ values in a large range of frequencies allows to candidate the material for radio frequency (RF) applications where very low dissipation factor is desired to avoid signal losses.

References

[1] A. Facchetti, M. H. Yoon, T. J. Marks, Adv. Mater., *2005*, **17**, 1705

[2] Q. M. Zhang, H. F. Li, M. Poh, F. Xia, Z. Y. Cheng, H. S. Xu, *Nature*, *2002*, **419**, 284

[3] Y. Bai, Z. Y. Cheng, V. Bharti, H. S. Xu, Q. M. Zhang, *Appl. Phys. Lett.*, *2000*, **76**, 3804

[4] A. Burke, *Electrochimica Acta*, *2007*, **53**, 1083

[5] S. R. Forrest, *Nature*, *2004*, **428**, 911.

[6] C. Dimitrakopoulos, P. Malenfant, *Adv. Mater.*, *2002*, 14, 99

[7] R. Wallace, G. Wilk, MRS Bull., *2002*, **March 2002**, 192

[8] S. Roberts, *Phys. Rev.*, *1949*, **76,** 1215.

[9] S. Campbell, H. Kim, D. Gilmer, B. He, T. Ma, W. Gladfelter, *W. IBM J. Res. Dev.*, *1999*, **43**, 383

[10] A. K. Tagantsev, V. O. Sherman, K. F. Astafiev, J. Venkatesh, N. Setter, *J. of Electroceramics*, *2003*, **11**, 5.

[11] G. Goh, S. Donthu, P. Pallathadka, Chem. Mater. *2004*, **16**, 2857.

[12] W. Wunderlich, Physical Constant of Poly(methyl methacrilate). In *Polymer Handbook*, 3rd ed.; J. Brandrupp, E. Immergut, Eds.; John Wiley & Sons: New York, *1989*; p V77.

[13] J. Rudd, Physical Constant of Poly(styrene). In *Polymer Handbook*, 3rd ed.; J. Brandrupp, E. Immergut, Eds.; John Wiley & Sons: New York, *1989*; p V81.

[14] B. Balasubramanian, K. L. Kraemer, N. A. Reding, R. Skomski, S. Ducharme, D. J. Sellmyer, *ACS Nano*, *2010, 4 (4)*, 1893

[15] B. Chu, M. Lin, B. Neese, Q. Zhang, J. Appl. Phys., *2009*, **105**, 14103.

[16] J. Xu, C. P. Wong, *Composites Part. A*, *2006*, **38A**, 13.

[17] P. Badheka, V. Magadala, N. G. Devaradju, B. I. Lee, E. S. Kee, J. Appl. Polym. Sci. *2005*, **99**, 2815.

[18] P. Barber, S. Balasubramanian, Y. Anguchamy, S. Gong, A. Wibowo, H. Gao, H. J. Ploehn, H. C. zur Loye, Materials, *2009*, **2**, 1697

[19] L. Jylha, A. Sihvola, *J. Phys. D: Appl. Phys.*, *2007*, **40**, 4966

[20] C. Pecharroman, J. S. Moya, *Adv. Mater.,2000*, **12**, 294.

[21] Z.-M. Dang, L.-Z. Fan, Y. Shen, C.-W. Nan, *Chemical Physics Letter*, *2003*, **369**, 95.

[22] D. J. Bergman, Y. Imry, *Phys. Rev. Lett.*, *1977*, **39**, 1222.

[23] L. Qi, B. I. Lee, S. Chen, W. D. Samuels, G. J. Exarhos, *Advanced Materials*, *2005*, **17**, 1777

[24] Z. M. Dang, J. P. Wu, H. P. Xu, S. H. Yao, M. J. Jiang, *Appl. Phys. Lett.*, ***2007***, **91**, 072912.

[25] D. M. Grannan, J. C. Garland, D. T. Tanner, *Phys. Rev. Lett.*, *1981*, **46**, 375.

[26] Z. M. Dang, Y. H. Lin, C. W. Nan, Adv. Mater, *2003*, **15**, 1625.

[27] G. Wang, *Applied Materials and Interfaces*, *2010*, **2**, 1290.

[28] H. Althues, J. Henle, S. Kaskel, *Chem. Soc. Rev. 2007*, **36**, 1454.

[29]N. Nakayama, T. Hayashi, *Colloids Surf., A 2008*, **317**, 543.

[30] P. H. Mutin, G. Guerrero, A. Vioux, *Journal of Materials Chemistry 2005*, **15**, 3761.

[31] V. Lafond, C. Gervais, J. Maquet, D. Prochnow, F. Babonneau, P. H. Mutin, *Chemistry of Materials 2003*, **15**, 4098.

[32] G. Guerrero, P. H. Mutin, A. Vioux, *Chemistry of Materials 2001*, **13**, 4367.

[33] M. Crippa, M.Callone, M. D'Arienzo, K. Mueller, S. Polizzi, L. Wahba, F. Morazzoni, R. Scotti, *Applied Catalysis B: Environmental*, *2011*, **104**, 282

[34] P. Tao, Y. Li, A. Rungta, A. Viswanath, J. Gao, B. C. Benicewics, R. W Siegel, L. S. Schadler, *J. Mater. Chem*, *2011*, **21**, 18623

[35] M. A. White, A. Maliakal, N. J. Turro, J. Koberstein, *2008*, **29**, 1544

[36] M. N. Tchoul, S. P. Fillery, H. Koerner, L. F. Drummy, F. T Oyerokun, P. A. Mirau, M. F. Durstock, R. A. Vaia, *Chem. Mater.*, *2010*, **22**, 1749.

[37] A. Maliakal, H. Katz, P. M. Cotts, S. Subramoney, P. Mirau, *J. Am. Chem. Soc.*, *2005*, **127**, 14655.

[38] J. Pyun, K. Matyjaszewski, T. Kowalewski, D. A. Savin, G. D. Patterson, G. Kickelbick, N. Huesing, *J. Am. Chem. Soc. 2001*, **123**, 9445.

[39] J. Pietrasik, C. M. Hui, W. Chaladaj, H. Dong, J. Choi, J. Jurczak, M. R. Bockstaller, K. Matyjaszewski, *Macromol. Rapid Comm. 2011***, 32**, 295.

[40] C. Bartholome, E. Beyou, E. Bourgeat-Lami, P. Chaumont, F. Lefebvre, N. Zydowicz, *Macromolecules 2005*, **38**, 1099.

[41] B. Hojjati, P. A. Charpentier, P.A. *J. Polym. Sci: Part A: Polym. Chem. 2008*, **46**, 3926.

[42] B. J. Lowes, A. G. Bohrer, T.T. Tran, D .A. Shipp, *Polym. Bull. 2009*, **62**, 281.

[43] Andrew G. Thomas and Karen L. Syres, *Chem. Soc. Rev.*, 2012, **41**, 4207-4217

[44] J. T. Lai, D. Filla, R. Shea, *Macromolecules 2002***, 35***,* 6754.

[45] A. Testino, I. R. Bellobono, V. Buscaglia, C. Canevali, M. D'Arienzo, S. Polizzi, R. Scotti, F. Morazzoni, *J. Am. Chem. Soc. 2007*, **129**, 3564.

[46] S. Brunauer, P. H. Emmet, E. Teller, *J. Am. Chem. Soc. **1938***, **60**, 309.

[47] L. Ojamue, C. Aulin, H. Pedersen, P. O. Käll, P-O, *J. Coll. Inter. Sci*., *2006***, 296**, 71.

[48] C. H. Liu, C. Y. Pan, *Polymer*, *2007*, **48**, 3679.

[49] R. Scotti, M. D'Arienzo, F. Morazzoni, I. R. Bellobono *Applied Catalysis B: Environmental*, *2009***, 88***,* 323.

[50] D. Bhadra, A. Biswas, S.Sarkar, B.K. Chaudhuri, K.F. Tseng, H.D.Yang, J. App. Phys., *2010*, **107**, 124115.

[51] C. Chiteme, D.S. Mclachlan, *Physica B*, *2000*, **279**, 69.

[52] C. W. Nan, Y. Shen, J. Ma, *Annu. Rev. Mater. Res.*, *2010*, **40**, 131.

CHAPTER 6

Conclusions

The overall conclusions of the dissertation will be focused on the hybrid and nanocomposite aspects of the three materials described in details explained in chapters 3, 4 and 5. The general concepts of hybrid and nanocomposite were used not only to classify but also to drive the synthesis optimizing the materials for the different applications.

The common denominator of each material was the titanium dioxide as photoreactive material, chapters 3 and 4, and dielectric material in chapter 5. Because both the morphology and the crystal phase of the titanium dioxide play a crucial role on the material performances the used TiO_2 was always synthesized ex situ by hydrothermal synthesis allowing to control the morphological characteristics. In the chapter 3 and 4 anatase phase was used for its photocatalytic ability in presence of oxygen and water while in the chapter 5 the rutile phase was used because its highest dielectric constant compare anatase.

In chapter 3 a polyacrilate composite material prepared by mechanical mixing of nanocrystalline titania with acrylate oligomers shows that, without titania surface functionalisation, the oxide forms micrometric aggregates reducing the exposed surface of the TiO_2. Despite the filler aggregation the material preserves its photocatalytic properties. As drawback of the photocatalytic activity in phenol photomineralisation (use to simulate pollutants in water) some photooxidative degradation phenomena involve the organic matrix. Hence the necessity to have a stable material was the driving force to create a new material containing titania as photoactive material while embedded into an inorganic matrix.

In the chapter 4 this porous and UV transparent inorganic-inorganic nanocomposite material is described. In order to obtain the desired porosity of the final material the silica sol-gel solution was mixed with PEG obtaining a *class I* hybrid material. During the silica formation PEG segregates in warm-like polymeric phase that, once the material is calcinated, leaves the voids conferring the desired macroporosity to the material. The

photoactive oxide, previously functionalized on the surface with organic molecules, migrates in the polymeric phase during silica precursors hydrolysis and condensation. After calcination the titania nanocrystallites decorate the wall of the channels leaved by the organic species remotion. The molecules functionalizing the catalyst surface induce the TiO_2 migration into the PEG phase because of their more affinity with polymer instead with silica. The exposed titania is then able to freely react with pollutants while the silica matrix provides the UV transparency and macroporosity for the photocatalytic reactions. The abatement efficiency of the material is comparable with slurry TiO_2. The material is not affected by the photocatalyst leaching demonstrating that it is suitable for an industrial application. The nanocomposite material was tested for NO_x degradation too using P25 commercial titania instead of home made one demonstrating the generality of the preparation method. The abatement efficiency of the NOx was comparable with the DENOX technology currently used for industrial applications.

In chapter 5 the same reaction technique used to functionalize the nanoparticles in the chapter 4 was used to functionalize rutile titania nanoparticles with a RAFT reagent. After the styrene “polymerization from” reaction polystyrene chains were obtained. The brush like conformation of the chains justifies the high polymer surface density. The functionalized nanoparticles (c*lass II* material) are mixed in different concentrations with commercial polystyrene. The different concentration materials present good dispersion because of the high compatibilization properties of the surface functionalisation. At high concentrations the material shows a percolative behavior ascribed to the formation of chestnut like aggregates which increase the relative dielectric constant. Despite the charges percolation trough the material the polymeric surface layer acts as an insulating layer which contributes to mitigate the charge mobility and consequently the conductivity of the material. The low conductivity of the material allows to obtain low tanδ values.

The low tanδ values in a large range of frequencies allows to candidate the material for radio frequency (RF) applications where very low dissipation factor is desired to avoid signal losses.

In conclusion the present work, despite it covers three different materials, demonstrates how it is possible to create and optimize a material modifying the surface of the nanoparticles in order to confer them peculiar properties which drive the final material morphology. The final material morphology is then able to combine the properties both of the active material and of the matrix giving a new optimized material for a specific application.

Acknowledgements

Doverosamente ringrazio il Prof. Scotti e la Prof. sa Morazzoni per come mi hanno accolto nel gruppo ma soprattutto per la delicatezza che mi hanno mostrato quando nuvole cariche di tristezza si sono addensate nella mia vita.

Naturalmente un ringraziamento alla mia famiglia, ai colleghi e agli amici che da anni sopportano il pelato brontolone.

E infine un ringraziamento a Louisa per i sorrisi e la luce che porta nella mia vita.